

DIGITAL RECONSTRUCTION OF MULTIDIMENSIONAL
SIGNALS FROM THEIR PROJECTIONS

by

Russell Manning Mersereau

S.B., S.M., Massachusetts Institute of Technology
(1969)

E.E., Massachusetts Institute of Technology
(1970)

SUBMITTED IN PARTIAL FULFILLMENT OF THE
REQUIREMENTS FOR THE DEGREE OF
DOCTOR OF SCIENCE

at the

MASSACHUSETTS INSTITUTE OF TECHNOLOGY

February, 1973

Signature of Author _____

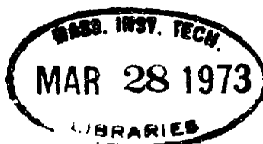
Department of Electrical Engineering, January 17, 1973

Certified by _____

Thesis Supervisor

Accepted by _____

Chairman, Departmental Committee on Graduate Students



DIGITAL RECONSTRUCTION OF MULTIDIMENSIONAL
SIGNALS FROM THEIR PROJECTIONS

by

Russell Manning Mersereau

Submitted to the Department of Electrical Engineering on January 17, 1973
in partial fulfillment of the requirements for the Degree of Doctor of
Science.

ABSTRACT

Several algorithms for the reconstruction of multidimensional signals from their projections are presented. These algorithms can be applied to the problem of estimating the structure of an unknown three-dimensional object from its x-ray photographs or electron micrographs taken at different orientations. The reconstruction problem is broken into two distinct steps; first samples of the Fourier transform of the unknown signal are computed from a series of digitized projections, then the unknown is estimated from the samples of its Fourier transform. Reconstructions are considered from several sets of samples in Fourier space. A particular set of samples, the concentric squares raster is developed, the reconstructions from which are superior to those made from the more traditional polar raster of samples for bandlimited inputs which have a rectangular frequency band. Furthermore for an important class of unknowns exact reconstructions can be performed from a concentric squares raster from a finite number of projections. In fact for this class of unknowns a single projection is sufficient. A detailed treatment of the one-projection reconstruction problem is presented and the difficulties associated with its solution are explored.

THESIS SUPERVISOR: Alan V. Oppenheim
TITLE: Associate Professor of Electrical Engineering

ACKNOWLEDGMENT

This thesis and its author have been influenced by many people. I am particularly indebted, however, to two of them. The first is Professor A.V. Oppenheim who suggested and supervised this research and by example, encouragement and insight guided it into its final form. The second is my wife Martha who contributed the patience and understanding to make it all worthwhile.

I would also like to express my appreciation to Professor T.S. Huang, and to Drs. B. Gold and O. Tretiak for their suggestions and criticisms throughout the duration of this undertaking and to S. Finn and D. Johnson for numerous meaningful discussions.

I would also like to thank Diane Horner for the high quality of the finished manuscript. Her influence is the most noticeable of all.

TABLE OF CONTENTS

ABSTRACT	2
ACKNOWLEDGEMENT	3
TABLE OF CONTENTS	4
LIST OF FIGURES AND TABLES	7
I. INTRODUCTION	
1.1 Introduction	10
1.2 Previous Development of the Problem	12
1.3 The Scope of this Thesis	13
II. MULTIDIMENSIONAL FOURIER TRANSFORMS AND PROJECTIONS	
2.1 Definitions and Background Mathematics	16
2.1.1 The one-dimensional Fourier transform	16
2.1.2 The N-dimensional Fourier transform	23
2.2 Projections	30
2.2.1 Examples of projection functions	33
2.2.2 The projection/slice theorem	36
2.3 A Generalized Reconstruction Algorithm	40
2.4 Number of Projections	46
2.5 Equivalence of Reconstruction and Picture Representation	47
2.6 Reducing a Three-Dimensional Reconstruction to a Series of Two-Dimensional Reconstructions	48
III. RECONSTRUCTION FROM A POLAR RASTER	
3.1 Introduction	50
3.2 Reconstruction by Interpolation	54
3.3 Reconstruction by Interpolation in Polar Coordinates	61

3.4	Reconstruction by Smearing	71
3.5	Reconstruction Using Hankel Transforms	88
3.6	Considerations in Implementing Any Reconstruction Scheme	90
3.6.1	Computation of projections	90
3.6.2	Aliasing and transforming	94
3.6.3	Origin centering	95
3.6.4	Block floating point	96
IV.	RECONSTRUCTING FROM A CONCENTRIC SQUARES RASTER	
4.1	Introduction	97
4.2	The Concentric Squares Raster	100
4.3	Bandlimited Functions of Finite Order	108
4.4	Approximate Reconstructions from a Concentric Squares Raster	112
4.4.1	Linear interpolation	112
4.4.2	Reconstruction by high order interpolation along the squares	119
4.4.3	Concentric squares smearing	122
4.4.4	Reconstructions from real data	126
4.5	The Use of Projections to Characterize Pictures	128
V.	EXACT RECONSTRUCTION FROM A SINGLE PROJECTION	
5.1	Introduction	136
5.2	The One-Projection Theorem	137
5.3	An Algorithm for Recovering Picture Samples from One Projection	147
5.4	The Inverse Chirp - z-Transform Algorithm	151
5.5	Sensitivity of the ICZT to Input Quantization Errors	157
5.6	Recovering a Bandlimited Three-Dimensional Function of Finite Order from a Single Projection	168

5.7 Using the ICZT to Reconstruct Bandlimited Functions of Order N from More Than One Projection	172
VI. SUMMARY AND SUGGESTIONS FOR FURTHER RESEARCH	
6.1 Summary	178
6.2 Suggestions for Further Research	179
BIBLIOGRAPHY	181
BIOGRAPHICAL NOTE	185

LIST OF FIGURES AND TABLES

<u>Figure</u>		<u>Page</u>
2.1	An example of a bandlimited function with bandwidth W .	19
2.2	A two-dimensional bandlimited function.	24
2.3	The region over which $G(e^{j\omega_1}, e^{j\omega_2})$ can be non-zero in order to apply the sampling theorem.	26
2.4	The samples of the Fourier transform of a function which correspond to the DFT.	28
2.5	The aperture corresponding to an idealized fan-beam scan.	35
2.6	The relation between a projection and a slice.	37
2.7	Lines in the two-dimensional Fourier plane where $F(\omega_x, \omega_y)$ would be known from 8 projections.	43
2.8	Points at which a two-dimensional Fourier transform would be known if the transforms were computed digitally.	44
3.1	The definition of a bandlimited function.	53
3.2	A comparison of the zeroth-order and linear interpolation schemes.	56
3.3	Reconstructions by zeroth-order interpolation from 64 evenly spaced projections.	59
3.4	Reconstructions by linear interpolation from 64 evenly spaced projections.	60
3.5	The reconstruction algorithm based on interpolation in polar coordinates.	70
3.6	Reconstructions by interpolation in polar coordinates followed by linear interpolation.	72
3.7	The area ΔA_{mi} associated with one polar sample.	75

<u>Figure</u>		<u>Page</u>
3.8	The smearing algorithm	79
3.9	Reconstructions by smearing from 64 evenly spaced projections.	82
3.10	Reconstructions by smearing for different numbers of projections.	84
3.11	An enlarged view of the centers of the polar and Cartesian rasters.	86
3.12	The algorithm used for computing projections.	92
4.1	The region of the Fourier plane over which the transform of a bandlimited picture is non-zero.	98
4.2	Relation between the Fourier transform of a bandlimited function and the N-point DFT of its samples.	102
4.3	A concentric squares raster.	103
4.4	An 8 x 8 polar raster superimposed on an 8 x 8 concentric squares raster.	104
4.5	A configuration for recording concentric squares projections.	107
4.6	A set of Fourier plane samples from which an 8 x 8 sampled picture can be reconstructed exactly.	110
4.7	Reconstructions obtained by using linear interpolation on a concentric squares raster with 64 evenly spaced projections.	114
4.8	Reconstructions obtained by using linear interpolation on a concentric squares raster from 64 projections whose slices have evenly spaced intersections with the concentric squares.	115
4.9	Reconstructions by linear interpolation from a concentric squares raster.	116
4.10	Comparison of the linear interpolation algorithm for polar samples and concentric squares samples.	117

<u>Figure</u>		<u>Page</u>
4.11	Reconstructions from 64 projections by approximating $F(\omega_x, \omega_y)$ along each square side by a polynomial $x^x y^y$ of 32nd degree.	121
4.12	The area ΔA_1 associated with one concentric squares sample.	123
4.13	Some reconstructions made by smearing 64 concentric squares projections.	125
4.14	Reconstruction of a section of a leg bone from 36 evenly spaced projections using linear interpolation.	127
4.15	A comparison of reconstructions for different values of L, M and b in the smearing algorithm.	130
5.1	The samples corresponding to the extended definition of $S_\theta(k\Delta\omega)$.	150
5.2	A digital network whose unit sample response is the solution to the inverse CZT problem.	155
5.3	The location of one critical slice for recovering N^3 function samples of a three-dimensional bandlimited function of order N.	171
 <u>Table</u>		
5.1	The sensitivity of the inverse CZT for different values of L and M.	165
5.2	The reconstruction of a bandlimited picture of order 2 from the single projection at $\theta_0 = \tan^{-1} 1/2$.	166
5.3	The reconstruction of a bandlimited picture of order 4 from the single projection at $\theta = \tan^{-1} 1/4$.	167
5.4	The reconstruction of a bandlimited picture of order 4 from the projections at $\theta_1 = \tan^{-1} 1/2$ and $\theta_2 = \tan^{-1}(-1/2)$.	174

Chapter I
INTRODUCTION

1.1 Introduction

In this thesis we shall be concerned with the problem of approximating or reconstructing unknown multidimensional signals from their projections. A projection represents an $N - 1$ dimensional representation of an N -dimensional signal, much as a transmission x-ray photograph is a two-dimensional representation of a three-dimensional unknown structure. A projection, like an x-ray photograph is formed by superimposing all structural detail in a particular direction and thus with each projection we can associate an orientation. In general a single projection will provide an incomplete description of an unknown signal. In this dissertation, therefore, we shall consider techniques whereby an unknown signal can be determined either exactly or approximately from a set of projections at different orientations.

Throughout this dissertation this problem shall be considered as a mathematical, signal processing problem. There are, however, a number of problems of practical importance which can be interpreted within the framework of recovering signals from their projections. One of these is the approximation of visually opaque structures from their x-ray photographs which was alluded to earlier. From x-ray photographs

of an unknown taken at different orientations, we can approximate the optical density function of the object being x-rayed. Also a transmission electron micrograph (as opposed to a scanning electron micrograph), can be considered to be a projection of the specimen under observation. By tilting the stage of the microscope, it is possible to obtain different projections of the same specimen. It is also frequently possible to obtain different projections by identifying the orientations of different structures, such as viruses which are projected on a single electron micrograph. In the case of some symmetrical structures such as helical viruses it is also frequently possible to obtain several projections from a single view.

Another application which frequently occurs in medicine is the autoradiograph scan. If for example we wish to observe the blood circulation in a person's brain, perhaps to detect a hemorrhage, we can inject radioactive tracers into the bloodstream; then at a later time, with a scintillation counter we can scan along planes in the vicinity of the brain. These planar scans constitute projections which can then be processed to yield the size and location of any hemorrhage. The procedures for recovering a function (signal) from its projections can also be used to invert fan-beam radiotelescope scans or to recover the point spread function of a two-dimensional linear optical system from a series of line responses.

If a function can be reconstructed exactly or even approximately from its projections, then those projections must characterize that function. Thus it has been suggested that projections might be useful for pattern recognition (5), (6) or for bandwidth compression in communicating

and storing pictures. In both of these applications it is suggested that much of the redundancy which is present in storing multidimensional signals in terms of their samples, might be removed by storing only a limited number of projections of those signals. The possibility of using projections for bandwidth compression will be discussed at the end of Chapter IV.

Correlating all of the information in several projections is a formidable task, however, the problem is readily amenable to machine computation. The projections can be sampled and together with their orientation parameters put into a digital computer which can then compute a reconstruction. There are additional advantages to approaching the problem digitally. Irregularities in the projections can be compensated for and the N-dimensional image can be processed to enhance important features, such as perhaps contours, or to suppress undesirable ones. Also computations can be made on the unknown - distances can be measured, volumes computed, etc. There are also some constraints that are introduced by treating the problem digitally. The projections must be expressible in terms of their samples for instance.

1.2 Historical Development of the Problem

The basis for most of the algorithms which perform reconstructions from projections is a theorem which we shall call the projection slice theorem. It appears to have been discovered on at least two different occasions independently. Bracewell (3) used it in 1956 to invert fan-beam radio telescope scans and DeRosier and Klug (17) in 1968 used it to perform reconstructions from electronmicrographs of helical viruses.

Since 1968, a number of workers, particularly biophysicists have been attracted to the problem and have presented a number of computer algorithms for performing reconstructions. In this regard the reader is referred to the papers of Crowther, DeRosier and Klug (7) - (18), Ramachandran (45), (46), (47) and Vainshtein (39), (50), (51). A unique statistical algorithm has been suggested by Gordan, Herman et al. (2), (19), (20), (24), (25), (30), (31). The problem has also been approached optically and an optical system for generating reconstructions has been built by Grant, Garrison et al. (21), (26), (27) which superimposes projections. This is the optical counterpart of an algorithm presented in section 3.4 of this thesis.

1.3 The Scope of this Thesis

Except for the optical techniques of Grant (21), (26), (27) and Hart (28), (29) all previous attempts at performing reconstructions from projections have used a digital computer. This imposes certain constraints on the class of allowable input functions. First the projections must be sampled. For the projections to be recoverable from their samples this normally requires that the unknown be bandlimited. Furthermore the reconstruction can only be performed at a limited number of points. Thus the unknown must be determined by its samples which further requires that the unknown be bandlimited. In this thesis, therefore we shall focus our attention on bandlimited functions. In this regard the present work represents a departure from the work of others in the field who have not explicitly considered bandlimited functions,

although they have assumed that sampling could be performed and have thus implied bandlimitedness. Restricting the range of possible input functions is not a particularly serious constraint since most unknown signals of interest, if not strictly bandlimited themselves, can be closely approximated by such functions. On the other hand, restricting ourselves to bandlimited functions or even to specific classes of bandlimited functions has its rewards, for many of the properties of such signals can be exploited in the design of reconstruction algorithms. This problem can also be considered as a digital signal processing problem and many of the results of that discipline which are concerned with sampled data and thus bandlimited functions, can be used in the design of more powerful and efficient algorithms than could be obtained without the assumption of bandlimitedness.

Throughout this thesis most results have been phrased in terms of reconstructing two-dimensional functions (photographs) from their one dimensional projections. Most of the two-dimensional results can be straightforwardly extended to three or more dimensions but the two-dimensional case is simpler to work with. It yields more tractable mathematical expressions, its demands on computation time and storage are reduced and the results are easier to display.

This thesis is divided into four parts. Some classical results from digital signal processing are presented in Chapter 2 as background information, since they are of central importance in understanding the algorithms which follow in later chapters. Also in this chapter projection functions are formally defined and the projection/slice theorem is

presented upon which all of the algorithms depend. In Chapter III several algorithms are presented, some of which were suggested by other workers. These are presented mainly for comparison with the algorithms of Chapter IV, where we assume that the class of unknown signals is a subset of the class of bandlimited functions. By exploiting the properties of this class of functions, a series of algorithms are developed which yield improved reconstructions over the algorithms of Chapter III. A particularly interesting property of this class of functions is that they can be reconstructed in theory from a single projection. In Chapter V the implications of this property are considered.

Chapter II

MULTIDIMENSIONAL FOURIER TRANSFORMS AND PROJECTIONS

2.1 Definitions and Background Mathematics

The intent of the first section of this chapter is to standardize the notation and define the terms that will be used throughout this thesis. It will summarize some of the background material from the field of multi-dimensional signal processing upon which the work in this thesis depends heavily. This material, although not difficult, may be unfamiliar to some readers. Of particular concern is the operation of taking the Fourier transform of a multidimensional signal since most of the reconstruction algorithms are performed in Fourier space rather than in function space. In the latter part of the chapter, the projection/slice theorem is presented.

2.1.1 The One-Dimensional Fourier Transform

If $f(x)$ represents a function in a single variable which is continuous from the right and if

$$\int_{-\infty}^{\infty} |f(x)| dx < \infty$$

then we can define a function $F(\omega_x)$ which we shall call the Fourier transform of $f(x)$ by means of (2.1).

$$F(\omega_x) = \int_{-\infty}^{\infty} f(x) \exp[-jx\omega_x] dx \quad (2.1)$$

where

$$j = \sqrt{-1}$$

$F(\omega_x)$ and $f(x)$ are equivalent in that one function can be determined from the other. In particular $f(x)$ can be computed from $F(\omega_x)$ by means of (2.2).

$$f(x) = \frac{1}{2\pi} \int_{-\infty}^{\infty} F(\omega_x) \exp[jx\omega_x] d\omega_x \quad (2.2)$$

The two functions $f(x)$ and $F(\omega_x)$ are often referred to as a Fourier transform pair. The domain of f is referred to as the time domain or space domain. We shall prefer the latter term since in this work the variable x will generally represent a spatial rather than a time variable. The domain of $F(\omega_x)$ is often referred to as the frequency domain, the Fourier domain, or by the somewhat confusing term Fourier space. The Fourier transform then represents a mapping of a function from the space domain to the Fourier domain. Many operations which are difficult to perform in one domain become particularly simple when considered in the other domain. Convolution and projection (for multidimensional signals) are two such operations.

Notationally we shall use capital letters to describe functions defined in the Fourier domain and lower case letters for functions defined in the space domain. Greek letters shall denote Fourier domain variables and roman letters shall denote space domain ones.

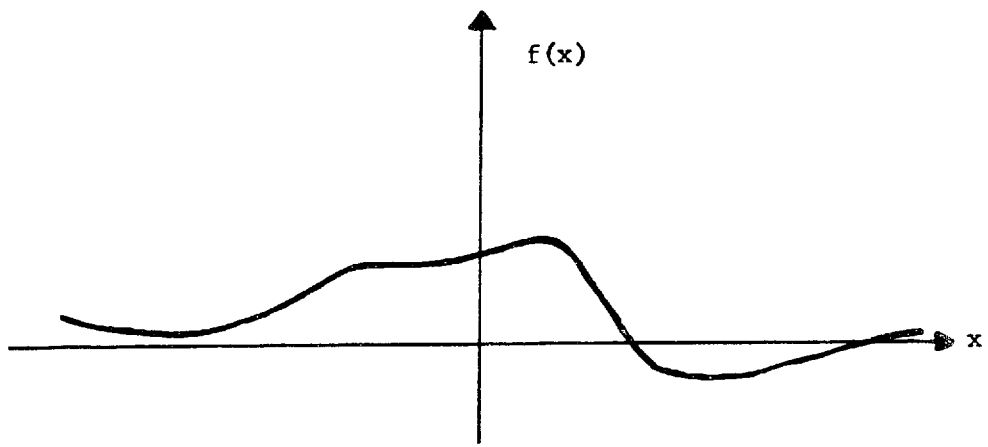
The Fourier transformation and the inverse Fourier transformation as defined in equations (2.1) and (2.2) respectively are functions of continuous variables and as a result these equations are not readily amenable to machine computation unless we impose some additional constraints upon $f(x)$ (or conversely upon $F(\omega_x)$). The function $f(x)$ will be said to be bandlimited if $F(\omega_x) \equiv 0$ for $|\omega_x| > W$ for some number W , which is referred to as the bandwidth. This definition is illustrated in figure 2.1. Note that we say that $f(x)$ is bandlimited while the constraint is actually applied to $F(\omega_x)$. $F(\omega_x)$ is bandlimited if $f(s) \equiv 0$ for $|x| \geq X$ for some X . To avoid confusion in the latter case we usually say that $f(x)$ is spacelimited.

If $f(x)$ is a bandlimited function, then $F(\omega_x)$ is non-zero only over a limited region of the ω_x -axis and we can thus expand $F(\omega_x)$ in a Fourier series. If W_1 is greater than W

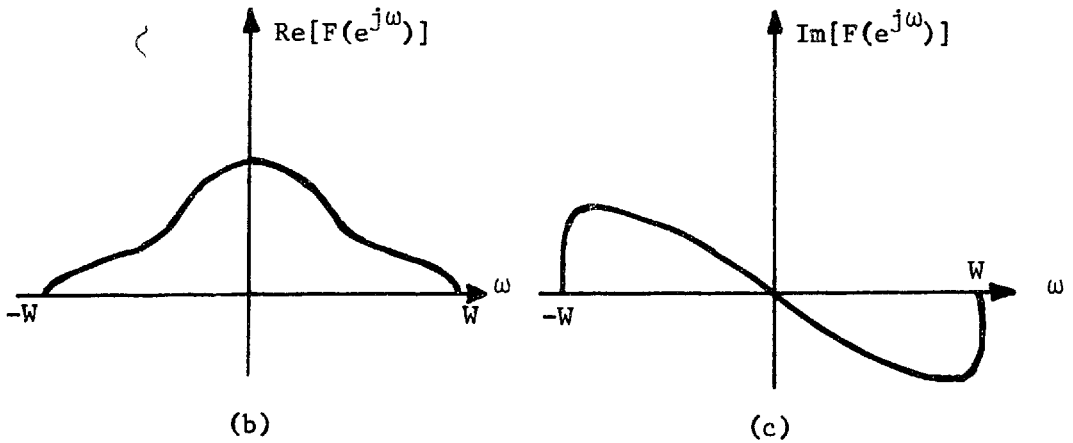
$$F(\omega_x) = \sum_{n=-\infty}^{\infty} a_n \exp[-j \frac{\pi n}{W_1} \omega_x] , \quad |\omega_x| \leq W_1 \quad (2.3)$$

where

$$a_n = \frac{1}{2W_1} \int_{-W_1}^{W_1} F(\omega_x) \exp[j \frac{\pi n}{W_1} \omega_x] d\omega_x \quad (2.4)$$



(a) $f(x)$



Real part of the
Fourier transform of $f(x)$

Imaginary part of the
Fourier transform.

Figure 2.1

An example of a bandlimited function $f(x)$
with bandwidth W .

By comparing equations (2.2) and (2.4) while remembering that $F(\omega_x) = 0$ for $|\omega_x| \geq W$, we see that

$$a_n = \frac{\pi}{W_1} f\left(\frac{n\pi}{W_1}\right) \quad (2.5)$$

This enables us to say that for a bandlimited function $f(x)$

$$F(\omega_x) = \frac{\pi}{W_1} \sum_{n=-\infty}^{\infty} f\left(\frac{n\pi}{W_1}\right) \exp\left[-j\frac{\pi n}{W_1} \omega_x\right] \quad (2.6)$$

$$f\left(\frac{n\pi}{W_1}\right) = \frac{1}{2W_1} \int_{-W_1}^{W_1} F(\omega_x) \exp\left[j\frac{\pi n}{W_1} \omega_x\right] d\omega_x$$

Thus for bandlimited space domain functions $f(x)$, $F(\omega_x)$ can be determined from samples of $f(x)$. This important result is known as the sampling theorem. The operation of obtaining the sequence of numbers $\left\{\frac{\pi}{W_1} f\left(\frac{n\pi}{W_1}\right)\right\}$ from $f(x)$ will be referred to as periodic sampling with sampling rate $2W_1$ (radians). The minimum sampling rate $2W$ consistent with the sampling theorem, will be called the Nyquist rate and the maximum distance between adjacent samples $\frac{\pi}{W}$ will be referred to as the Nyquist sampling interval.

Although the expressions of (2.6) are more convenient to use than those equations (2.1) and (2.2) they are still inadequate for computational purposes for two reasons. First we must know an infinite number of samples of $f(x)$ and secondly the inverse transform computation still requires the evaluation of an integral. We can circumvent these

difficulties by imposing the additional constraint that when $f(x)$ is sampled at its Nyquist rate only a finite number of its samples are non-zero. Although this constraint when coupled with the bandlimitedness constraint is severe, functions of this class are frequently useful as very good approximations to functions of interest. Let us further stipulate with no loss of generality that the non-zero samples of $f(x)$ are those for which $n = 0, 1, \dots, N-1$. We shall refer to N as the order of $f(x)$ and shall refer to $f(x)$ as a function of finite order if it is bandlimited and if such an N exists. If $f(x)$ is of finite order then

$$F(\omega_x) = \frac{\pi}{W} \sum_{n=0}^{N-1} f\left(\frac{n\pi}{W}\right) \exp\left[-j\frac{\pi n}{W} \omega_x\right], \quad |\omega_x| < W \quad (2.7)$$

$F(\omega_x)$ is a polynomial of degree $N-1$ in the variable $\exp\left[-j\frac{\pi}{W} \omega_x\right]$ and it is thus determined by any N samples of $F(\omega_x)$. In particular the sequence $f\left(\frac{\pi n}{W}\right)$ should be determinable from the sequence $F\left(\frac{2\pi k}{N}\right)$ for $k = 0, 1, \dots, N-1$. Consider the sum

$$\begin{aligned} & \frac{1}{N} \sum_{k=0}^{N-1} F\left(\frac{2\pi k}{N}\right) \exp\left[j\frac{2\pi k r}{N}\right], \quad r = 0, 1, \dots, N-1 \quad (2.8) \\ &= \frac{\pi}{NW} \sum_{k=0}^{N-1} \sum_{n=0}^{N-1} f\left(\frac{\pi n}{W}\right) \exp\left[-j\frac{2\pi k n}{N}\right] \exp\left[j\frac{2\pi k r}{N}\right] \\ &= \frac{\pi}{W} \sum_{n=0}^{N-1} f\left(\frac{\pi n}{W}\right) \left\{ \frac{1}{N} \sum_{k=0}^{N-1} \exp\left[j\frac{2\pi}{N}(r - n)k\right] \right\} \\ &= \frac{\pi}{W} \sum_{n=0}^{N-1} f\left(\frac{\pi n}{W}\right) \delta_{rn} \end{aligned}$$

where

$$\begin{aligned}\delta_{nn} &= 1 \quad \text{if } r = n \\ &= 0 \quad \text{if } r \neq n\end{aligned}$$

Thus

$$\frac{1}{N} \sum_{k=0}^{N-1} F\left(\frac{2Wk}{N}\right) \exp\left[j \frac{2\pi kr}{N}\right] = \frac{\pi}{W} f\left(\frac{\pi r}{W}\right), \quad r = 0, 1, \dots, N-1 \quad (2.9)$$

We can thus define a transform relation between the sequences $f\left(\frac{n\pi}{W}\right)$ defined in the space domain and $F\left(\frac{2Wk}{N}\right)$ defined in the Fourier domain.

$$F\left(\frac{2Wk}{N}\right) \triangleq \hat{F}(k) = \sum_{n=0}^{N-1} \hat{f}(n) \exp\left[-j \frac{2\pi}{N} kn\right], \quad k = 0, 1, \dots, N-1$$

$$\frac{\pi}{W} f\left(\frac{\pi n}{W}\right) \triangleq \hat{f}(n) = \frac{1}{N} \sum_{k=0}^{N-1} \hat{F}(k) \exp\left[j \frac{2\pi}{N} kn\right], \quad n = 0, 1, \dots, N-1 \quad (2.10)$$

$\hat{F}(k)$ and $\hat{f}(n)$ are said to form a discrete Fourier transform (DFT) pair.

For bandlimited functions of finite order we can thus say that samples of the function and samples of its transform form a discrete Fourier transform pair. The equations in (2.10) are extremely useful computationally and an extremely efficient algorithm, the fast Fourier transform algorithm exists for their computation.

2.1.2 The N-dimensional Fourier transform

We can derive results similar to those of section 2.1.1 for N-dimensional signals (functions of N-variables). Let $f(x_1, x_2, \dots, x_N) = f(\vec{x})$ represent a space domain function of N-dimensions for which

$$\int_{-\infty}^{\infty} |f(\vec{x})| d\vec{x} < \infty \quad (2.11)$$

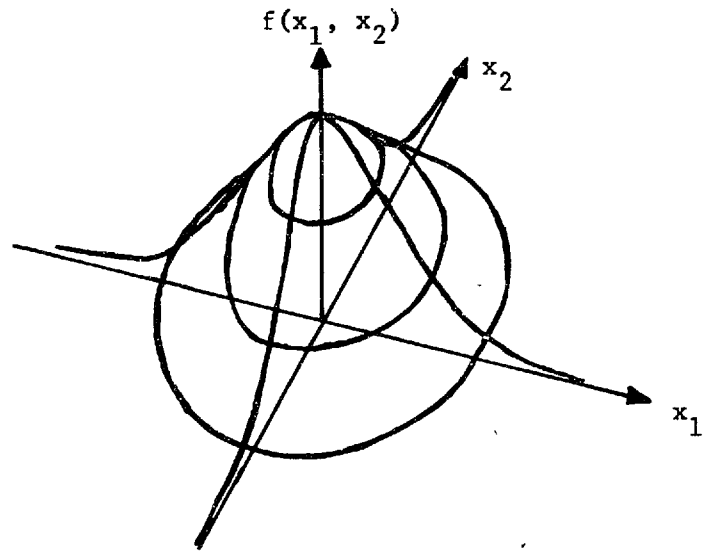
We shall use vector notation because of its notational compactness. The integral in (2.11) is meant to be carried out over the whole domain of \vec{x} and thus it represents an integral not over a line but rather over an N-dimensional volume. If we let $F(\vec{\omega}) = F(\omega_1, \omega_2, \dots, \omega_N)$ represent the N-dimensional Fourier transform of $f(\vec{x})$ then $F(\vec{\omega})$ and $f(\vec{x})$ are related by

$$F(\vec{\omega}) = \int_{-\infty}^{\infty} f(\vec{x}) \exp[-j \vec{x} \cdot \vec{\omega}] d\vec{x} \quad (2.12)$$

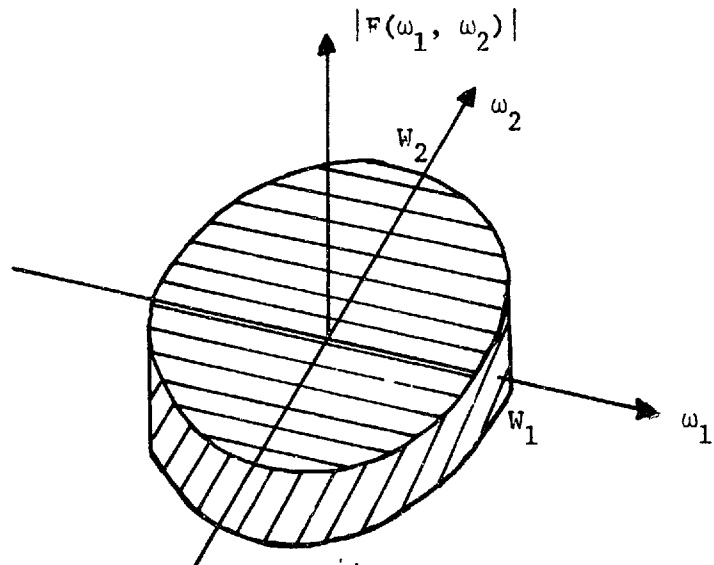
where

$$f(\vec{x}) = \frac{1}{(2\pi)^N} \int_{-\infty}^{\infty} F(\vec{\omega}) \exp[j \vec{x} \cdot \vec{\omega}] d\vec{\omega} \quad (2.13)$$

As before we shall refer to the domain of f as the space domain and the domain of F as the Fourier domain. The function $f(x_1, x_2, \dots, x_N)$ will be said to be bandlimited if there exists an N-tuple of numbers (W_1, W_2, \dots, W_N) such that $F(\omega_1, \omega_2, \dots, \omega_N) \equiv 0$ for $|\omega_1| > W_1, |\omega_2| > W_2, \dots, |\omega_N| > W_N$. A two-dimensional bandlimited function is illustrated in figure 2.2. The N-tuple of numbers $(W_1, W_2, \dots, W_{N-1})$ will be referred to as the bandwidth. It costs us little generality to set $W = \max[W_1, W_2, \dots, W_N]$ and to refer to W as the bandwidth of $f(\vec{x})$. In general this is what



(a) the function



(b) the magnitude of its Fourier transform

Figure 2.2

A two-dimensional bandlimited function.

we shall do and if the bandwidth of a multidimensional signal is specified as a scalar W , we really mean that $W = \max[W_1, W_2, \dots, W_N]$.

Since $F(\omega_1, \omega_2, \dots, \omega_N)$ is non-zero only over a limited region of Fourier space for bandlimited functions, we can expand $F(\vec{\omega}) = F(\omega_1, \omega_2, \dots, \omega_N)$ in an N -dimensional Fourier series. If $V \geq W = \max\{W_1, W_2, \dots, W_N\}$ then

$$F(\vec{\omega}) = \sum_{\vec{n}=-\infty}^{\infty} a_{\vec{n}} \exp[-j \frac{\pi}{V} \vec{n} \cdot \vec{\omega}] \quad (2.14)$$

where $\vec{n} = (n_1, n_2, \dots, n_N)$ is an N -triple of integers, each of which varies from $-\infty$ to ∞ in the N^{th} order summation. The summation is written as a single (vector) summation for convenience. Since the set of numbers $a_{\vec{n}}$ represent Fourier series coefficients, they can be determined by

$$a_{\vec{n}} = \frac{1}{(2V)^N} \int_{-V}^V F(\vec{\omega}) \exp[j \frac{\pi}{V} (\vec{n} \cdot \vec{\omega})] d\vec{\omega} \quad (2.15)$$

Comparing equations (2.13) and (2.15) as we did in the one-dimensional case, we see that

$$a_{\vec{n}} = \left(\frac{\pi}{V}\right)^N f\left(\frac{\pi}{V} \vec{n}\right) \quad (2.16)$$

Thus we can say that for a bandlimited function $f(\vec{x})$

$$F(\vec{\omega}) = \left(\frac{\pi}{V}\right)^N \sum_{\vec{n}=-\infty}^{\infty} f\left(\frac{\pi}{V} \vec{n}\right) \exp[-j \frac{\pi}{V} (\vec{n} \cdot \vec{\omega})] \quad (2.17)$$

$$f\left(\frac{\pi}{V} \vec{n}\right) = \frac{1}{(2V)^N} \int_{-V}^V F(\vec{\omega}) \exp[j \frac{\pi}{V} (\vec{n} \cdot \vec{\omega})] d\vec{\omega}$$

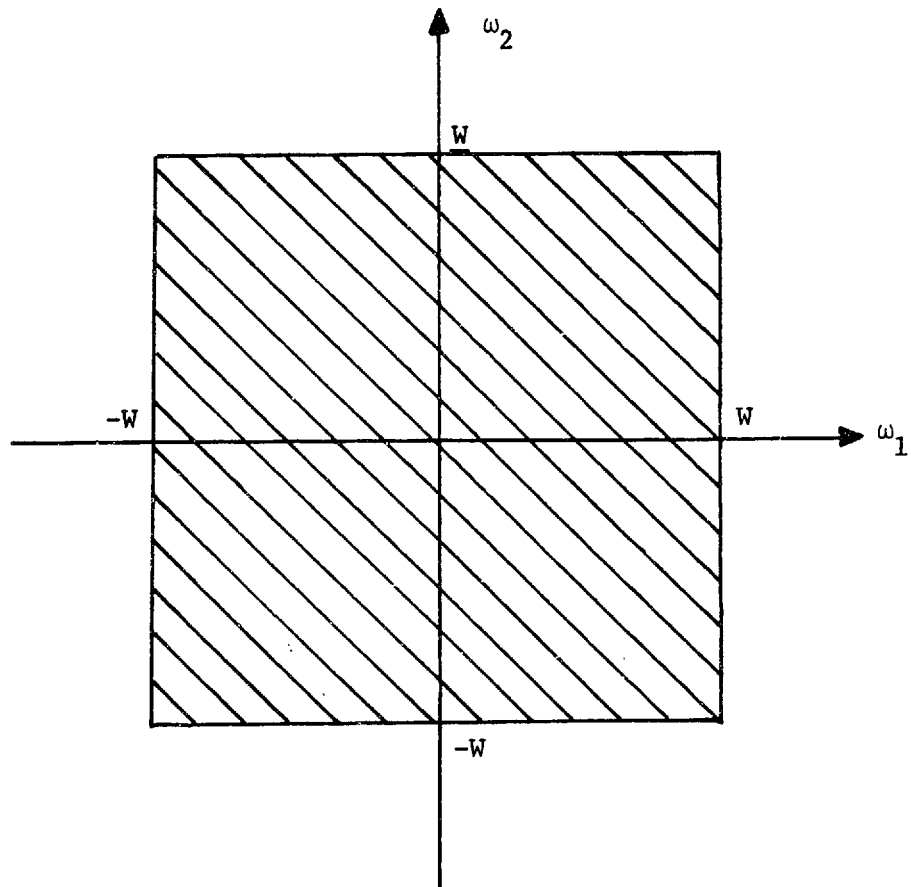


Figure 2.3

The region over which $G(e^{j\omega_1}, e^{j\omega_2})$ can be non-zero in order to apply the sampling theorem of section 2.1.2.

This is the N-dimensional sampling theorem. The operation of obtaining the multidimensional array of numbers $(\frac{\pi}{V})^N f(\frac{\pi}{W} \vec{n})$ will be referred to as periodic Cartesian sampling with sampling rate V. The term Cartesian implies that the locations of the samples in the space domain form a regular hypercubic or rectangular lattice. As in the one-dimensional case, the term Nyquist rate refers to the minimum sampling rate 2W which is consistent with the sampling theorem. Let us, as before, apply the additional constraint that only a finite number of the Cartesian samples of $f(x_1, x_2, \dots, x_N)$ when sampled at the Nyquist rate are non-zero and that with no loss of generality those samples are the ones for which $n_i = 0, 1, \dots, M-1$ where $i = 1, 2, \dots, N$. The number N shall be called the order of $f(\vec{x})$. Let us also consider the array of Cartesian samples of $F(\vec{\omega}) = F(\omega_1, \omega_2, \dots, \omega_N)$.

$$\{F(\frac{2W\vec{k}}{M})\} = F(\frac{2W}{M} k_1, \frac{2W}{M} k_2, \dots, \frac{2W}{M} k_N), k_i = 0, 1, \dots, M-1$$

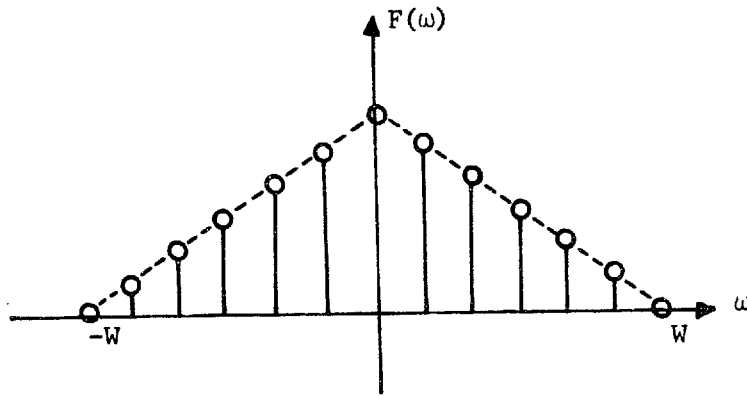
We shall now show that $f(\frac{\pi}{W} \vec{n})$ can be determined from $F(\frac{2W}{M} \vec{k})$.

Letting

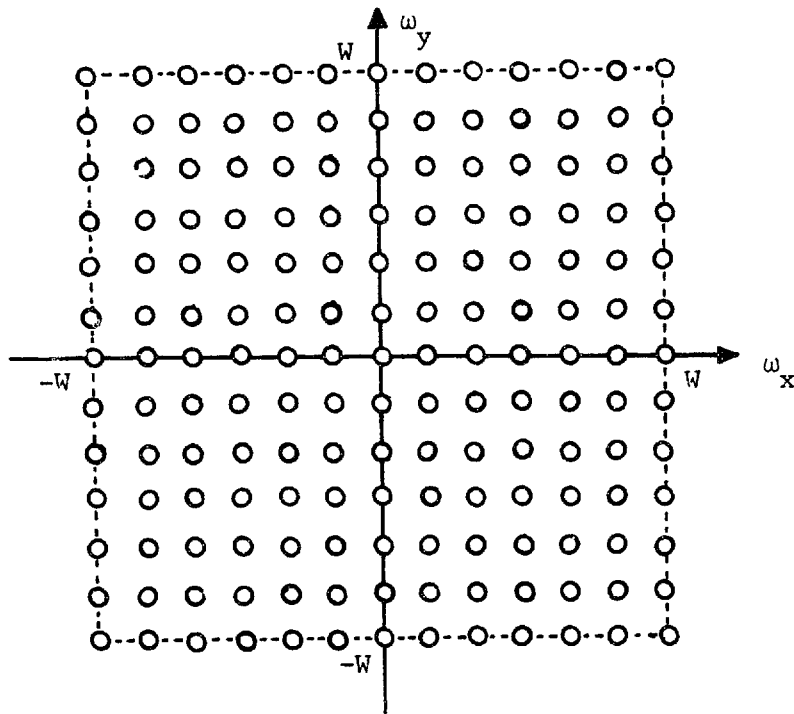
$$\sum_{\vec{k}=0}^{M-1} \text{ represent } \sum_{k_1=0}^{M-1} \sum_{k_2=0}^{M-1} \dots \sum_{k_N=0}^{M-1}$$

consider the sum

$$\frac{1}{M^N} \sum_{\vec{k}=0}^{M-1} F(\frac{2W}{M} \vec{k}) \exp[j \frac{2\pi}{M} (\vec{k} \cdot \vec{r})] \quad r_i = 0, 1, \dots, M-1 \quad (2.18)$$



(a) the location of these samples for a one-dimensional DFT



(b) the location of these samples for a two-dimensional DFT

Figure 2.4

The samples of the Fourier transform of a function which correspond to the DFT.

$$\begin{aligned}
 &= \frac{\pi^N}{M^N W^N} \sum_{\vec{k}=0}^{M-1} \sum_{\vec{n}=0}^{M-1} f\left(\frac{\pi}{W} \vec{n}\right) \exp\left[-j \frac{2\pi}{M} (\vec{k} \cdot \vec{n})\right] \exp\left[j \frac{2\pi}{M} (\vec{k} \cdot \vec{r})\right] \\
 &= \frac{\pi^N}{W^N} \sum_{\vec{n}=0}^{M-1} f\left(\frac{\pi}{W} \vec{n}\right) \frac{1}{M^N} \sum_{\vec{k}=0}^{M-1} \exp\left[j \frac{2\pi}{M} (\vec{r} - \vec{n}) \cdot \vec{k}\right] \\
 &= \frac{\pi^N}{W^N} \sum_{n_1=0}^{M-1} \sum_{n_2=0}^{M-1} \dots \sum_{n_N=0}^{M-1} f\left(\frac{\pi n_1}{W}, \frac{\pi n_2}{W}, \dots, \frac{\pi n_N}{W}\right) \delta_{r_1 n_1} \delta_{r_2 n_2} \dots \delta_{r_N n_N} \\
 &= \frac{\pi^N}{W^N} f\left(\frac{\pi r_1}{W}, \frac{\pi r_2}{W}, \dots, \frac{\pi r_N}{W}\right) = \frac{\pi^N}{W^N} f\left(\frac{\pi}{W} \vec{r}\right) \tag{2.19}
 \end{aligned}$$

Thus for N-dimensional signals of order M, the Cartesian samples of f are related to the Cartesian samples of F by a discrete Fourier transform (DFT) relation as in equations (2.20) and (2.21).

$$F\left(\frac{2W}{M} \vec{k}\right) \triangleq \hat{F}(\vec{k}) = \sum_{\vec{n}=0}^{M-1} \hat{f}(\vec{n}) \exp\left[-j \frac{2\pi}{M} (\vec{k} \cdot \vec{n})\right] \tag{2.20}$$

$$\frac{\pi^N}{W^N} f\left(\frac{\pi}{W} \vec{n}\right) \triangleq \hat{f}(\vec{n}) = \frac{1}{M^N} \sum_{\vec{k}=0}^{M-1} \hat{F}(\vec{k}) \exp\left[j \frac{2\pi}{M} (\vec{k} \cdot \vec{n})\right] \tag{2.21}$$

The fast Fourier transform (FFT) algorithm can be used to evaluate (2.20) or (2.21) in an efficient manner, for we can write (2.20) as

$$\begin{aligned}
 \hat{F}(k_1, k_2, \dots, k_N) &= \sum_{n_1=0}^{M-1} \exp\left[-j 2\pi \frac{k_1 n_1}{M}\right] \left\{ \sum_{n_2=0}^{M-1} \exp\left[-j 2\pi \frac{k_2 n_2}{M}\right] \left\{ \dots \right. \right. \\
 &\quad \left. \left. \dots \left\{ \sum_{n_N=0}^{M-1} \hat{f}(n_1, n_2, \dots, n_N) \exp\left[-j 2\pi \frac{k_N n_N}{M}\right] \right\} \right\} \right\} \tag{2.22}
 \end{aligned}$$

The inner summation is simply a one-dimensional DFT calculation which can be evaluated using the FFT with respect to the variable n_N . The results of this computation then serve as the inputs to another series of one-dimensional DFT computations, this time with respect to the variable n_{N-1} and so on. In all the number of M point DFT computations that must be performed is NM^{N-1} . Thus evaluating a multidimensional DFT is a formidable problem for N (the number of dimensions) larger than 2 or 3.

2.2 Projections

In the first chapter we considered a projection operator as a mapping of an N-dimensional function to an (N-1)-dimensional function which was obtained by superimposing all information associated with a particular direction or orientation. We defined a projection as the (N-1)-dimensional function which resulted from such an operation. Thus

$$p(x_1) = \int_{-\infty}^{\infty} f(x_1, x_2) dx_2 \quad (2.23)$$

$$q(x_2) = \int_{-\infty}^{\infty} f(x_1, x_2) dx_1 \quad (2.24)$$

$$r(x_1, x_3) = \int_{-\infty}^{\infty} f(x_1, x_2, x_3) dx_2 \quad (2.25)$$

are all examples of projections. Equations (2.23) - (2.25) do not represent the most general form for projections, however. The function $f(x_1, x_2, \dots, x_N)$ is defined on an N-dimensional vector space where the N-tuple (x_1, x_2, \dots, x_N) simply represents a point in the domain of f.

The numbers x_1, x_2, \dots, x_N simply represent coordinates with respect to some orthonormal basis. We can perform a change of variables and define another orthonormal coordinate system with respect to another orthonormal basis. We can then define projections by integrating with respect to these new variables. Let A be a matrix which accomplishes a change of coordinates from the variables x_1, x_2, \dots, x_N to the variables t_1, t_2, \dots, t_N , i.e.

$$\vec{t} = A\vec{x}$$

Since the change of coordinates must be reversible, A must be invertible so that

$$\vec{x} = A^{-1} \vec{t}$$

thus

$$f(\vec{x}) = f(A^{-1} \vec{t}) \tag{2.26}$$

The left-hand side of (2.26) expresses the function in terms of the variables x_1, x_2, \dots, x_N and the right-hand side expresses the same function in terms of the variables t_1, t_2, \dots, t_N where both sets of variables correspond to Cartesian coordinate systems. We can then define a projection as

$$p(t_1, t_2, \dots, t_{i-1}, t_{i+1}, \dots, t_N) = \int_{-\infty}^{\infty} f(A^{-1} \vec{t}) dt_i \tag{2.27}$$

The projection thus defined is N-1 dimensional. The examples in (2.23) - (2.25) are all seen to correspond to special cases where the matrix A is the identity matrix of appropriate size.

The issue of exactly what a projection is can be made clearer by considering the special case N = 2. Let $f(x_1, x_2)$ represent the function which we wish to project. We can now define a new coordinate system, the (u_1, u_2) coordinate system which is simply a rotation of the (x_1, x_2) coordinate system, as illustrated in figure 2.6a. The matrix A is

$$A = \begin{bmatrix} \cos\theta & \sin\theta \\ -\sin\theta & \cos\theta \end{bmatrix}$$

$$A^{-1} = \begin{bmatrix} \cos\theta & -\sin\theta \\ \sin\theta & \cos\theta \end{bmatrix}$$

thus

$$\begin{aligned} x_1 &= u_1 \cos\theta - u_2 \sin\theta \\ x_2 &= u_1 \sin\theta + u_2 \cos\theta \end{aligned} \tag{2.28}$$

and

$$p_\theta(u_1) = \int_{-\infty}^{\infty} f(u_1 \cos\theta - u_2 \sin\theta, u_1 \sin\theta + u_2 \cos\theta) du_2 \tag{2.29}$$

The projection is obtained by integrating along lines normal to the u_1 - axis. Equation (2.29) represents the general form for a projection in two-dimensions; the projection is completely specified by the angle θ which represents the orientation of the u_1 - axis with respect to the x_1 - axis. In general we shall thus refer to the projection of a two-dimensional function by its angle. Obtaining different projections of a two-dimensional function corresponds to finding a set of angles $\{\theta_1\}$ and taking the projection according to (2.29) for each angle.

2.2.1 Examples of Projection Functions

We stated in Chapter I that x-ray photographs and electron micrographs could be described by projections. Let us assume that we have an unknown specimen which is characterized by an optical density function $f(x,y,z)$ and that an x-ray photograph is made of the specimen with the orientation of the x-ray beam parallel to the y-axis. Furthermore let us assume that the beam is uniform with intensity I_0 , collimated, and that the effects of scattering of the beam by the specimen can be ignored. Then the observed intensity variation of the x-ray photograph can be described by

$$I(x,y) = I_0 \exp\left[- \int_{-\infty}^{\infty} f(x,y,z) dy\right] \quad (2.30)$$

where the location of the image $I(x,y)$ is assumed to lie behind the specimen. We can then define

$$p(x,y) = -\ln \frac{I(x,y)}{I_0} = \int_{-\infty}^{\infty} f(x,y,z) dy \quad (2.31)$$

and we see that $p(x,y)$ is clearly a projection of the optical density function. Other projections could easily be obtained by either altering the orientation of the specimen or changing the direction of the x-ray beam.

As a second example of a projection function, consider an idealized fan-beam scan as illustrated in figure 2.5. As with any scanning device we measure the total light intensity which passes through some aperture. The output of the scanner is the total light intensity as a function of the position of the aperture. With an idealized fan beam the aperture is very narrow in one direction and wide (infinitely wide) in the orthogonal direction. Thus the idealized fan beam scanner measures the light present along an infinitely long line. The total light passed by the beam is

$$\begin{aligned} p_0(y_0) &= \int_{-\infty}^{\infty} \int_{-\infty}^{\infty} f(x,y) U_0(y - y_0) dx dy \\ &= \int_{-\infty}^{\infty} f(x,y_0) dx \end{aligned} \quad (2.32)$$

Thus by varying y_0 over the range $(-\infty, \infty)$ we obtain a one-dimensional projection $p_c(y)$ of the light intensity of the object being scanned. By varying the orientation of the beam line we obtain different projections.

As a final example consider the response of a linear shift-variant two-dimensional system with point spread function (unit impulse response) $h(x,y)$ to a line input $U_0(x)$.

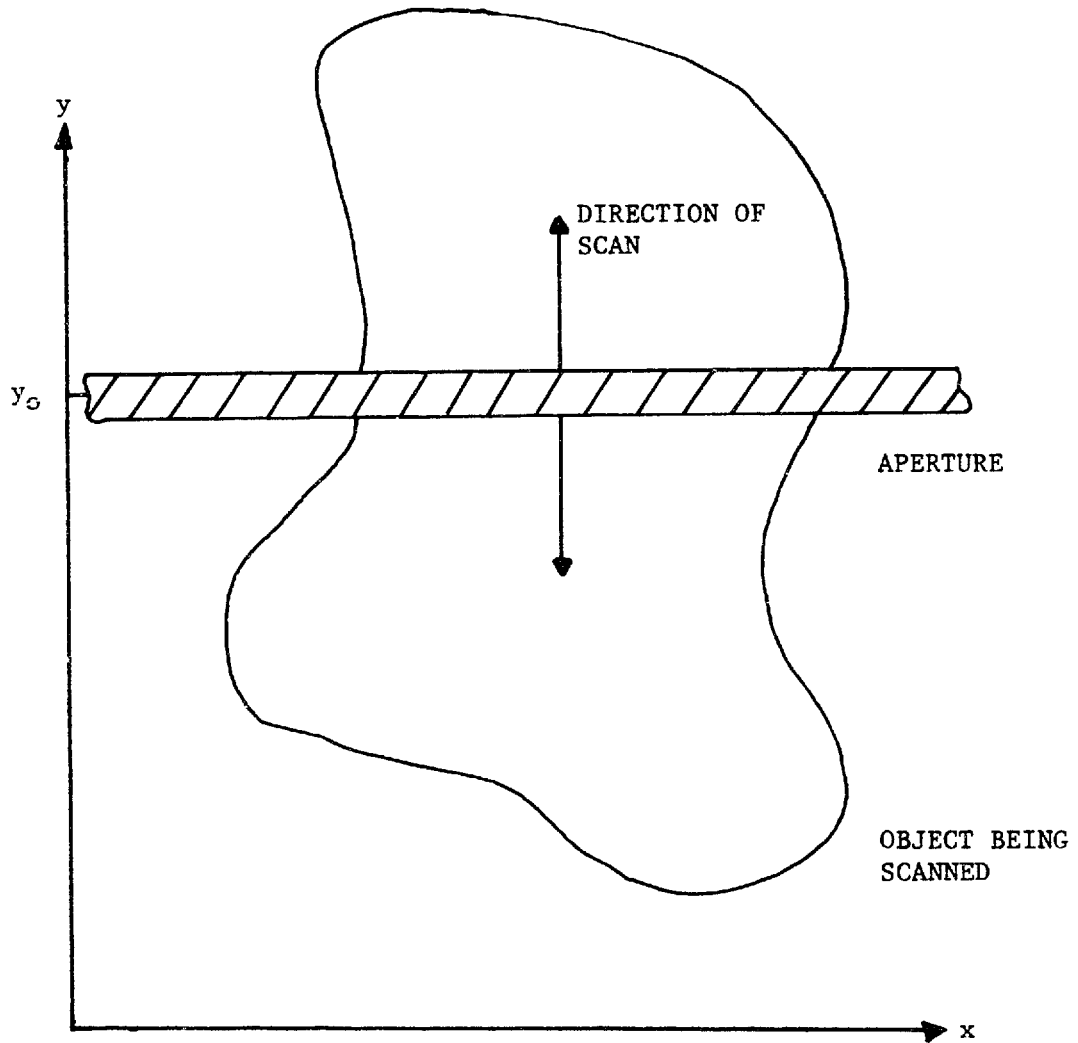


Figure 2.5

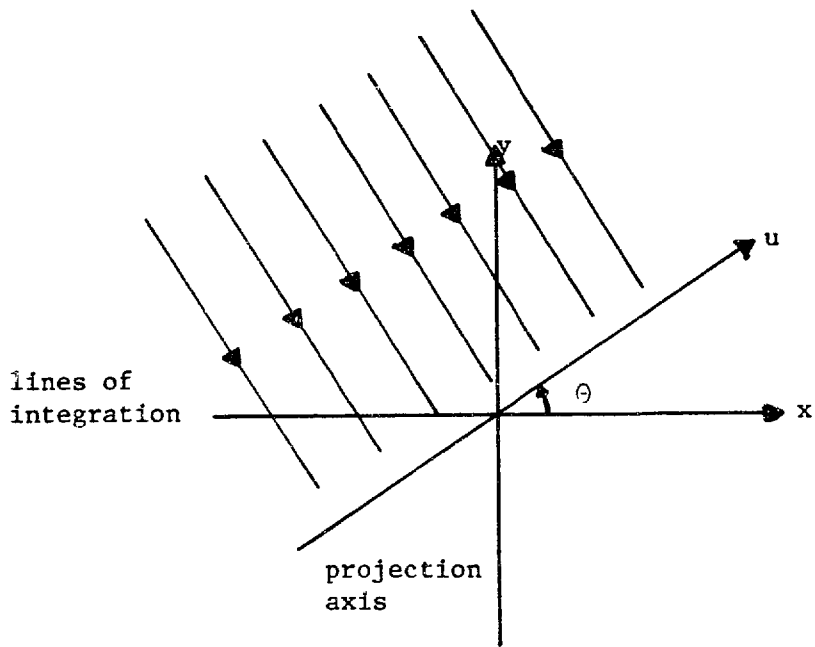
The aperture corresponding to an idealized fan-beam scan.

$$\begin{aligned}
 p_0(x,y) &= \int_{-\infty}^{\infty} h(s,t) U_0(x - s) ds dt \\
 &= \int_{-\infty}^{\infty} h(x,t) dt \\
 &\stackrel{\Delta}{=} p_0(x)
 \end{aligned}
 \tag{2.33}$$

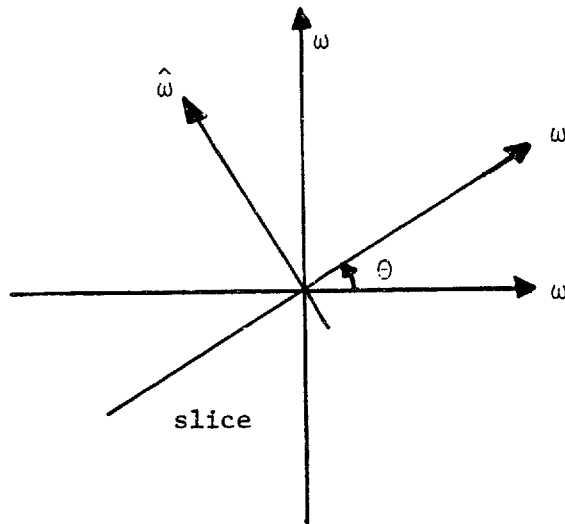
Thus the response to a line input is a two-dimensional function of one variable. Thus in this case the line spread function represents a projection function in the x-direction for every value of y. By choosing line inputs at different orientations - $U_0(u_1 \cos\theta + u_2 \sin\theta)$ we could generate other projections of the point spread function. Each of these other line responses will be uniform in the u_2 -direction and represents a projection if considered only as a function of the variable u_1 .

2.2.2 The Projection/Slice Theorem

The projection/slice theorem relates the Fourier transforms of the projections of a function to the Fourier transform of the function itself. It will serve as a basis for all of the algorithms of this thesis. We shall assume that we are working with a two-dimensional unknown since this is the case that we care most about in the examples of this thesis and since the results are simpler than the general N-dimensional case. This theorem can, however, be readily extended to three or more dimensions. We shall let $f(x,y)$ represent the function which is projected and $p_\theta(u)$ represent its projection at angle θ i.e. the u-axis intersects the x-axis at an angle θ . These relationships are illustrated in figure 2.6.



(a) the definition of a projection in the space domain



(b) the definition of a slice in the Fourier domain

Figure 2.6

The relation between a projection and a slice.

Because of the importance of this theorem we shall demonstrate it twice - first in the special case $\Theta = 0$ where we can understand what the theorem says and then again in the general case.

Case I: $\Theta = 0$

Consider $F(\omega_x, \omega_y)$, the Fourier transform of $f(x, y)$ evaluated along the ω_x -axis.

$$F(\omega_x, \omega_y) = \int_{-\infty}^{\infty} \int_{-\infty}^{\infty} f(x, y) \exp[-j(x\omega_x + y\omega_y)] dx dy \quad (2.34)$$

$$F(\omega_x, 0) = \int_{-\infty}^{\infty} \int_{-\infty}^{\infty} f(x, y) \exp[-jx\omega_x] dx dy \quad (2.35)$$

$$= \int_{-\infty}^{\infty} \exp[-jx\omega_x] \int_{-\infty}^{\infty} f(x, y) dy dx$$

$$F(\omega_x, 0) = \int_{-\infty}^{\infty} p_0(x) \exp[-j\omega_x x] dx \quad (2.36)$$

Thus the function $F(\omega_x, \omega_y)$ evaluated along the line $\omega_y = 0$ corresponds to the one-dimensional Fourier transform of the projection at $\Theta = 0$. We shall call such a section of $F(\omega_x, \omega_y)$ a slice of $F(\omega_x, \omega_y)$.

Case II: General Case

A slice of a two-dimensional Fourier transform represents $F(\omega_x, \omega_y)$ evaluated along a line which passes through the point $\omega_x = \omega_y = 0$. Each slice then is a function of a single variable which we shall call ω and each slice is characterized by a parameter Θ which represents the

angle between the ω -axis and the ω_x -axis as illustrated in figure 2.6. Equation (2.36) states that the projection at angle $\theta = 0$ transforms to the slice at $\theta = 0$. We shall show that each slice is the Fourier transform of a projection. In general the slice at angle θ transforms to the projection at angle θ . For this reason we have defined the single angle θ to represent the orientation of both a projection in the space domain and a slice in the Fourier domain.

Let $\hat{\omega}$ represent a Cartesian coordinate in the Fourier plane such that the $\omega - \hat{\omega}$ coordinate system is an orthonormal Cartesian coordinate system which is related to the $\omega_x - \omega_y$ coordinate system by a rotation of θ . Then referring to figure 2.6 we can write

$$\begin{aligned}\omega &= \omega_x \cos\theta + \omega_y \sin\theta \\ \hat{\omega} &= -\omega_x \sin\theta + \omega_y \cos\theta\end{aligned}\tag{2.37}$$

which can be inverted as

$$\begin{aligned}\omega_x &= \omega \cos\theta - \hat{\omega} \sin\theta \\ \omega_y &= \omega \sin\theta + \hat{\omega} \cos\theta\end{aligned}\tag{2.38}$$

Substituting into the expression for $F(\omega_x, \omega_y)$ we get

$$\hat{F}(\omega, \hat{\omega}) \triangleq F(\omega_x, \omega_y) = \int_{-\infty}^{\infty} \int_{-\infty}^{\infty} f(x, y) \exp[-j(x\omega \cos\theta + y\omega \sin\theta - x\hat{\omega} \sin\theta + y\hat{\omega} \cos\theta)] dx dy\tag{2.39}$$

To obtain the slice at angle θ we merely evaluate equation (2.39) along the line $\hat{\omega} = 0$.

$$\hat{F}(\omega, 0) = \int_{-\infty}^{\infty} \int_{-\infty}^{\infty} f(x, y) \exp[-j(x\omega \cos\theta + y\omega \sin\theta)] d\omega d\hat{\omega} \quad (2.40)$$

To recognize this as the Fourier transform of the projection at angle θ we can make the substitution of variables

$$\begin{aligned} u &= x \cos\theta + y \sin\theta \\ v &= -x \sin\theta + y \cos\theta \end{aligned}$$

Doing this we get

$$\hat{F}(\omega, 0) = \int_{-\infty}^{\infty} \exp[-ju\omega] \int_{-\infty}^{\infty} f(u \cos\theta - v \sin\theta, u \sin\theta + v \cos\theta) dv du \quad (2.41)$$

By comparing this with equation (2.29) we see that

$$\hat{F}(\omega, 0) = \int_{-\infty}^{\infty} \exp[-ju\omega] p_{\theta}(u) du \quad (2.42)$$

which is what we wished to prove: the slice at angle θ transforms to the projection at angle θ .

2.3 A General Reconstruction Algorithm

From the projection/slice theorem we see that specification of a projection of a signal corresponds to the specification of a slice of

that signal's Fourier transform and thus it represents a partial specification of the signal itself. In fact if we start with the inverse Fourier transform integral for a two-dimensional signal

$$f(x,y) = \frac{1}{(2\pi)^2} \int_{-\infty}^{\infty} \int_{-\infty}^{\infty} F(\omega_x, \omega_y) \exp[j(x\omega_x + y\omega_y)] d\omega_x d\omega_y \quad (2.43)$$

If we then represent $F(\omega_x, \omega_y)$ in polar coordinates

$$\begin{aligned} f(x,y) &= \frac{1}{(2\pi)^2} \int_{-\infty}^{\infty} \int_0^{\pi} F(\omega, \theta) \exp[j(x\omega \cos\theta + y\omega \sin\theta)] |\omega| d\theta d\omega \\ &= \frac{1}{(2\pi)^2} \int_{-\infty}^{\infty} \int_0^{\pi} S_{\theta}(\omega) \exp[j(x\omega \cos\theta + y\omega \sin\theta)] |\omega| d\theta d\omega \quad (2.44) \end{aligned}$$

where $S_{\theta}(\omega)$ represents the slice at angle θ . Equation (2.44) tells us how $f(x,y)$ should be reconstructed from its projections (slices). In general an infinite number of slices are needed. In practice, however, only a finite number of them will be available; thus in general equation (2.44) must be approximated from the values of $S_{\theta}(\omega)$ at only a finite number of discrete angles. Notice that from equation (2.44) only projections for $0 \leq \theta < \pi$ need to be taken. If $\pi \leq \theta < 2\pi$ then

$$\begin{aligned} p_{\theta}(u) &= \int_{-\infty}^{\infty} f(u \cos\theta - v \sin\theta, u \sin\theta + v \cos\theta) dv \\ &= \int_{-\infty}^{\infty} f(-u \cos(\theta - \pi) + v \sin(\theta - \pi), -u \sin(\theta - \pi) - v \cos(\theta - \pi)) du \end{aligned}$$

$$\begin{aligned}
 &= - \int_{-\infty}^{+\infty} f(-u \cos(\theta - \pi) - w \sin(\theta - \pi), -u \sin(\theta - \pi) + w \cos(\theta - \pi)) dw \\
 &= p_{\theta-\pi}(-u)
 \end{aligned}
 \tag{2.45}$$

From the properties of the Fourier transform it follows that if $p_{\theta}(u)$ is a real function then

$$S_{\theta}(\omega) = S_{\theta-\pi}^*(\omega)
 \tag{2.46}$$

where * denotes the complex conjugate. If, for example, eight projections were taken at evenly spaced angles from 0 to π , $F(\omega_x, \omega_y)$ would only be specified along those lines shown in figure 2.7.

In addition to requiring an infinite number of slices, equation (2.44) also requires that each slice be specified for all values of ω . This is in general impossible to do because the Fourier transforms which must be computed to determine the slices of $F(\omega_x, \omega_y)$, must be computed digitally. If the projections are all bandlimited (equivalent to requiring that $f(x,y)$ be bandlimited because of the projection/slice theorem) and if the projections can be closely approximated by functions of finite order, then samples of $S_{\theta}(\omega)$ can be computed by regular sampling of the projection $p_{\theta}(u)$ followed by a DFT calculation. This procedure will give us $F(\omega_x, \omega_y)$ at only a finite number of points on each slice. If $f(x,y)$ is not precisely bandlimited, or if the projections are not of finite order, then these samples of $F(\omega_x, \omega_y)$ will only be known approximately. Our knowledge of $F(\omega_x, \omega_y)$ will thus be confined to points such as those shown in figure 2.8. In general errors made by making approximations in

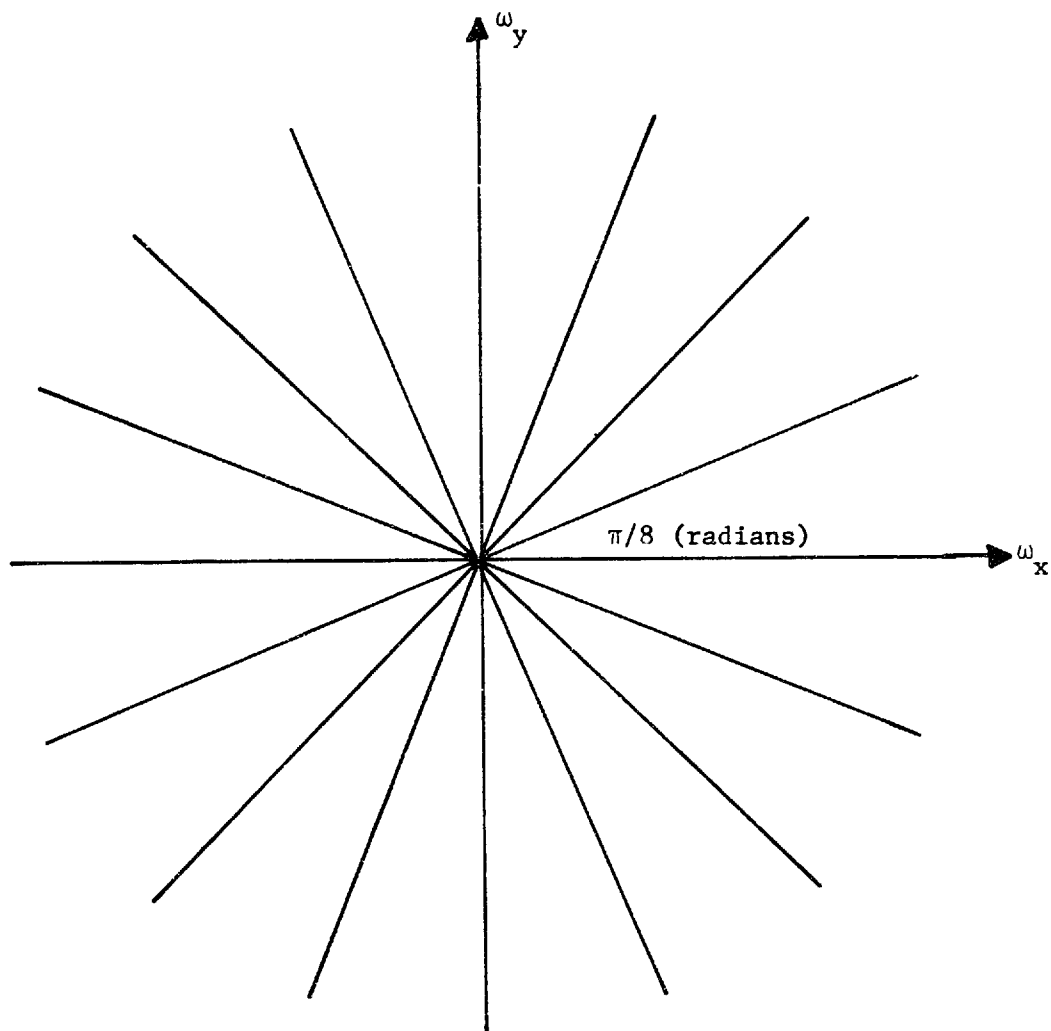


Figure 2.7

Lines in the two-dimensional Fourier plane where $F(\omega_x, \omega_y)$ would be known from 8 projections with equally spaced angles in the range $[0, \pi]$.

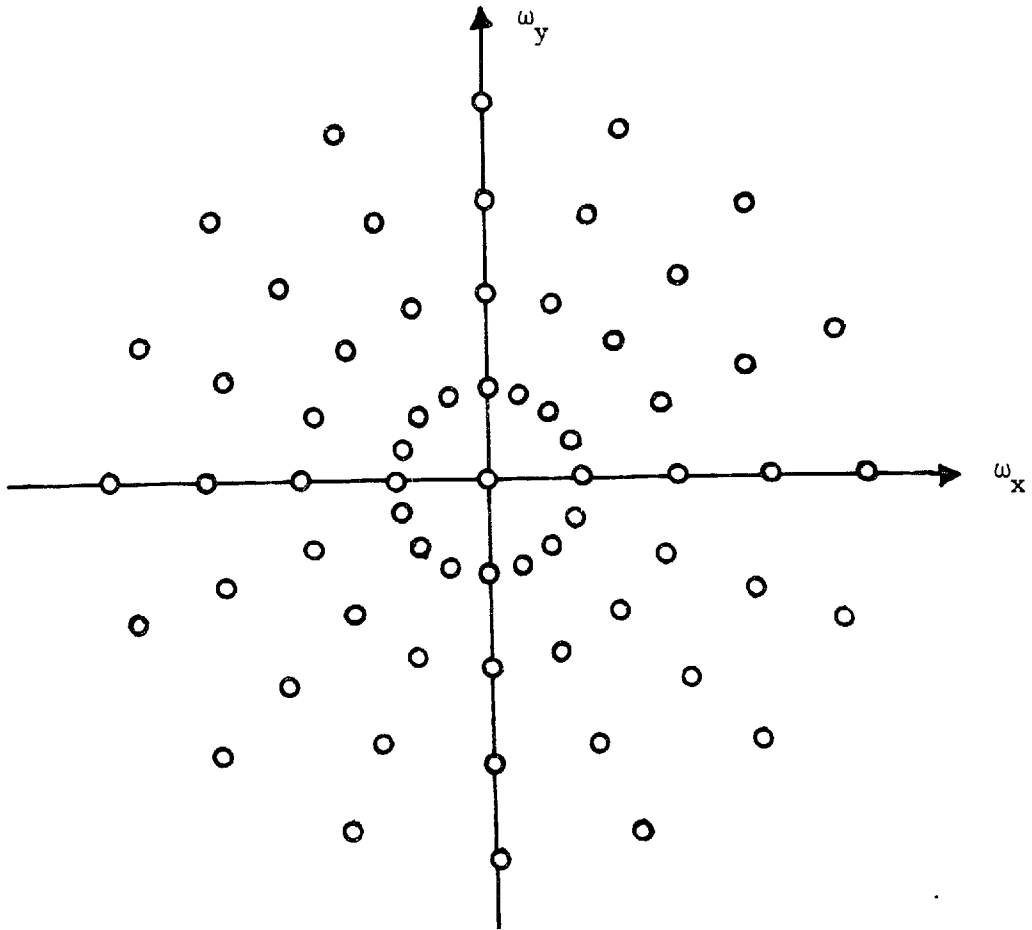


Figure 2.8

Points at which a two-dimensional Fourier transform will be known from 8 projections with the Fourier transforms computed digitally.

the ω variable seem to be less critical than those in the θ variable. Also errors made by insufficient sampling of each slice are relatively easy to correct by resampling $p_{\theta}(u)$, whereas it is considerably more difficult to obtain extra projections.

The essence of the reconstruction problem is to find some method for approximating the entire Fourier space from its values at the finite number of points that can be computed from projections. This requires that we make some assumptions about $F(\omega_x, \omega_y)$ or equivalently about $f(x, y)$. Suppose for example that we know that $f(x, y)$ is circularly symmetric. All of the projections of a circularly symmetric function must necessarily be identical, thus its slices must all be the same independent of their orientation, which is to say that $F(\omega_x, \omega_y)$ must also be circularly symmetric. Thus a circularly symmetric function can be reconstructed from a single projection. Similarly in three-dimensions an unknown which is known to be spherically symmetric, cylindrically symmetric or helically symmetric can also be reconstructed from a single two-dimensional projection. In the latter two cases the projection should be taken normal to the longitudinal axis of the cylinder or helix.

Another class of functions which can be represented exactly from a limited number of projections are the bandlimited functions of finite order. As we recall from section 2.1.2 these functions are completely determined by their DFT's, which correspond to a finite number of samples of the Fourier transforms of these functions. This finite set of Fourier samples can obviously be included in a finite number of slices and this particular set of slices can be determined by a particular set of projections which has a finite number of members. In

Chapters IV and V these functions will be considered in detail. In Chapter III some algorithms are presented which approximate more general signals. All of the reconstruction algorithms in this thesis, however, contain four basic steps.

- 1) Obtain a finite number of projections at known orientations (angles).
- 2) Sample and transform these projections.
- 3) Utilize the sampled slices to approximate the entire Fourier plane.
- 4) Inverse transform.

Some of the algorithms perform steps (3) and (4) simultaneously.

2.4 Number of Projections

There are two types of reconstruction algorithms. With the first type, called the parameter algorithms, a form is assumed for $f(x,y)$ in terms of a finite number of parameters. These parameters are then estimated from the projections and the estimates are used to perform a reconstruction. The algorithms of Chapter V are examples of such algorithms. In general we can make no statement about how many projections are needed by a parameter algorithm for this depends critically on the nature of the particular algorithm. For example one of the algorithms in Chapter V requires only one projection, where a parameter algorithm which represents $f(x,y)$ in terms of its N^2 DFT samples requires on the order of N^2 projections.

The second type of reconstruction algorithm is the class of approximation algorithms. Here the basic approach is simply to approximate

equation (2.44) from a finite number of samples of $F(\omega_x, \omega_y)$ which are available from a finite number of projections. For the approximation algorithms there are two rules of thumb that seem to be useful for picking projections.

- 1) If we have an object of dimension A and we wish to reconstruct detail to a dimension B then,

$$\# \text{ of projections} \approx \pi A/B \quad (2.47)$$

- 2) Choose the projections to be evenly spaced from 0 to π . These rules of thumb (Crowther (12), Tretiak (49), Bracewell (4)) are based on the sampling theorem and the requirement that the maximum distance between adjacent Fourier samples be less than the Nyquist interval.

2.5 Equivalence of Reconstruction and Picture Representation

In the four step reconstruction procedure outlined in the preceding section, the important and difficult step is that of approximating the entire Fourier plane from a finite number of its samples. This problem is equivalent to the problem of representing a multidimensional signal in terms of a finite number of parameters (exactly or approximately). If we approximate $f(x,y)$ by

$$f(x,y) \approx \sum_{n=0}^{N-1} a_n \psi_n(x,y) \quad (2.48)$$

then

$$F(\omega_x, \omega_y) = \sum_{n=0}^{N-1} a_n \Psi_n(\omega_x, \omega_y) \quad (2.49)$$

where $\{\psi_n(x,y)\}$ represents a set of basis functions and $\{\Psi_n(\omega_x, \omega_y)\}$ represents their two-dimensional Fourier transforms. If now the set $\{a_n\}$ can be determined from a finite number of projections (say N of them) we will have a technique for reconstructing $f(x,y)$ from N projections. In fact, the essence of the parameter reconstruction problem is to find good representations of the form of (2.48) or (2.49). Nor is this representation problem confined to performing reconstructions. It is, in fact, related to many other important disciplines such as picture coding for bandwidth compression, pattern recognition, and picture classification. Hopefully this work with reconstructions and projections can shed some light on these other disciplines.

2.6 Reducing the Three-dimensional Reconstruction Problem to a Series of Two-dimensional Problems

Another reason for directing the bulk of our discussions to the two-dimensional reconstruction problem is that the three-dimensional reconstruction can be considered as a series of two-dimensional reconstructions. In general an N dimensional reconstruction can be performed using a series of $N - 1$ dimensional reconstructions. Instead of performing a three-dimensional reconstruction by working in three-dimensional Fourier space, we can work in a hybrid $\omega_x - \omega_y - z$ space if we impose the constraint that all of the projections are to be taken normal to the z -axis. If we define

$$F(\omega_x, \omega_y, z) = \int_{-\infty}^{\infty} \int_{-\infty}^{\infty} f(x,y,z) \exp[j(x\omega_x + y\omega_y)] dx dy \quad (2.50)$$

then we can modify the projection/slice theorem at $\theta = 0$ to

$$F(\omega_x, 0, z) = \int_{-\infty}^{\infty} p_0(\mathbf{x}, z) \exp[-jx\omega_x] dx \quad (2.51)$$

and the projection/slice theorem at a general angle θ to

$$\hat{F}(\omega, \hat{\omega}, z) = F(\omega \cos\theta, \omega \sin\theta, z) = \int_{-\infty}^{\infty} p_\theta(u, z) \exp[-ju\omega] du \quad (2.52)$$

In this alternate formulation $f(x, y, z)$ can be considered to be a stack of two-dimensional functions where the variable z indexes the members of the stack. $F(\omega_x, \omega_y, z)$ then represents a stack of the two-dimensional Fourier transforms of the members of the space domain stack. Furthermore $p_\theta(x, z)$ is a stack of one-dimensional projection functions and $F(\omega \cos\theta, \omega \sin\theta, z)$ is a stack of one-dimensional slices. We can thus perform a three-dimensional reconstruction by performing a two-dimensional reconstruction for each member of the stack from its one-dimensional slices and then restack the results. This procedure requires considerably less storage and is simpler computationally than attacking the three-dimensional problem directly. Furthermore in many cases of interest, only a few members of the stack (few values of z) are required and in this case we can save computation time as well. As a result we will concern ourselves almost exclusively with two-dimensional reconstructions in the remainder of this work.

Chapter III

RECONSTRUCTING FROM A POLAR RASTER

3.1 Introduction

In section 2.3 of the previous chapter a generalized form for a reconstruction algorithm was presented which encompasses all of the algorithms that will be developed in this dissertation. First, samples of the Fourier transform of the unknown signal are computed from a set of projections. Then the unknown is estimated from these samples. The designer of an algorithm must decide upon the locations of these samples in the Fourier domain subject to the constraint that they can be computed from a limited number of projections and he must decide how the estimation of the unknown function should be made from this limited information. In this chapter attention shall be directed at the second of these problems, that of estimating $f(x,y)$ from a particular set of samples of its Fourier transform $F(\omega_x, \omega_y)$. A set of sample locations will be called a raster and here we will consider a particularly simple raster - the regular polar raster. A regular polar raster is illustrated in figure 2.8. If $F(\omega_x, \omega_y)$ is expressed in polar coordinate variables ω and θ such that $F(\omega_x, \omega_y) = F(\omega \cos\theta, \omega \sin\theta)$, then the locations of the samples of $F(\omega_x, \omega_y)$ are regularly spaced in ω and θ . Before we consider the problem of reconstructing from this raster, however, let us briefly address ourselves to the issues concerned with obtaining these polar samples.

Ideally we would like the output of any reconstruction scheme to represent an approximation to the unknown function $f(x,y)$. Digital computers, however, can only compute numbers and thus our actual output will be a set of numbers which hopefully correspond to approximate samples of $f(x,y)$. This represents no problem if there is a rule for obtaining $\hat{f}(x,y)$ (the approximation to $f(x,y)$) from its samples. This, however, limits the set of functions $\{\hat{f}(x,y)\}$ which can serve as reconstructions. The simplest such restriction which can be imposed on $\{\hat{f}(x,y)\}$ is to require that they be bandlimited. If $\hat{f}(x,y)$ is to be bandlimited and still provide an approximation to $f(x,y)$, then $f(x,y)$ must also be restricted to be bandlimited or very nearly bandlimited. In this dissertation we shall therefore restrict our attention to the reconstruction of bandlimited (or nearly bandlimited) functions. As we recall from Chapter II, a function is bandlimited if its Fourier transform is non-zero only over a finitely bounded region of Fourier space. We shall say that a function is nearly bandlimited if it has almost all of its signal energy confined to such a region or if for any $0 < \epsilon < 1$ there exists a number W_ϵ such that

$$\frac{\int_{-W_\epsilon}^{W_\epsilon} \int_{-W_\epsilon}^{W_\epsilon} |F(\omega_x, \omega_y)|^2 d\omega_x d\omega_y}{\int_{-\infty}^{\infty} \int_{-\infty}^{\infty} |F(\omega_x, \omega_y)|^2 d\omega_x d\omega_y} < 1 - \epsilon \quad (3.1)$$

This is not a particularly stringent condition since any function which has a well-defined Fourier transform is nearly bandlimited for some W_ϵ .

Equation (3.1) can be satisfied if

$$\int_{-\infty}^{\infty} \int_{-\infty}^{\infty} |F(\omega_x, \omega_y)|^2 d\omega_x d\omega_y < \infty \quad (3.2)$$

but from Schwartz's inequality

$$\int_{-\infty}^{\infty} \int_{-\infty}^{\infty} |F(\omega_x, \omega_y)|^2 d\omega_x d\omega_y \leq \left[\int_{-\infty}^{\infty} \int_{-\infty}^{\infty} |F(\omega_x, \omega_y)| d\omega_x d\omega_y \right]^2 \quad (3.3)$$

The right-hand side of (3.3) is finite, however, if $F(\omega_x, \omega_y)$ is defined, which establishes (3.2).

From the sampling theorem we recall that a bandlimited function $f(x, y)$ can be expressed in terms of its samples by

$$f(x, y) = \sum_{m=-\infty}^{\infty} \sum_{n=-\infty}^{\infty} f\left(\frac{m\pi}{W}, \frac{n\pi}{W}\right) \frac{\sin \frac{W}{\pi} \left(x - \frac{m\pi}{W}\right) \sin \frac{W}{\pi} \left(y - \frac{n\pi}{W}\right)}{\frac{W^2}{\pi^2} \left(x - \frac{m\pi}{W}\right) \left(y - \frac{n\pi}{W}\right)} \quad (3.4)$$

where W is the bandwidth of $f(x, y)$ as illustrated in figure 3.1. In the case that $f(x, y)$ is nearly bandlimited, equation (3.4) must be regarded as an approximation. In addition if $f(x, y)$ is bandlimited, then each of its projections is a one-dimensional bandlimited function, since each projection is the inverse Fourier transform of a slice of $F(\omega_x, \omega_y)$. By requiring that $f(x, y)$ be bandlimited we therefore can also guarantee that each projection be specified in terms of its samples if those samples are sufficiently close together. By appealing to figure 3.1, we see that the non-zero region of $F(\omega_x, \omega_y)$ is confined to a disc of radius $\sqrt{2} W$ in the

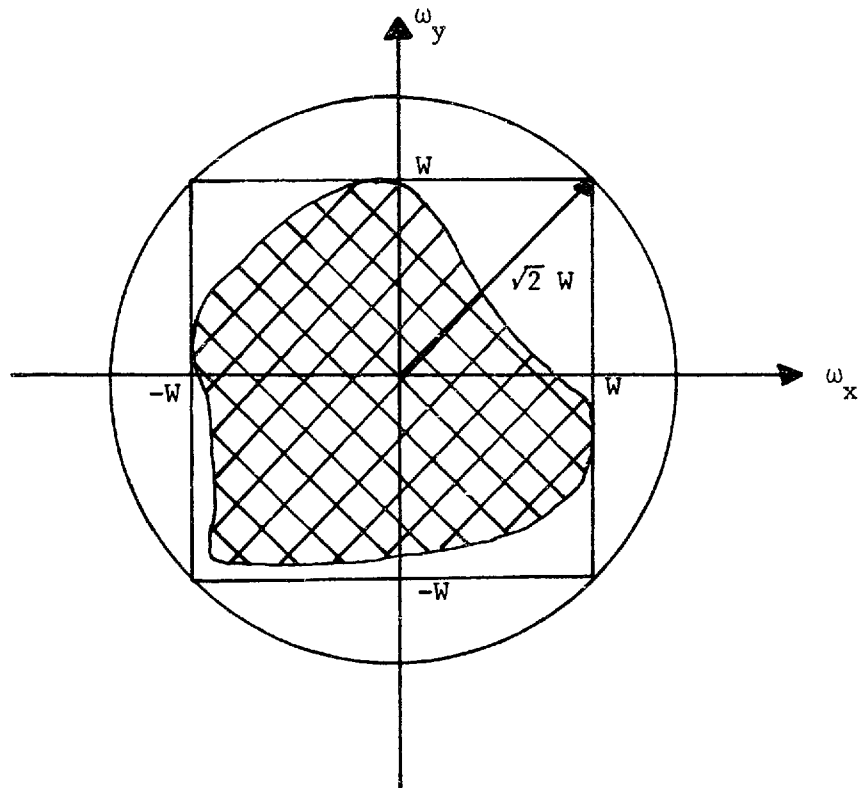


Figure 3.1

The definition of a bandlimited function.

Fourier plane. If each projection is periodically sampled with an inter-sample distance less than $\pi/\sqrt{2} W$ (meters) then each projection will be sampled faster than its Nyquist rate.

Each sampled projection represents a sequence of numbers of infinite duration. We can obtain M samples of $F(\omega_x, \omega_y)$ along the slice corresponding to a particular projection by converting that infinitely long sequence to an M point sequence by aliasing. Thus if $\{p_\theta(\frac{\pi}{\sqrt{2}W} n) \mid n = -\infty, \dots, 0, 1, \dots, \infty\}$ represents the infinitely long sequence and we define

$$\tilde{p}_\theta(n) = \sum_{m=-\infty}^{\infty} x(Mm + n) \quad n = 0, 1, \dots, M-1 \quad (3.5)$$

then $\tilde{p}_\theta(n)$ is a sequence of length M whose DFT corresponds to evenly spaced samples of the Fourier transform of $\tilde{p}_\theta(x)$. In practice the sum in (3.5) must be computed with finite limits. If this procedure is followed for each of N projections which are evenly spaced in angle over the range 0 to π , then we will know the Fourier transform $F(\omega_x, \omega_y)$ on a regular polar raster such as that in figure 2.8.

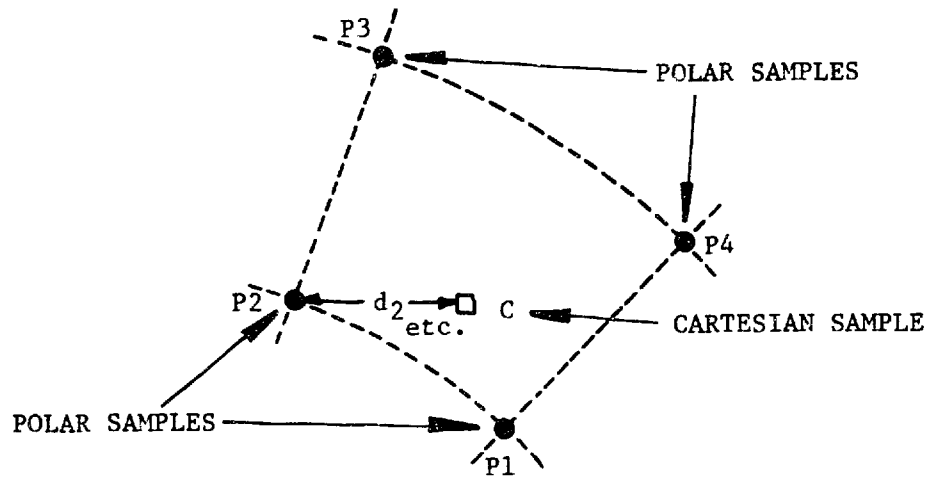
3.2 Reconstruction by Interpolation

Reconstruction by linear interpolation represents a straightforward approach to performing a reconstruction using the projection/slice theorem. Assume that the unknown signal can be represented by a bandlimited function of order N . From Chapter II this means that $f(x,y)$ is completely specified by N^2 Cartesian samples, or that the limits in the summations of equation (3.4) extend over the limited range 0 to $N-1$.

Such a function is also specified by N^2 Cartesian samples of its Fourier transform. In particular it is specified by the DFT of the array of samples of $f(x,y)$, $\{f(\frac{m\pi}{W}, \frac{n\pi}{W}), 0 \leq m, n \leq N-1\}$. Thus an $f(x,y)$ of this form can be reconstructed exactly from N^2 samples of its Fourier transform.

One can, of course, take N^2 projections of $f(x,y)$ and evaluate the Fourier transform of each at a single point. In practice this represents too many projections. If for example we wished to reconstruct a picture which can be specified by a 64 pt. x 64 pt. array, then $(64)^2 = 4096$ projections would be required. Even if we allow for the fact that some projections can be used to evaluate more than one Fourier sample, this is clearly too many projections to be practical. What would be preferred is an algorithm which can perform an approximate reconstruction from considerably fewer projections.

Suppose instead that we try to estimate the DFT samples of $F(\omega_x, \omega_y)$ from the samples on a regular polar raster. One way to do this is to use a simple form of polynomial interpolation. Two interpolation techniques have been used - zeroth-order interpolation and linear interpolation. Each of these approximations is shown in figure 3.2. With zeroth-order interpolation each Cartesian (DFT) sample is assigned the value of the nearest polar sample and with linear interpolation it is assigned a weighted average of the four nearest polar values, the weighting varying inversely with the Cartesian distance between the Cartesian sample and the polar sample in question. Referring to figure 3.3, if the Cartesian sample at (ω_x, ω_y) can be enclosed in a "square" whose vertices correspond to polar samples which are located at $(\omega_{x1}, \omega_{y1}), (\omega_{x2}, \omega_{y2}),$



ZEROth ORDER: $F(C) = F(P1)$

LINEAR:

$$F(C) = \frac{\frac{1}{d_1} F(P1) + \frac{1}{d_2} F(P2) + \frac{1}{d_3} F(P3) + \frac{1}{d_4} F(P4)}{\frac{1}{d_1} + \frac{1}{d_2} + \frac{1}{d_3} + \frac{1}{d_4}}$$

Figure 3.2

A comparison of the zeroth order and linear interpolation schemes.

$(\omega_{x3}, \omega_{y3})$ and $(\omega_{x4}, \omega_{y4})$ and if we define

$$\begin{aligned}
 d_1 &= [(\omega_x - \omega_{x1})^2 + (\omega_y - \omega_{y1})^2]^{1/2} \\
 d_2 &= [(\omega_x - \omega_{x2})^2 + (\omega_y - \omega_{y2})^2]^{1/2} \\
 d_3 &= [(\omega_x - \omega_{x3})^2 + (\omega_y - \omega_{y3})^2]^{1/2} \\
 d_4 &= [(\omega_x - \omega_{x4})^2 + (\omega_y - \omega_{y4})^2]^{1/2}
 \end{aligned}
 \tag{3.6}$$

then we set

$$\hat{F}(\omega_x, \omega_y) = \frac{\frac{1}{d_1} F(\omega_{x1}, \omega_{y1}) + \frac{1}{d_2} F(\omega_{x2}, \omega_{y2}) + \frac{1}{d_3} F(\omega_{x3}, \omega_{y3}) + \frac{1}{d_4} F(\omega_{x4}, \omega_{y4})}{\frac{1}{d_1} + \frac{1}{d_2} + \frac{1}{d_3} + \frac{1}{d_4}}
 \tag{3.7}$$

Thus the entire reconstruction algorithm can be summarized as:

- (1) Take the Fourier transform of the sampled projections using a one-dimensional DFT to obtain a collection of sampled slices of $F(\omega_x, \omega_y)$ which represent a polar sampling of $F(\omega_x, \omega_y)$.
- (2) Use zeroth-order or linear interpolation to estimate the Cartesian samples of $F(\omega_x, \omega_y)$ which correspond to a two-dimensional DFT of $\{f(\frac{m\pi}{W}, \frac{n\pi}{W}), 0 \leq m, n \leq N-1\}$.
- (3) Use a two-dimensional inverse DFT to obtain an estimate of $\{f(\frac{m\pi}{W}, \frac{n\pi}{W}), 0 \leq m, n \leq N-1\}$
- (4) Set

$$\hat{f}(x, y) = \sum_{m=0}^{N-1} \sum_{n=0}^{N-1} f\left(\frac{m\pi}{W}, \frac{n\pi}{W}\right) \frac{\sin\frac{W}{\pi}(x - \frac{m\pi}{W}) \sin\frac{W}{\pi}(y - \frac{n\pi}{W})}{\frac{W^2}{\pi^2}(x - \frac{m\pi}{W})(y - \frac{n\pi}{W})}
 \tag{3.8}$$

In figures 3.3 and 3.4 are presented some reconstructions obtained by using the above technique with zeroth-order and linear interpolation respectively. Each of these reconstructions was made from 64 evenly-spaced-in-angle computer generated projections. The original pictures from which these projections were calculated are included for comparison. Discrepancies between the reconstructions and the originals are due to two factors - errors made in computing the projections and errors made in performing the reconstruction. Since the same projections have been used to calculate all of the reconstructions in this chapter, we can say that the difference in performance of the various algorithms is due entirely to differences in the algorithms themselves and not to the projections. By comparing the reconstructions in figures 3.3 and 3.4 with those later in the chapter, we can say that most of the discrepancies in these reconstructions are due to the shortcomings of the interpolation algorithms. In computing the projections it was assumed that the original photographs represented two-dimensional bandlimited functions of order N , where the DFT computed in the reconstruction algorithm was $N \times N$.

An examination of figures 3.3 and 3.4 shows that both of these algorithms have their shortcomings although for these particular photographs the reconstructions performed using linear interpolation are better than the zeroth-order reconstructions. This is apparent in both examples and is intuitively reasonable since linear interpolation can be expected to give a better approximation to $F(\omega_x, \omega_y)$ than zeroth-order interpolation, particularly if $F(\omega_x, \omega_y)$ is continuous and slowly varying.

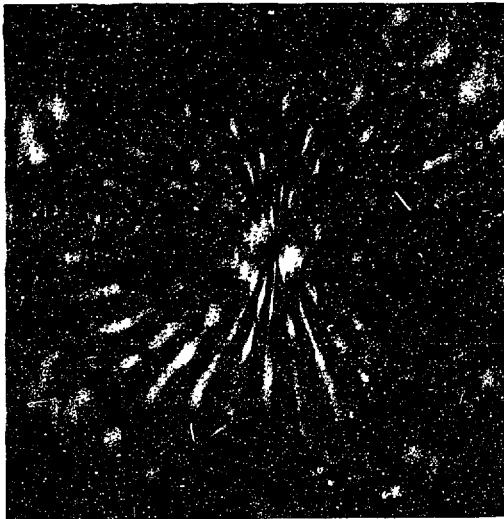
In the reconstructions by zeroth-order interpolation, the background and areas of constant gray level are irregular, considerably more



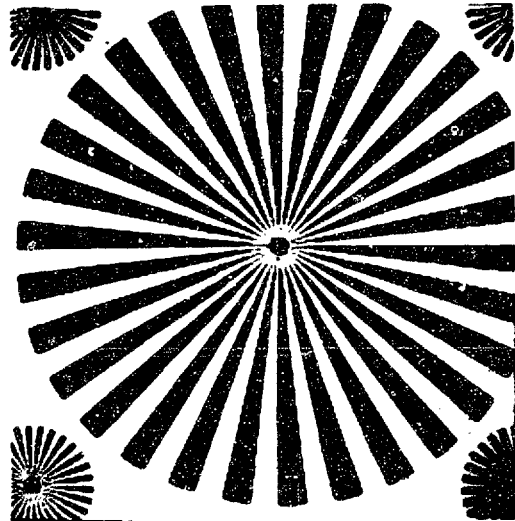
(a)



(b)



(c)



(d)

Figure 3.3

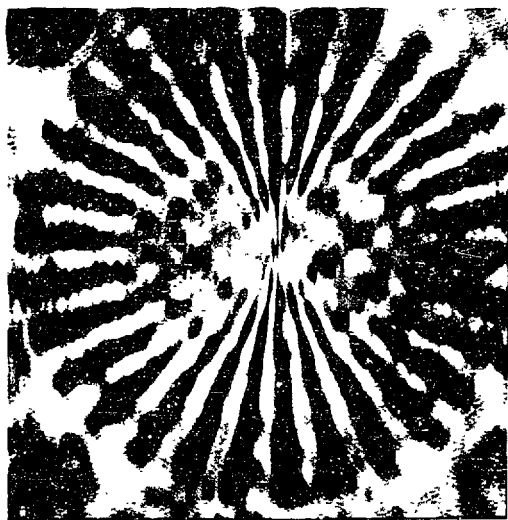
Reconstructions by zeroth order interpolation from 64 evenly spaced projections. The above are 256 x 256 sampled pictures. (a) and (c) represent reconstructions. (b) and (d) are originals.



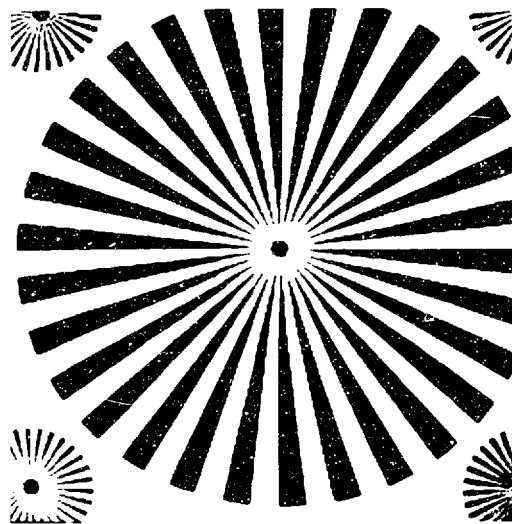
(a)



(b)



(c)



(d)

Figure 3.3

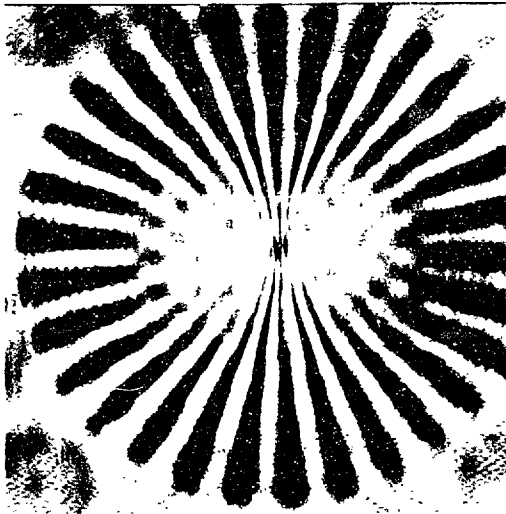
Reconstructions by zeroth order interpolation from 64 evenly spaced projections. The above are 256 x 256 sampled pictures. (a) and (c) represent reconstructions. (b) and (d) are originals.



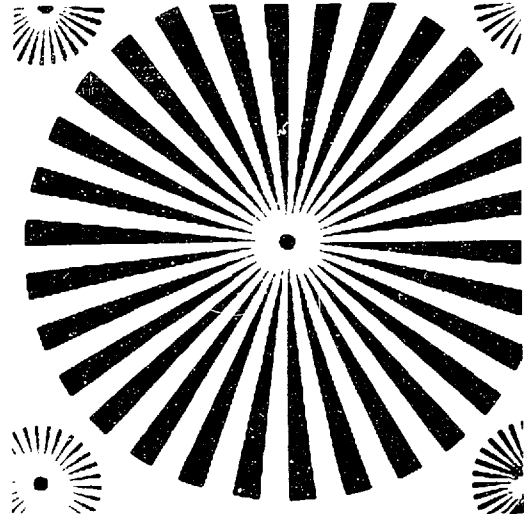
(a)



(b)



(c)



(d)

Figure 3.4

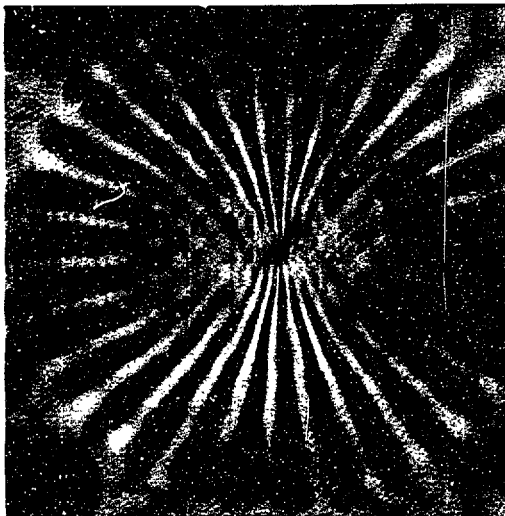
Reconstruction by linear interpolation from 64 evenly spaced projections. All of the above represent 256 x 256 sampled pictures. (a) and (c) represent reconstructions. (b) and (d) are originals.



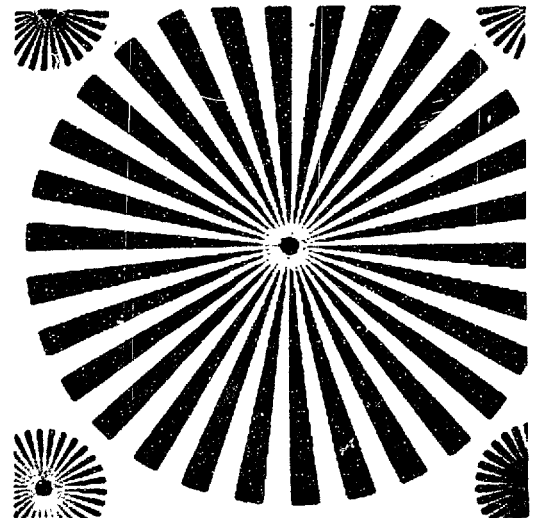
(a)



(b)



(c)



(d)

Figure 3.4

Reconstruction by linear interpolation from 64 evenly spaced projections. All of the above represent 256 x 256 sampled pictures. (a) and (c) represent reconstructions. (b) and (d) are originals.

so than in the linear interpolation examples. This is apparent in the backgrounds of both pictures and on the forehead and hair of the portrait. Edges are also not sharp nor are straight edges straight. This is evident in the mouth, nose, and mustache of the portrait and particularly in the dark rays of the test pattern. With neither technique is the center of the large test pattern or the small test patterns in the corners of that picture resolved. Neither algorithm resolves some of the fine details in each picture such as the eyes, mouth, and collar of the portrait and the details in the corners of the test pattern. Curiously both algorithms reveal an angular bias in that the vertical rays of the central test pattern are resolved better than the horizontal ones. This is believed to be due to the interaction between the asymmetries in the original and the interpolation algorithms.

Remembering that one of the reasons for performing multidimensional reconstructions is to resolve unknown signals, it can be said that all of these examples seem to give us some information about the unknown signals that could in many cases be valuable. The reconstructions in 3.3a and 3.4a are both clearly of a man's face, for example.

3.3 Reconstruction by Interpolation in Polar Coordinates

One of the possible explanations for the errors that were introduced by the algorithms of the previous section is that not enough projections were taken. Indeed it was noted experimentally that as the number of projections was increased the quality of the reconstructions improved. In most practical situations, however, obtaining extra projections is a major effort; it is sometimes even impossible. Instead of

physically taking extra projections of the unknown, it might be possible to compute extra projections from the ones that are already available. From this extended set of projection/slices linear interpolation could then be used. If these extra projections were computed from the original set by linear or zeroth-order interpolation, then our reconstructions would be identical to those of the previous section, but if we use some other interpolation scheme different and hopefully improved reconstructions should be obtained. This is the central idea behind the interpolation in polar coordinates (IPC) algorithm.

Suppose we sample $f(x,y)$ in a generalized fashion so that

$$f(x,y) = \sum_{m=-\infty}^{\infty} \sum_{n=-\infty}^{\infty} f_{mn} \phi_{mn}(x,y) \quad (3.9)$$

The two dimensional sequence $\{f_{mn}\}$ corresponds to the "samples" of $f(x,y)$ and the set of basis functions $\{\phi_{mn}(x,y)\}$ determines the nature of the representation. The class of functions $f(x,y)$ which can be represented as in 3.9 will depend upon the basis $\{\phi_{mn}(x,y)\}$ as will the technique for sampling $f(x,y)$. In the special case of periodic sampling we choose

$$f_{mn} = \frac{\pi^2}{W^2} f\left(\frac{m\pi}{W}, \frac{n\pi}{W}\right)$$

$$\phi_{mn}(x,y) = \frac{\sin\frac{W}{\pi}\left(x - \frac{m\pi}{W}\right) \sin\frac{W}{\pi}\left(y - \frac{n\pi}{W}\right)}{\left(x - \frac{m\pi}{W}\right)\left(y - \frac{n\pi}{W}\right)} \quad (3.10)$$

This particular choice of a basis allows us to compute $\{f_{mn}\}$ by periodic sampling but constrains us to represent only bandlimited functions with bandwidth W or less.

Equation (3.9) is a linear relation and thus we can expand $F(\omega_x, \omega_y)$, the Fourier transform of $f(x, y)$, according to

$$F(\omega_x, \omega_y) = \sum_{m=-\infty}^{\infty} \sum_{n=-\infty}^{\infty} f_{mn} \phi_{mn}(\omega_x, \omega_y) \quad (3.11)$$

where $\phi_{mn}(\omega_x, \omega_y)$ is the two-dimensional Fourier transform of $\phi_{mn}(x, y)$.

If we rewrite (3.11) in terms of polar coordinates then

$$F(\omega \cos \theta, \omega \sin \theta) = F_p(\omega, \theta) = \sum_{m=-\infty}^{\infty} \sum_{n=-\infty}^{\infty} f_{mn} \psi_{mn}(\omega, \theta) \quad (3.12)$$

and equation (3.9) becomes

$$f(r \cos \phi, r \sin \phi) = f_p(r, \phi) = \sum_{m=-\infty}^{\infty} \sum_{n=-\infty}^{\infty} f_{mn} \psi_{mn}(r, \phi) \quad (3.13)$$

where

$$\psi_{mn}(r, \phi) = \frac{1}{4\pi^2} \int_{-\pi}^{\pi} \int_0^{\infty} \psi_{mn}(\omega, \theta) \{\exp[j\omega r \cos(\phi - \theta)]\} \omega \, d\omega \, d\theta \quad (3.14)$$

We now wish to choose a set of basis functions $\{\psi_{mn}(r, \phi)\}$ such that a finite subset of $\{\psi_{mn}(r, \phi)\}$ will provide a good approximation to

$f_p(r, \phi)$ and also so that the coefficients $\{f_{mn}\}$ can be readily computed from a finite number of projections. Let us choose $\{\psi_{mn}(r, \phi)\}$ so that

$$\psi_{mn}(\omega, \theta) = \exp\left[j\left(\frac{2\pi\omega m}{\sqrt{2}W} + n\theta\right)\right] p_W(\omega) \quad (3.15)$$

where

$$p_W(\omega) = \begin{cases} 1 & 0 \leq \omega < \sqrt{2}W \\ 0 & \text{otherwise} \end{cases}$$

The reasons for this choice are threefold. First these functions are the Fourier transforms of bandlimited functions and furthermore the non-zero region of $\psi_{mn}(\omega, \theta)$ is confined to the disk in the Fourier plane of radius $\sqrt{2}W$. Thus $F_p(\omega, \theta)$ or $F(\omega_x, \omega_y)$ must be bandlimited and it must be confined to the same disk. This will allow us to use sampled projections to compute the $\{f_{mn}\}$. Secondly as will be demonstrated shortly, this choice for a basis will allow the $\{f_{mn}\}$ to be computed straightforwardly from sampled slices of $F(\omega_x, \omega_y)$. Finally these functions are complete over the set of real bandlimited functions and good approximations to $F(\omega_x, \omega_y)$ can often be obtained from only a few members of the set $\{\psi_{mn}(\omega_x, \omega_y)\}$.

We can demonstrate the completeness of $\{\psi_{mn}(\omega, \theta)\}$ by means of the following argument. Let

$$f_{mn} = \frac{\sqrt{2}W}{2\pi} \int_0^{\sqrt{2}W} \int_{-\pi}^{\pi} F_p(\omega, \theta) \exp\left[-j\left(\frac{2\pi m\omega}{\sqrt{2}W} + n\theta\right)\right] d\theta d\omega \quad (3.16)$$

Substituting equation (3.16) into equation (3.12) we get

$$G(\omega, \theta) = \sum_{m=-\infty}^{\infty} \sum_{n=-\infty}^{\infty} \frac{\sqrt{2} W}{2\pi} \int_0^{\sqrt{2}W} \int_{-\pi}^{\pi} F_p(\alpha, \beta) \exp[-j(\frac{2\pi m\alpha}{\sqrt{2} W} + n\beta)] \exp[j(\frac{2\pi m\omega}{\sqrt{2} W} + n\theta)] d\beta d\alpha \quad (3.17)$$

where we wish to show that $G(\omega, \theta) = F_p(\omega, \theta)$. Interchanging the summations and the integrations, we get

$$G(\omega, \theta) = \frac{\sqrt{2} W}{2\pi} \int_0^{\sqrt{2}W} \int_{-\pi}^{\pi} F_p(\alpha, \beta) \left\{ \sum_{m=-\infty}^{\infty} \exp[j \frac{2\pi m}{\sqrt{2}W} (\omega - \alpha)] \right\} \left\{ \sum_{n=-\infty}^{\infty} \exp[jn(\theta - \beta)] \right\} d\beta d\alpha \quad (3.18)$$

We can now notice that each of the summations in braces corresponds to the Fourier series expansion of a train of delta functions. Thus

$$\sum_{m=-\infty}^{\infty} \exp[j \frac{2\pi m}{\sqrt{2}W} (\omega - \alpha)] = \sqrt{2}W \sum_{s=-\infty}^{\infty} \delta(\omega - \alpha - \sqrt{2}Ws) \quad (3.19)$$

$$\sum_{n=-\infty}^{\infty} \exp[jn(\theta - \beta)] = \frac{1}{2\pi} \sum_{t=-\infty}^{\infty} \delta(\theta - \beta - 2\pi t) \quad (3.20)$$

By substituting (3.19) and (3.20) into (3.18),

$$G(\omega, \theta) = \int_0^{\sqrt{2}W} \int_{-\pi}^{\pi} F_p(\alpha, \beta) \sum_{s=-\infty}^{\infty} \delta(\omega - \alpha - \sqrt{2}Ws) \sum_{t=-\infty}^{\infty} \delta(\theta - \beta - 2\pi t) d\beta d\alpha \quad (3.21)$$

But the ranges of α , β , ω and Θ are constrained such that

$$0 \leq \alpha < \sqrt{2W} \quad (3.22a)$$

$$0 \leq \omega < \sqrt{2W} \quad (3.22b)$$

$$-\pi < \beta \leq \pi \quad (3.22c)$$

$$-\pi < \Theta \leq \pi \quad (3.22d)$$

It thus follows that

$$G(\omega, \Theta) = F_p(\omega, \Theta)$$

which is what we wished to show. Thus the set $\{\phi_{mn}(\omega_x, \omega_y)\}$ is complete on the set of bandlimited functions for which $F(\omega_x, \omega_y)$ is confined to a disk of radius $\sqrt{2W}$. In addition we see from (3.16) how the $\{f_{mn}\}$ should be chosen.

From this demonstration we further see that representing $F(\omega_x, \omega_y)$ exactly requires an infinite number of basis functions in general. This in turn requires an infinite number of projections in order that the $\{f_{mn}\}$ can be computed. Let us therefore make the approximation

$$F_p(\omega, \Theta) \approx \sum_{m=-M/2+1}^{M/2} \sum_{n=-N/2+1}^{N/2} f_{mn} \exp\left[j\left(\frac{2\pi m\omega}{\sqrt{2}W} + n\Theta\right)\right] p_W(\omega) \quad (3.23)$$

From the projections (slices), samples of $F_p(\omega, \Theta)$ are known on a polar raster, i.e., $F_p(\omega, \Theta)$ is known at points $F_p\left(\frac{\sqrt{2}W}{M}a, \frac{2\pi}{N}b\right)$ for $a = 0, 1, \dots, M-1$ and $b = 0, 1, \dots, N-1$. From these values we can set

up a series of linear equations which can be solved for f_{mn} .

$$F_p \left(\frac{\sqrt{2W}}{M} a, \frac{2\pi}{N} b \right) = \sum_{m=-M/2+1}^{M/2} \sum_{n=-N/2+1}^{N/2} f_{mn} \exp \left[j \left(\frac{2\pi m a}{M} + \frac{2\pi n b}{N} \right) \right] \quad (3.24)$$

$$a = 0, 1, \dots, M-1$$

$$b = 0, 1, \dots, N-1$$

If this is done it can be seen that

$$f_{mn} = \frac{1}{MN} \sum_{a=0}^{M-1} \sum_{b=0}^{N-1} F_p \left(\frac{\sqrt{2W}}{M} a, \frac{2\pi}{N} b \right) \exp \left[-j 2\pi \left(\frac{m a}{M} + \frac{n b}{N} \right) \right] \quad (3.25)$$

The validity of (3.25) can be demonstrated by means of the following:

$$\frac{1}{MN} \sum_{a=0}^{M-1} \sum_{b=0}^{N-1} F_p \left(\frac{\sqrt{2W}}{M} a, \frac{2\pi}{N} b \right) \exp \left[-j 2\pi \left(\frac{m a}{M} + \frac{n b}{N} \right) \right] \quad (3.26)$$

$$= \frac{1}{MN} \sum_{a=0}^{M-1} \sum_{b=0}^{N-1} \sum_{s=-M/2+1}^{M/2} \sum_{t=-N/2+1}^{N/2} f_{st} \exp \left[j 2\pi \left(\frac{s a}{M} + \frac{t b}{N} - \frac{m a}{M} - \frac{n b}{N} \right) \right] \quad (3.27)$$

$$= \frac{1}{MN} \sum_{s=-M/2+1}^{M/2} \sum_{t=-N/2+1}^{N/2} f_{st} \left\{ \sum_{a=0}^{M-1} \exp \left[j \frac{2\pi a}{M} (s - m) \right] \right\} \left\{ \sum_{b=0}^{N-1} \exp \left[j \frac{2\pi b}{N} (t - n) \right] \right\} \quad (3.28)$$

$$= \frac{1}{MN} \sum_{s=-M/2+1}^{M/2} \sum_{t=-N/2+1}^{N/2} MN \delta_{sm} \delta_{tn} \quad (3.29)$$

$$= f_{mn}$$

Remembering that $F_p(\frac{\sqrt{2}Wa}{M}, \frac{2\pi}{N} b)$ corresponds to samples of $F(\omega_x, \omega_y)$ on a polar raster, we see that these numbers are available from $N/2$ evenly spaced projections. Furthermore (3.25) is of the form of a two-dimensional DFT. Thus to obtain the two-dimensional sequence f_{mn} from the sequence $\{F_p(\frac{\sqrt{2}Wa}{M}, \frac{2\pi}{N} b)\}$ it is sufficient to take the two-dimensional DFT of the latter sequence as if that sequence consisted of Cartesian samples rather than polar ones! Once that we have the sequence f_{mn} we can reconstruct the picture function $f_p(r, \phi)$ either by means of (3.13) or (3.12) followed by an inverse Fourier transform. The latter technique is easier to implement because it does not require the computation of the $\{\psi_{mn}(r, \phi)\}$ which can be a formidable calculation. Thus we shall use (3.12) to compute the DFT samples corresponding to an estimate of $f(x, y)$ and then evaluate an inverse DFT. This approach is computationally straightforward.

We can evaluate $F(\omega_x, \omega_y) = F_p(\omega, \theta)$ at any point because

$$F_p(\omega, \theta) \approx \sum_{m=-M/2+1}^{M/2} \sum_{n=-N/2+1}^{N/2} f_{mn} \psi_{mn}(\omega, \theta) \quad (3.30)$$

or

$$F_p(\omega, \theta) \approx \sum_{m=-M/2+1}^{M/2} \sum_{n=-N/2+1}^{N/2} \frac{1}{MN} \sum_{a=0}^{M-1} \sum_{b=0}^{N-1} F_p(\frac{\sqrt{2}W}{M} a, \frac{2\pi}{N} b) \exp[-j2\pi(\frac{ma}{M} + \frac{nb}{N})] \times \exp[j(\frac{2\pi m\omega}{\sqrt{2}W} + n\theta)] p_W(\omega) \quad (3.31)$$

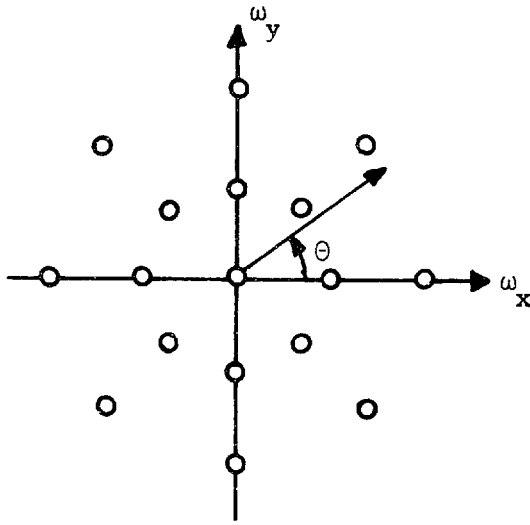
$$= \sum_{a=0}^{M-1} \sum_{b=0}^{N-1} F_p(\frac{\sqrt{2}W}{M} a, \frac{2\pi}{N} b) \frac{1}{M} \sum_{m=-M/2+1}^{M/2} \exp[j2\pi(\frac{\omega}{\sqrt{2}W} - \frac{a}{M})] \frac{1}{N} \sum_{n=-N/2+1}^{N/2} \exp[jn(\theta - \frac{2\pi b}{N})] p_W(\omega) \quad (3.32)$$

$$= \sum_{a=0}^{M-1} \sum_{b=0}^{N-1} F_p \left(\frac{\sqrt{2W}}{M} a, \frac{2\pi}{N} b \right) \exp \left[-j \left(\pi \left(\frac{\omega}{\sqrt{2W}} - \frac{a}{M} \right) + \frac{1}{2} \left(\Theta - \frac{2\pi b}{N} \right) \right) \right] x$$

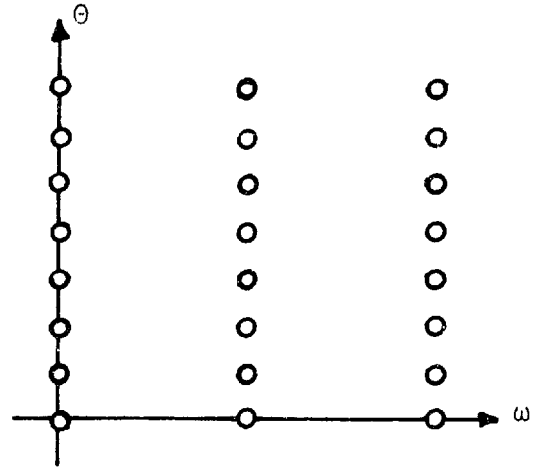
$$\frac{\sin \pi M \left(\frac{\omega}{\sqrt{2W}} - \frac{a}{M} \right) \sin \frac{N}{2} \left(\Theta - \frac{2\pi b}{N} \right)}{MN \sin \pi \left(\frac{\omega}{\sqrt{2W}} - \frac{a}{M} \right) \sin \frac{1}{2} \left(\Theta - \frac{2\pi b}{N} \right)} P_W(\omega) \quad (3.33)$$

Equation (3.33) is simply an expression for the bandlimited interpolation of a function $F_p(\omega, \Theta)$ in terms of two "Cartesian" variables ω and Θ . Note that it is $F_p(\omega, \Theta)$ which is to be considered bandlimited in this strange sense, not $f_p(r, \phi)$.

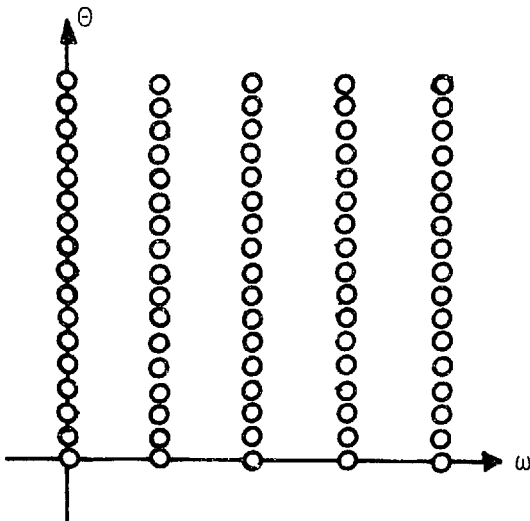
Instead of plugging into equation (3.33), however, we can formulate a reconstruction algorithm as illustrated in figure 3.5. First a set of $N/2$ evenly spaced (in angle) slices are obtained from projections in the usual manner and from these, additional slices are computed in the following fashion. The polar samples are mapped into a Cartesian coordinate system where ω and Θ are considered as Cartesian variables. Then using bandlimited interpolation (which can be implemented using a DFT) additional "Cartesian" samples are computed between the ones already available. This dense Cartesian grid of samples is then mapped back to the Fourier plane. From this dense set of sample values, linear interpolation can then be used to obtain an approximation to the DFT of $f(x, y)$, samples of which are then available by performing an inverse DFT. Hopefully the errors introduced by linear interpolation from this denser polar grid will be smaller than those induced by straightforward linear interpolation so that our reconstructions will be better.



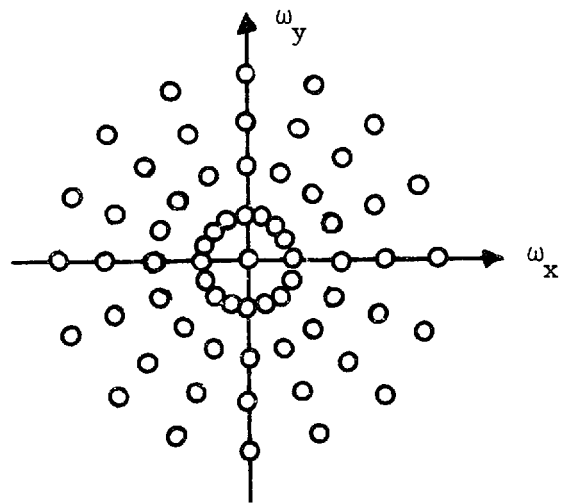
(a) original set of polar samples



(b) point mapped to "Cartesian" coordinates



(c) extra points computed by bandlimited interpolation



(d) final polar raster

Figure 3.5

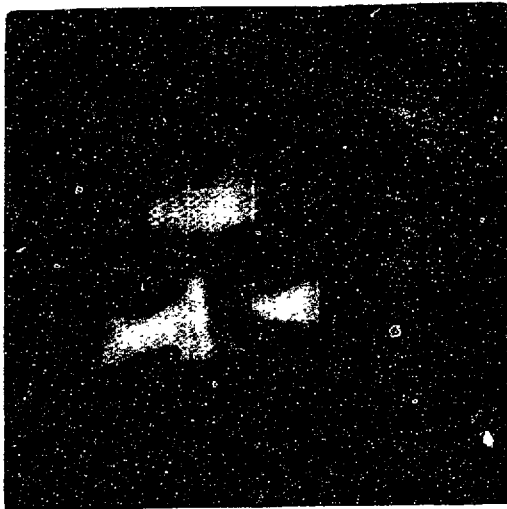
The reconstruction algorithm based on interpolation in polar coordinates.

In figure 3.6 are some reconstructions made using this algorithm. From the unknown, 64 projections of 256 samples apiece were computed. These projections were thus identical to those used in section 3.2. From these 192 additional projections of 256 points apiece were computed and then linear interpolation was used as in the previous section. If these reconstructions are compared with those of figure 3.4 we see that the IPC scheme gives little improvement over straightforward linear interpolation. The portrait reconstructions in 3.6a and 3.4a are virtually identical, although differences in performance can be seen for the test pattern reconstructions. The IPC algorithm reconstructs horizontal rays in the test pattern as well as vertical ones, in marked contrast to the linear interpolation algorithm. Also the pattern in the lower left hand corner of the test pattern has been partially resolved using IPC but not using linear interpolation. On the basis of these restricted examples we might infer that this algorithm might be preferable to linear interpolation when $f(x,y)$ is believed to exhibit some circular symmetry. This is of course equivalent to requiring that equation 3.23 hold. This is perhaps a valid assumption in the reconstruction of viruses from electron micrographs, since viruses exhibit much symmetry.

The IPC algorithm is similar in many ways to the Hankel transform algorithms which are presented in section 3.5.

3.4 Reconstruction by Smearing

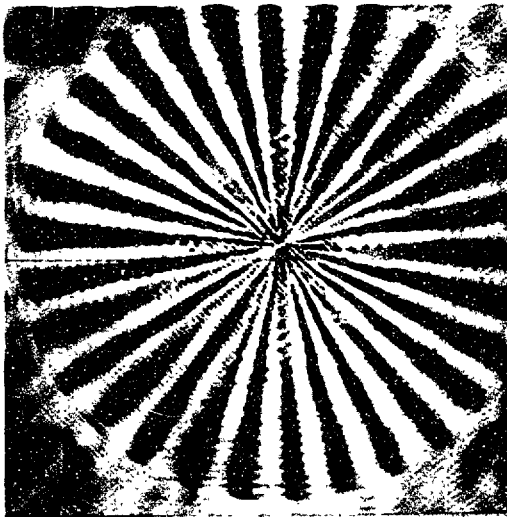
A standard procedure for estimating the value of an integral is to approximate the integral by a summation, the terms of which are proportional to samples of the integrand. This is what we shall do in



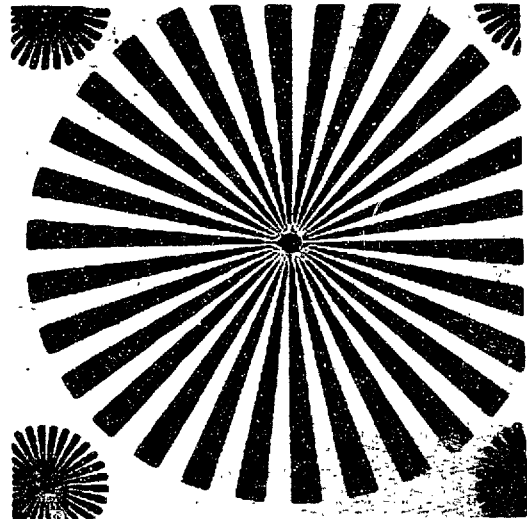
(a)



(b)



(c)



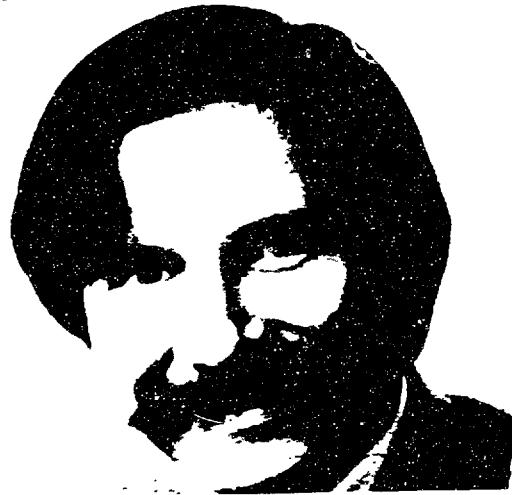
(d)

Figure 3.6

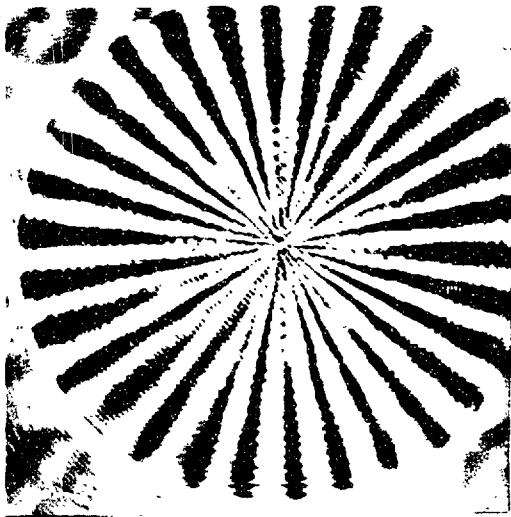
Reconstructions by interpolation in polar coordinates followed by linear interpolation. (a) and (c) represent reconstructions. (b) and (d) are originals.



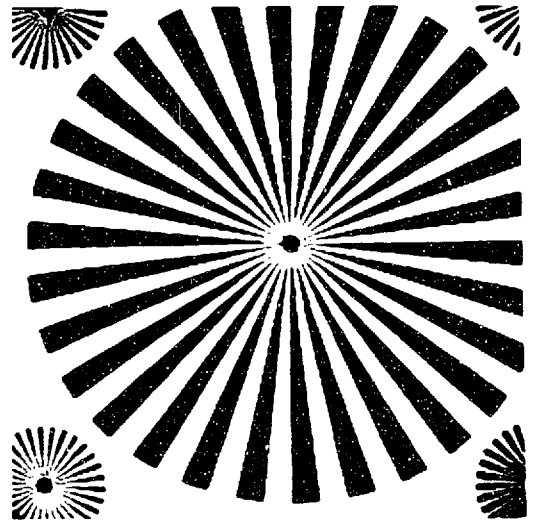
(a)



(b)



(c)



(d)

Figure 3.6

Reconstructions by interpolation in polar coordinates followed by linear interpolation. (a) and (c) represent reconstructions. (b) and (d) are originals.

this reconstruction technique. Mathematically the technique is not elegant, but it yields an algorithm which is straightforward to implement, the reconstructions from which are of good quality. Unlike the first two algorithms, this technique does not require that $f(x,y)$ be a function of finite order, although since it is necessary to sample both $f(x,y)$ and its projections, we shall assume that $f(x,y)$ is nearly bandlimited.

In section 2.3 of Chapter II it was shown that $f(x,y)$ could be expressed in terms of its samples by

$$\begin{aligned} f(x,y) &= \frac{1}{(2\pi)^2} \int_{-\infty}^{\infty} \int_0^{\pi} S_{\theta}(\omega) \exp[j(x\omega \cos\theta + y\omega \sin\theta)] |\omega| \, d\omega d\theta \\ &= \frac{1}{(2\pi)^2} \int_{-\infty}^{\infty} \int_0^{\pi} S(\theta,\omega) \exp[j(x\omega \cos\theta + y\omega \sin\theta)] |\omega| \, d\omega d\theta \end{aligned} \quad (3.34)$$

where $S_{\theta}(\omega)$ represents the slice of $F(\omega_x, \omega_y)$ at angle θ . The second equation of (3.34) simply rewrites $S_{\theta}(\omega)$ as $S(\theta,\omega)$ to emphasize the fact that $S_{\theta}(\omega)$ is a function of two variables. The ω - θ coordinate system is similar to the standard polar coordinate system except that ω may take on values from $-\infty$ to ∞ and the range of θ is constrained to 0 to π . This is so that along a line with a fixed value of θ , $S(\theta,\omega)$ corresponds to a slice of $F(\omega_x, \omega_y)$ at angle θ .

Assume that N slices are available and that they are at angles $\theta_0, \theta_1, \dots, \theta_{N-1}$. Further assume that along each slice the values of $S(\theta_i, \omega)$ are known at M values designated by $\omega_{-M/2+1}, \dots, \omega_0, \omega_1, \dots, \omega_{M/2}$. It shall be assumed that M is even although this is not necessary. (If M is odd then the indices on ω should go from $-\frac{M-1}{2}$ to $+\frac{M-1}{2}$). Furthermore

since the radial values will be computed from sampled projections using a DFT, we shall assume that the radial spacing is independent of both M and the set of slice angles. Thus

$$\Delta\omega = \omega_{m+1} - \omega_m \quad (3.35)$$

It is not necessary to assume that the slices are regularly spaced and this shall not be done, although this is presumably the case most frequently encountered in practice. Then we can define the angular spacing between projections by

$$\Delta\theta_i = \begin{cases} \frac{\theta_{i+1}}{2} - \frac{\theta_{i-1}}{2}, & i = 1, 2, \dots, N-2 \\ \frac{\theta_1}{2} - \frac{\theta_{N-1}}{2} + \frac{\pi}{2}, & i = 0 \\ \frac{\theta_0}{2} - \frac{\theta_{N-2}}{2} + \frac{\pi}{2}, & i = N-1 \end{cases} \quad (3.36)$$

It can be noted that $\sum_{i=0}^{N-1} \Delta\theta_i = \pi$, and that in the case of evenly spaced projections $\Delta\theta_i = \pi/N$.

Now suppose that the Fourier plane is divided into $N(M-1)$ small areas each of which is centered on one of the polar samples as illustrated in figure 3.7. For the moment we shall neglect the sample at the origin and the area of the section at $\omega = m\Delta\omega$, $\theta = \theta_i$ shall be denoted by ΔA_{mi} . If the spacing between adjacent polar samples is sufficiently small so

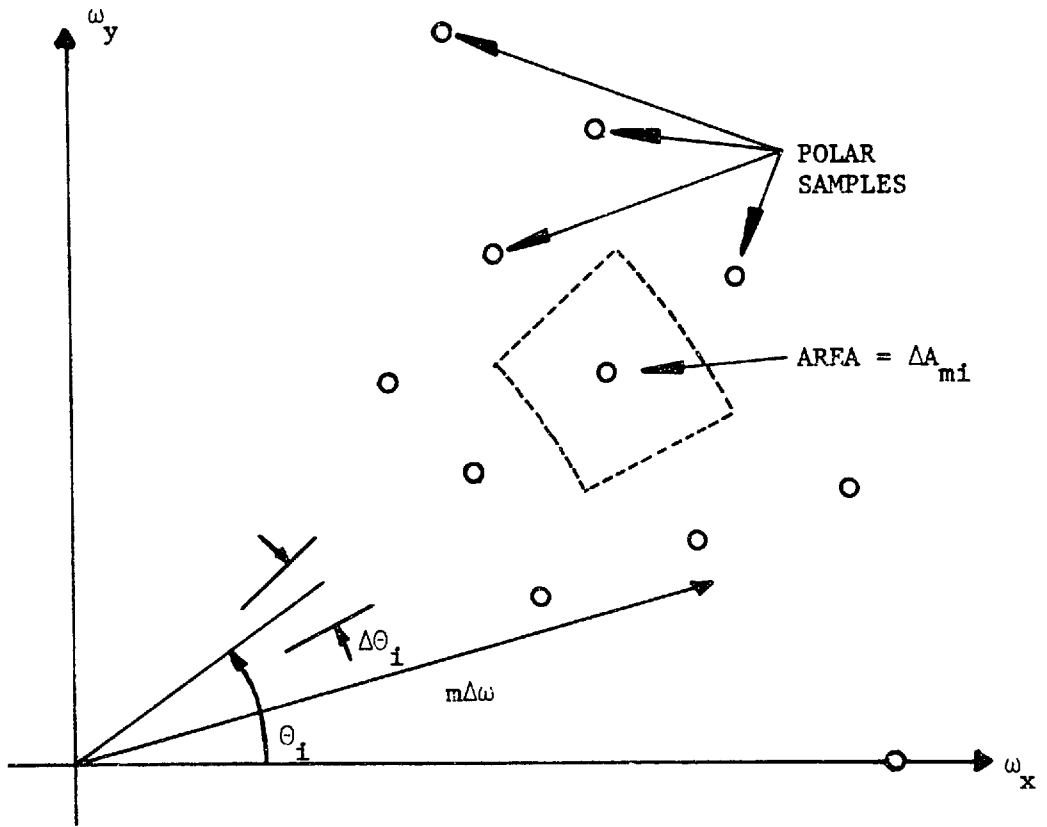


Figure 3.7

The area ΔA_{mi} associated with one polar sample.

that the quantity $S(\Theta, \omega) \exp[j\omega(x \cos\Theta + y \sin\Theta)]$ is nearly constant over each small area, then we can approximate (3.34) by

$$f(x, y) \approx \frac{1}{4\pi^2} \sum_{i=0}^{N-1} \sum_{m=-M/2+1}^{M/2} S(\Theta_i, m\Delta\omega) \exp[jm\Delta\omega(x \cos\Theta_i + y \sin\Theta_i)] \Delta A_{mi} \quad (3.37)$$

where if $m \neq 0$

$$\begin{aligned} \Delta A_{mi} &= \frac{\Delta\Theta_i}{\pi} \left| (m\Delta\omega + \frac{\Delta\omega}{2})^2 - (m\Delta\omega - \frac{\Delta\omega}{2})^2 \right| \\ &= \frac{2|m|}{\pi} \Delta\omega^2 \Delta\Theta_i \\ &= \frac{8|m|}{\pi} \cdot \frac{W^2}{M^2} \Delta\Theta_i \end{aligned} \quad (3.38)$$

The integral of a function which is continuous or nearly continuous (continuous except for a finite number of step discontinuities) can be closely approximated by a sum in this fashion. However, $F(\omega_x, \omega_y)$ generally has a delta function at $\omega_x = \omega_y = 0$ representing the DC level or mean gray level of the unknown picture. In the operations of processing projections - sampling, selecting only a finite number of samples and using a DFT - this DC level becomes associated with the central sample of the polar raster. Inasmuch as this sample is common to all lices it can be measured from any of them ^{*}. We will presumably want the

* In fact, the fact that all projections must have the same DC level is useful for preprocessing the projections. In the act of physically obtaining the projections e.g. illuminating the specimen, processing negatives, et., their DC levels might come out to be different. The invariance of the DC level from projection to projection allows us to normalize the projections before reconstructing from them.

DC levels of the original and of the reconstruction to agree. Thus we can combine equations (3.37) and (3.38) to get

$$f(x,y) \approx \hat{f}(x,y) = \frac{S(\theta_0, 0)}{4\pi^2} + \frac{2W^2}{\pi^2 M^2} \sum_{i=0}^{N-1} \Delta\theta_i \sum_{m=-M/2+1}^{M/2} |m| S(\theta_i, m\Delta\omega) \times \exp[jm\Delta\omega(x \cos\theta_i + y \sin\theta_i)] \quad (3.39)$$

Equation (3.39) represents a reconstruction algorithm since it expresses $f(x,y)$ in terms of $\{S(\theta_i, m\Delta\omega)\}$, the slice samples. The direct computation of (3.39) is formidable as that equation is written, however, we can reinterpret it and use the DFT to make it easier to compute. Reinterpreting (3.39) has multiple advantages. It gives us a straightforward computational procedure for implementing the algorithm, provides us with some insight into how the algorithm works, and shows us that this algorithm is equivalent to another algorithm - the smearing algorithm which can be implemented in the space domain. With the smearing algorithm each projection is back projected or smeared in the direction of the original projection and the smeared projections are then weighted and summed. Let us define what is meant by smearing. If $p_{\theta_i}(u_i)$ represents the projection of $f(x,y)$ at angle θ_i where

$$\begin{aligned} u_i &= x \cos\theta_i + y \sin\theta_i \\ v_i &= -x \sin\theta_i + y \cos\theta_i \end{aligned} \quad (3.40)$$

then the smeared projection at angle θ_1 , $p_{\theta_1}(u_1, v_1)$ is defined by

$$p_{\theta_1}(u_1, v_1) = p_{\theta_1}(u_1) \quad (3.41)$$

To express (3.39) in terms of smeared projections we can first rewrite (3.39) as

$$\hat{f}(x,y) = \frac{S(\theta_0, 0)}{4\pi^2} + \frac{2W^2}{\pi^2 M^2} \sum_{i=0}^{N-1} \Delta\theta_1 g_1(x,y) \quad (3.42)$$

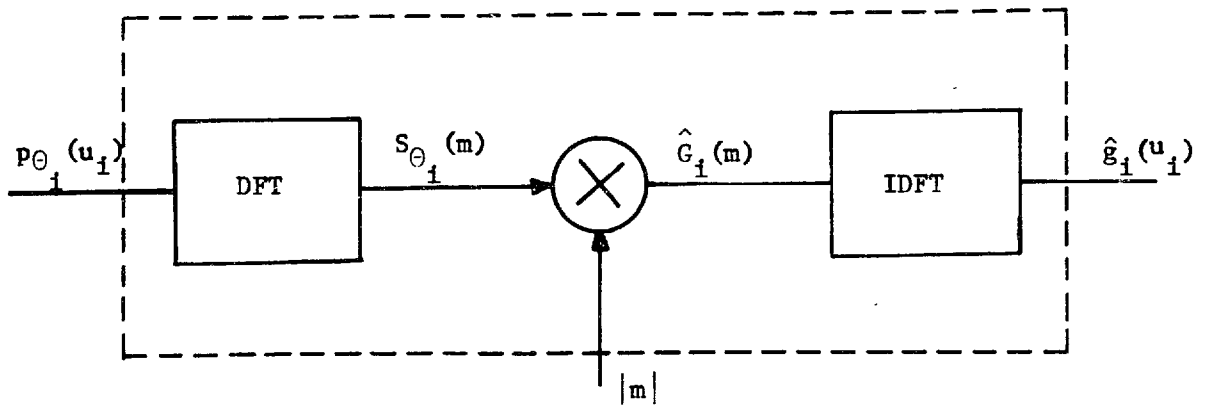
where

$$g_1(x,y) = \sum_{m=-M/2+1}^{M/2} |m| S(\theta_1, m\Delta\omega) \exp[jm\Delta\omega(x \cos\theta_1 + y \sin\theta_1)] \quad (3.43)$$

If we define $\hat{g}_1(u_1, v_1) = g_1(x,y)$ with a change of coordinates, then

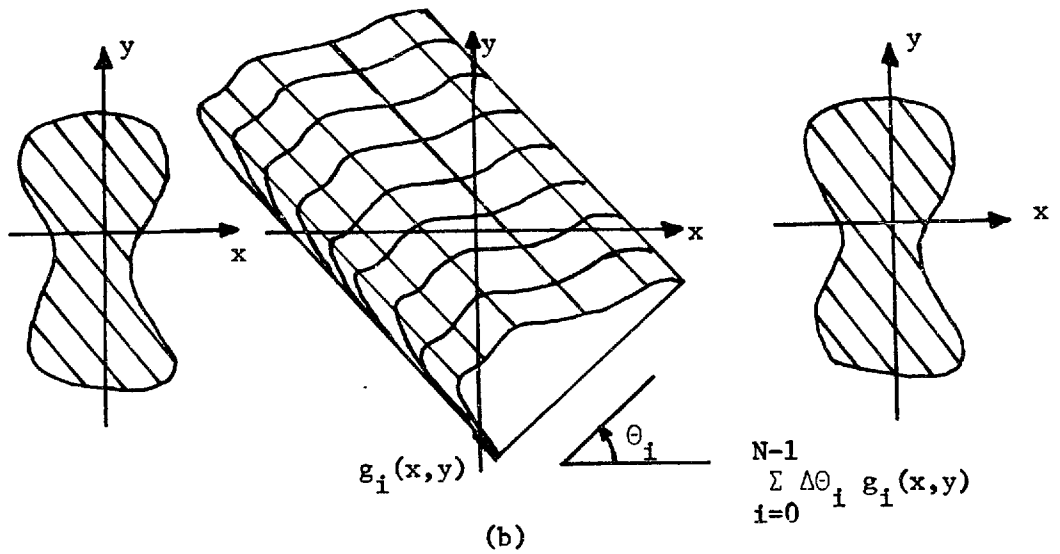
$$\hat{g}_1(u_1, v_1) = \sum_{m=-M/2+1}^{M/2} |m| S(\theta_1, m\Delta\omega) \exp[jmu_1\Delta\omega] \quad (3.44)$$

From (3.44) we see that $\hat{g}_1(u_1, v_1)$ is a function only of u_1 and that it is thus a smeared quantity. Furthermore the quantity which is smeared is a filtered projection. This filtering can be accomplished by taking the DFT of the projection, multiplying the resulting sequence by $|m|$ and then inverse transforming. According to (3.42), these filtered smeared projections $\{g_1(x,y)\}$ are then weighted, summed and added to the DC bias (constant) function. This procedure is illustrated in figure 3.8.



(a)

a flowchart of the computational operations involved



(b)

a pictorial representation of the algorithm

Figure 3.8

The smearing algorithm.

Instead of computing $\hat{g}_1(u_1)$ from $p_{\theta_1}(u_1)$ by taking transforms, we could confine ourselves totally to the space domain and express $\hat{g}_1(u_1)$ as a (circular) convolution of $p_{\theta_1}(u_1)$ and the inverse discrete Fourier transform of $|m|$. If we denote the latter function by $h(u_1)$, then

$$\begin{aligned}
 h(u_1) &= F^{-1}[|m|] = \sum_{m=-M/2+1}^{M/2} |m| \exp[jmu_1] \\
 &= \frac{\frac{M}{2} \sin(\frac{M-1}{2} u_1)}{2 \sin \frac{u_1}{2}} - \frac{1 - \cos \frac{M}{2} u_1}{4 \sin \frac{u_1}{2}} + \frac{M}{2} \exp[j\frac{M}{2}u_1]
 \end{aligned} \tag{3.44}$$

It should be stated, however, that the modification of the projections is more easily carried out in the frequency domain, than by performing the convolutions in the space domain.

This algorithm has been used by Vainshtein (51), Ramachandran(46), Herman (30), Bracewell (3) and perhaps others. There are a number of nice features to it. First it imposes no requirements on $f(x,y)$ except that it be nearly bandlimited and that $F(\omega_x, \omega_y)$ be "slowly varying" in ω_x and ω_y so that our original approximation of an integral by a sum is valid. These are not severe restrictions to impose. Another advantage of the algorithm is that the entire procedure can be implemented in the space domain (although as we have seen, it may be more efficient to filter the projections in the frequency domain). Omitting the modification of the projections, this system can in fact be implemented optically and such an optical system has been built by Garrison, Grant et al. (26)(27) (28). Another nice feature of this algorithm, which is actually the nicest feature of all, is that it yields very good reconstructions.

On the other hand there are a couple of problems inherent with the smearing algorithm. One of the most serious is that the reconstructions are very sensitive to inaccuracies in the input projections. Any errors or "noise" in the projections is amplified in the reconstructions and as a result the final reconstructions appear noisy, that is the reconstructions have a mottled or speckled appearance to them.

Some reconstructions formed by using this algorithm are shown in figure 3.9. As before, the reconstructions were made from 64, 256 point projections and the reconstructions are displayed as 256 x 256 pictures. The original pictures from which the projections were computed are included for comparison. It is perhaps instructive to compare these reconstructions with those in figure 3.4 obtained by linear interpolation. More fine details seem to be evident in the smearing reconstructions. For example the eyes, mouth, and collar area of the portrait are much more sharply defined with smearing. Also with the reconstruction of the test pattern the rays of the test pattern are clear with sharp edges unlike the interpolation reconstructions and the smaller patterns in the corners of the picture are resolved. On the negative side are the backgrounds of the smeared reconstructions which are not uniform and the speckled appearance of the reconstructions. The graininess can be removed somewhat at the expense of some of the sharp details in the reconstruction by low pass filtering the reconstructions. This low pass filter can be incorporated into the high frequency emphasis filter which operates on the projections prior to smearing them.

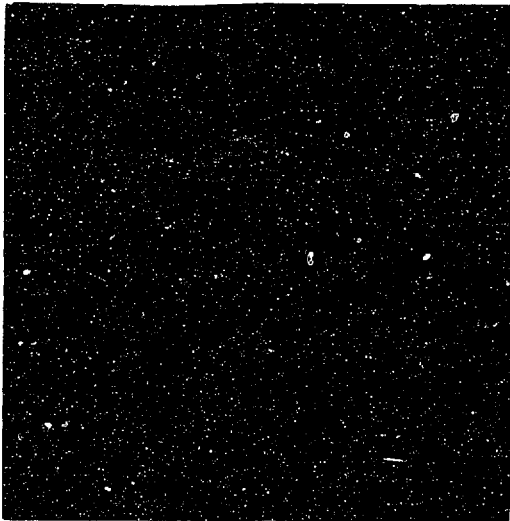
In figure 3.10 one of the pictures is reconstructed using 128, 64, 32, and 16 projections so that the degradation in performance can be



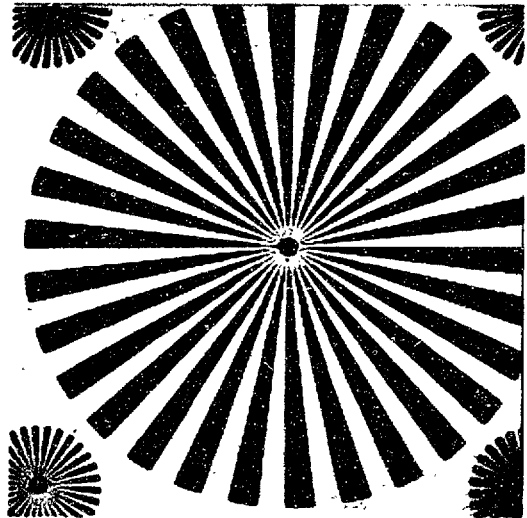
(a)



(b)



(c)



(d)

Figure 3.9

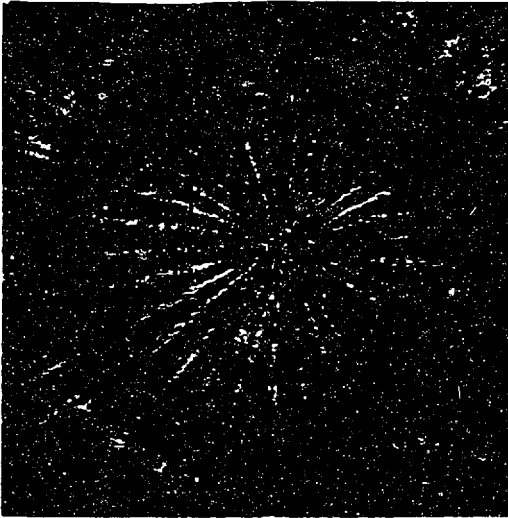
Reconstructions by smearing from 64 evenly spaced projections. (a) and (c) represent reconstructions. (b) and (d) are originals.



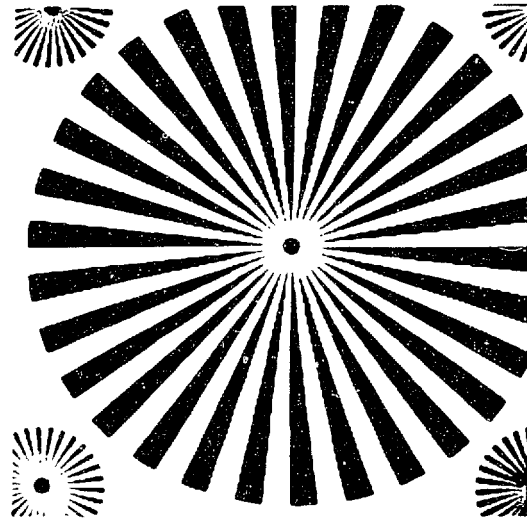
(a)



(b)



(c)



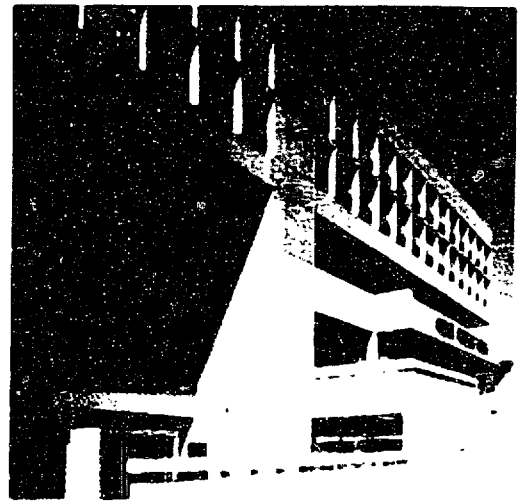
(d)

Figure 3.9

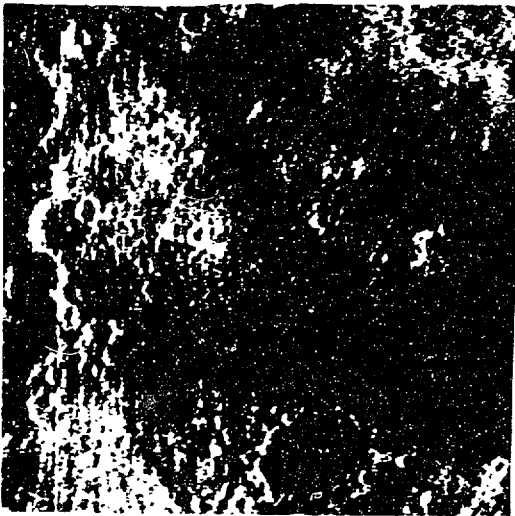
Reconstructions by smearing from 64 evenly spaced projections. (a) and (c) represent reconstructions. (b) and (d) are originals.



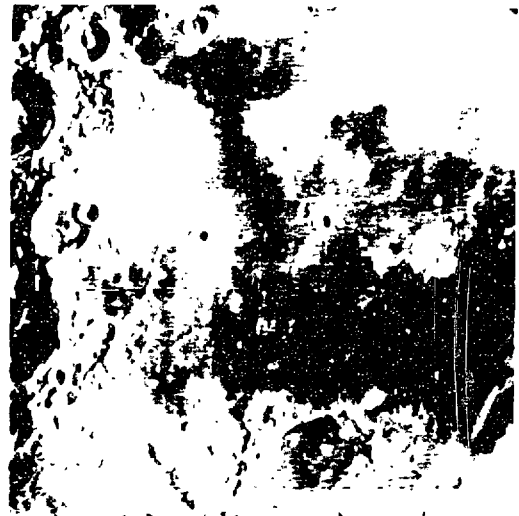
(e)



(f)



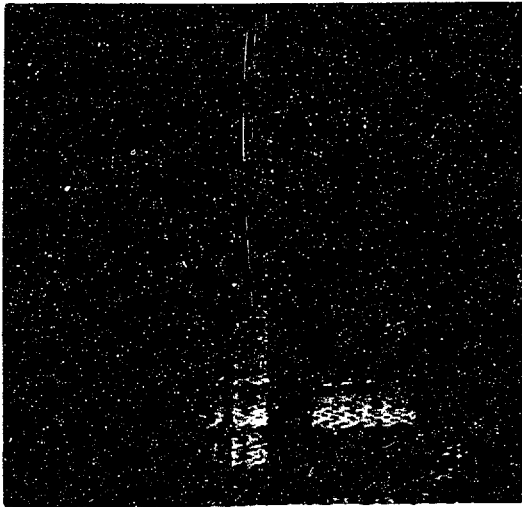
(g)



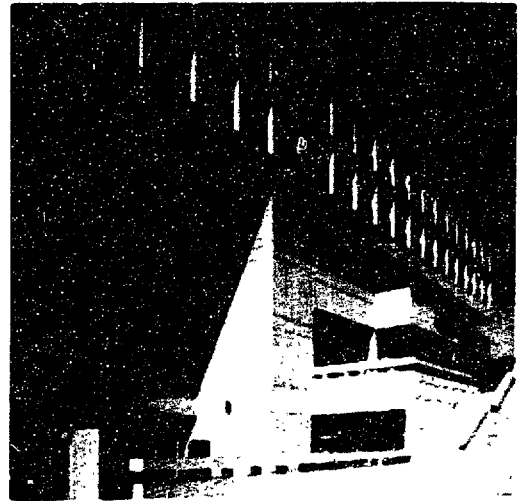
(h)

Figure 3.9 (cont'd)

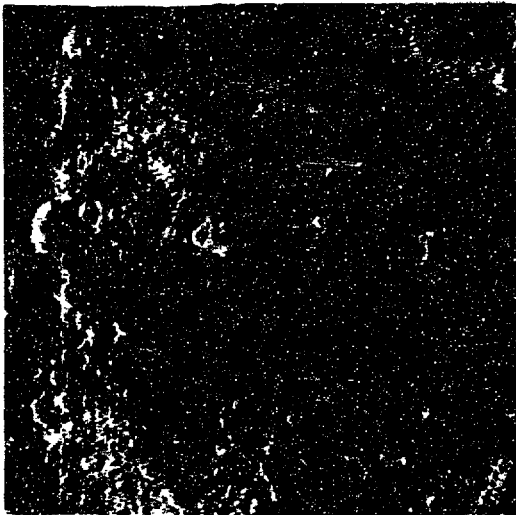
Reconstructions of two additional photographs by the smearing algorithm. (e) and (g) are reconstructions. (f) and (h) are originals.



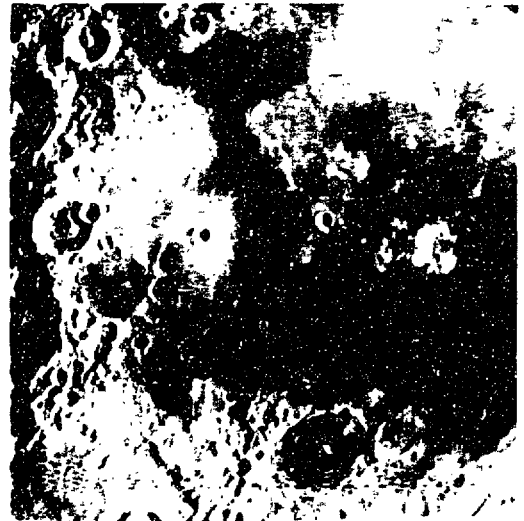
(e)



(f)



(g)



(h)

Figure 3.9 (cont'd)

Reconstructions of two additional photographs by the smearing algorithm. (e) and (g) are reconstructions. (f) and (h) are originals.



(a)



(b)



(c)



(d)

Figure 3.10

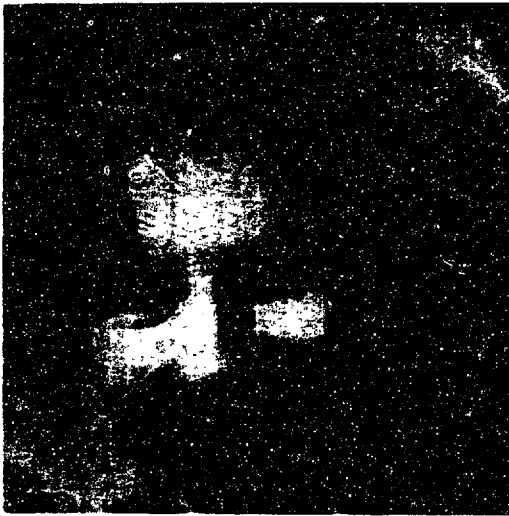
Reconstructions done by the smearing algorithm for different numbers of projections. (a) 128 projections (b) 64 projections (c) 32 projections (d) 16 projections.



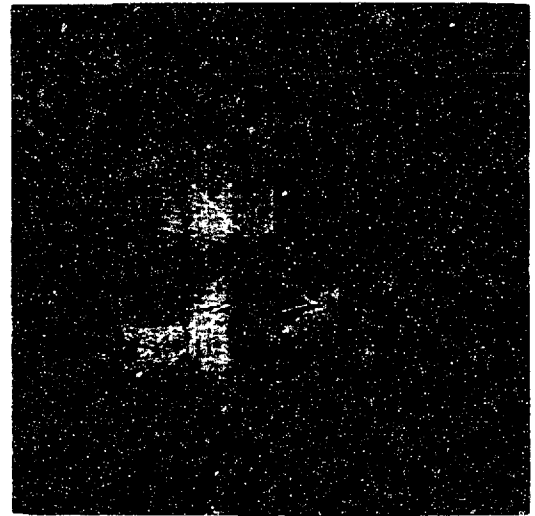
(a)



(b)



(c)



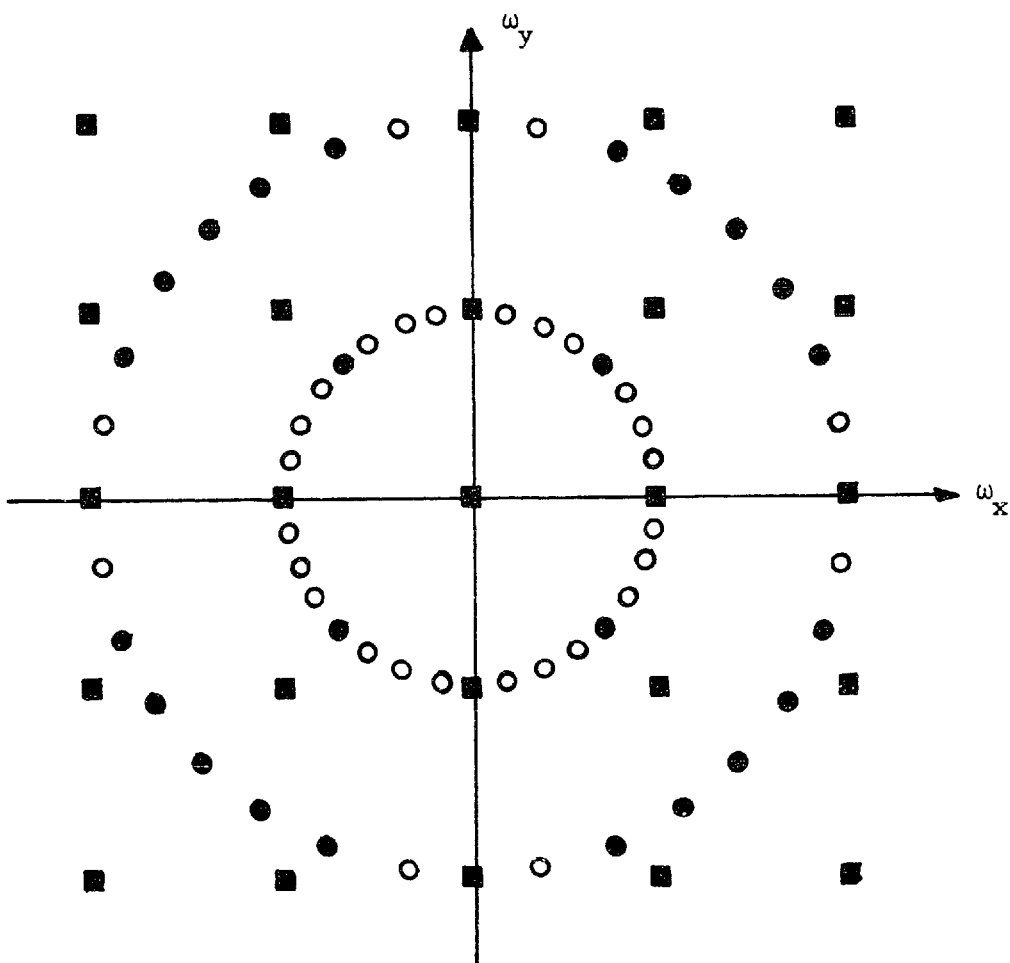
(d)

Figure 3.10

Reconstructions done by the smearing algorithm for different numbers of projections. (a) 128 projections (b) 64 projections (c) 32 projections (d) 16 projections.

seen when the number of projections is reduced. For the latter two reconstructions the irregularities caused by the smearing operation (evident as linear streaks) nearly obscure the face. These are caused by "noise" in the projections and are an important effect with the smearing algorithm when the number of projections is not large. When more projections are used this same noise causes the speckled appearance, which goes down as the number of projections is increased still further.

We notice in comparing the results of the four algorithms presented in this chapter that the smearing algorithm reconstructed details from the projections that the three interpolation algorithms could not extract. A closer examination of these algorithms reveals a possible explanation for this difference in performance. In the linear and zeroth-order interpolation algorithms the value of Cartesian samples was estimated from neighboring polar samples prior to performing an inverse DFT. As a result polar samples which are not close to Cartesian samples are ignored. For large values of ω (the radial variable in a polar coordinate system) this effect is negligible since almost all of these polar samples are used, but for polar samples close to the origin this effect becomes significant, especially since for photographs $|F(\omega_x, \omega_y)|$ is largest for those values of ω_x and ω_y near the origin. This effect is illustrated in figure 3.11. Here we see the center of the Cartesian and polar rasters for a reconstruction from 16 projections. The filled squares represent Cartesian samples and the unfilled circles represent polar samples that are not used by the linear interpolation algorithm. The filled circles represent polar samples which are used by the linear interpolation algorithm (the zeroth order interpolation scheme uses even fewer polar



- - CARTESIAN SAMPLES
- - POLAR SAMPLES USED BY LINEAR INTERPOLATION ALGORITHM
- - POLAR SAMPLES NOT USED BY LINEAR INTERPOLATION ALGORITHM
BUT USED BY SMEARING ALGORITHM

Figure 3.11

An enlarged view of the centers of the polar and Cartesian rasters illustrating the subset of polar samples that are considered by the linear and zeroth-order interpolation algorithms.

samples). Any information associated with the open circles is completely lost by linear interpolation. Thus if we have two polar rasters which have identical values on the filled points they will have identical reconstructions by linear interpolation no matter how much those rasters differ on the open samples. On the first ring 75% of the samples are ignored and when more projections are used the percentage of samples which are ignored increases. On the other hand the smearing algorithm uses all of the polar samples since all of the projections are treated identically. Thus for two rasters to give identical reconstructions using smearing, those rasters must be identical.

The algorithm which reconstructs by interpolation in polar coordinates in the Fourier plane, like the smearing algorithm uses all of the polar samples. It assumes, however, that the unknown can be expanded as

$$\hat{F}(\omega, \theta) \approx \sum_{m=-M/2+1}^{M/2} \sum_{n=-N/2+1}^{N/2} f_{mn} \exp[j(\frac{2\pi m\omega}{W} + n\theta)]$$

If this approximation is not a good one, then the reconstructions made according to it will of course not be good.

The noise which is introduced in the smearing reconstructions is due to the high frequency emphasis filter which is applied to the projections and it introduces computational errors which are similar to those introduced by numerical differentiation.

3.5 Reconstruction Using Hankel Transforms

For completeness we present an algorithm here which is similar to the interpolation in polar coordinates algorithm. This technique has not been used by the author but it has been used successfully by DeRosier and Klug (7) - (18) to reconstruct from electron micrographs.

Let $f(r, \phi)$ represent the picture function in polar coordinates and let $F(\omega, \theta)$ represent its Fourier transform. Then since $f(r, \phi)$ is necessarily a periodic function in ϕ with period 2π , we can express $f(r, \phi)$ in a Fourier series.

$$f(r, \phi) = \sum_{n=-\infty}^{\infty} f_n(r) \exp[jn\phi] \quad (3.45)$$

where

$$f_n(r) = \frac{1}{2\pi} \int_{-\pi}^{\pi} f(r, \phi) \exp[-jn\phi] d\phi \quad (3.46)$$

However, since $f(r, \phi)$ and $F(\omega, \theta)$ are a Fourier transform pair it is true that:

$$f(r, \phi) = \frac{1}{4\pi^2} \int_0^{\infty} \int_{-\pi}^{\pi} F(\omega, \theta) \exp[jr\omega \cos(\phi - \theta)] \omega d\theta d\omega \quad (3.47)$$

Thus

$$f_n(r) = \frac{1}{2\pi} \int_{-\pi}^{\pi} \left\{ \frac{1}{4\pi^2} \int_{-\pi}^{\pi} \int_0^{\infty} F(\omega, \theta) \exp[jr\omega \cos(\theta - \phi)] \omega d\omega d\theta \right\} \exp[-jn\phi] d\phi \quad (3.48)$$

Interchanging the order of the integrations

$$f_n(r) = \frac{1}{8\pi^3} \int_0^\infty \int_{-\pi}^\pi F(\omega, \theta) \omega d\omega d\theta \int_{-\pi}^\pi \exp[j(r\omega \cos(\phi - \theta) - n\phi)] d\phi \quad (3.49)$$

$$= \frac{1}{8\pi^3} \int_0^\infty \int_{-\pi}^\pi F(\omega, \theta) \exp[jn(\theta + \frac{\pi}{2})] \omega d\omega d\theta \int_{-\pi+\theta}^{\pi+\theta} \exp[jr\omega \sin\alpha - n\alpha] d\alpha \quad (3.50)$$

$$= \frac{1}{4\pi^2} \int_0^\infty \int_{-\pi}^\pi F(\omega, \theta) \exp[jn(\theta + \frac{\pi}{2})] J_n(r\omega) d\theta d\omega \quad (3.51)$$

where $J_n(x)$ is the n^{th} order Bessel function of the first kind. Since $F(\omega, \theta)$ is a periodic function in θ with period 2π we can express it in a Fourier series as well.

$$F(\omega, \theta) = \sum_{n=-\infty}^{\infty} F_n(\omega) \exp[-jn(\theta + \frac{\pi}{2})] d\theta \quad (3.52)$$

The factor of $\frac{\pi}{2}$ has been included in the exponent of (3.52) so that by comparing equations (3.52) and (3.51) we can see that

$$f_n(r) = \frac{1}{2\pi} \int_0^\infty F_n(\omega) J_n(r\omega) d\omega \quad (3.53)$$

and

$$F_n(\omega) = \int_0^\infty f_n(r) J_n(r\omega) dr \quad (3.54)$$

Equations (3.53) and (3.54) say that $f_n(r)$ and $F_n(\omega)$ form a Fourier-Bessel or Hankel transform pair.

From this derivation we can formulate a reconstruction algorithm. From the slices we compute the sequences $F_n(\omega)$. If the slice angles are evenly spaced, this can be done using a DFT. Then we can take the n^{th} order Hankel transform of each of the $F_n(\omega)$ to obtain the $f_n(r)$. Then using another DFT calculation, $f(r, \phi)$ can be obtained on any desired number of radii.

The major difficulties with this technique are computational. Each of the Hankel transforms which must be taken is different since each uses a different Bessel function. This makes the amount of computation formidable. For helical structures or structures with some circular symmetry, only a few of these transforms need to be calculated and in these cases it represents an efficient technique. DeRosier and Klug in their original work reconstructed helices for which a reconstruction could be obtained from only one $f_n(r)$. As a result they needed only a single projection.

3.6 Considerations in Implementing Any Reconstruction Algorithm

There are a number of computational issues that arise in performing reconstructions. Some of these are discussed in this section.

3.6.1 Computation of Projections

Most of the examples which are presented in this dissertation are reconstructions of photographs made from one-dimensional projections.

These projections were computed from the original photographs which are included next to the reconstructions. They were computed rather simply.

The picture is first represented as a square array of samples of N^2 points. For all of the examples in this dissertation $N = 256$. Each sample of the picture is then mapped to a point on the projection axis, as illustrated in figure 3.12. The projection axis is divided into some number M (in our case 256) of evenly spaced bins. In general each sample will map to a point which is between the centers of two adjacent bins and the value that is associated with that picture sample is then apportioned between the two bins according to the relative distances between the centers of the bins and the point on the projection axis to which that sample was mapped. From the M bin values, we get an M point sequence which represents a digitized projection. It can then be Fourier transformed using a DFT to yield samples of a slice. This procedure is then repeated for all of the projections.

The above procedure, of course, only represents an approximation to the true projection function, however, the true projection is difficult to compute. We can derive an expression for the true projection at angle θ , subject to the constraint that $f(x,y)$, the unknown function is bandlimited within a square in the Fourier plane of half-side W .

From the sampling theorem $f(x,y)$ can be written as:

$$f(x,y) = \sum_{m=-\infty}^{\infty} \sum_{n=-\infty}^{\infty} f\left(\frac{m\pi}{W}, \frac{n\pi}{W}\right) \frac{\sin\frac{W}{\pi}\left(x - \frac{m\pi}{W}\right) \sin\frac{W}{\pi}\left(y - \frac{n\pi}{W}\right)}{\frac{W^2}{\pi} \left(x - \frac{m\pi}{W}\right) \left(y - \frac{n\pi}{W}\right)} \quad (3.55)$$

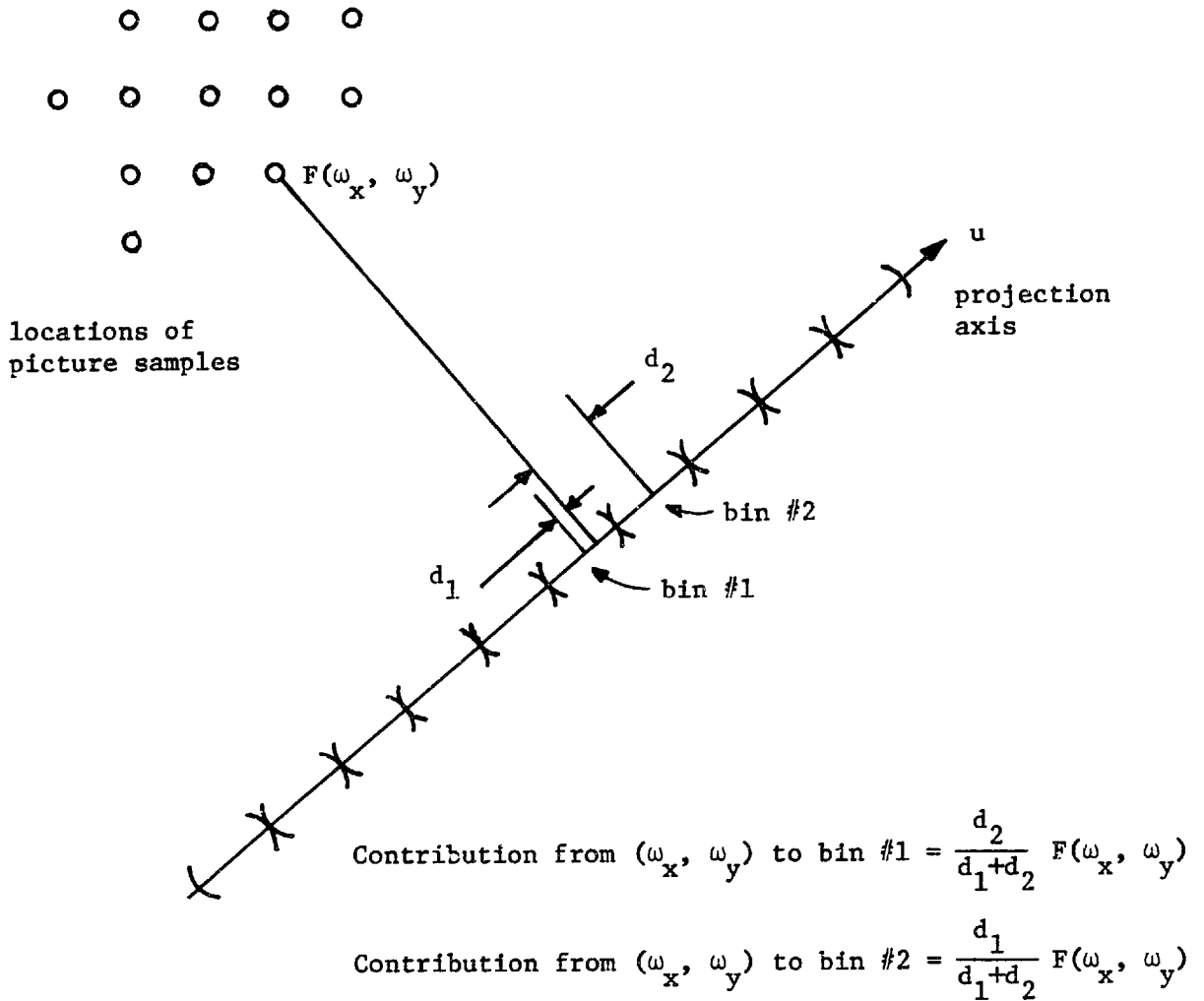


Figure 3.12

The algorithm used for computing projections.

from which it is seen that

$$F(\omega_x, \omega_y) = \frac{\pi^2}{W^2} \sum_{m=-\infty}^{\infty} \sum_{n=-\infty}^{\infty} f\left(\frac{m\pi}{W}, \frac{n\pi}{W}\right) \exp[-j \frac{\pi}{W}(m\omega_x + n\omega_y)] b_{WW}(\omega_x, \omega_y) \quad (3.56)$$

where

$$b_{WW}(\omega_x, \omega_y) = \begin{cases} 1 & |\omega_x| \leq W, |\omega_y| \leq W \\ 0 & \text{otherwise} \end{cases}$$

Thus the slice at angle θ , $S_\theta(\omega) = F(\omega \cos\theta, \omega \sin\theta)$ is

$$S_\theta(\omega) = \frac{\pi^2}{W^2} \sum_{m=-\infty}^{\infty} \sum_{n=-\infty}^{\infty} f\left(\frac{m\pi}{W}, \frac{n\pi}{W}\right) \exp[-j \frac{\pi\omega}{W}(m \cos\theta + n \sin\theta)] b_{WW}(\omega \cos\theta, \omega \sin\theta) \quad (3.57)$$

and $p_\theta(u)$ (continuous) is simply the inverse Fourier transform of $S_\theta(\omega)$.

$$p_\theta(u) = \frac{1}{2\pi} \int_{-\infty}^{\infty} S_\theta(\omega) \exp[ju\omega] d\omega \quad (3.58)$$

$$= \frac{\pi}{2W^2} \int_{-W_\theta}^{W_\theta} \sum_{m=-\infty}^{\infty} \sum_{n=-\infty}^{\infty} f\left(\frac{m\pi}{W}, \frac{n\pi}{W}\right) \exp[-j\omega\left(\frac{\pi}{W}(m \cos\theta + n \sin\theta) - u\right)] d\omega \quad (3.59)$$

$$= \frac{\pi}{2W^2} \sum_{m=-\infty}^{\infty} \sum_{n=-\infty}^{\infty} f\left(\frac{m\pi}{W}, \frac{n\pi}{W}\right) \int_{-W_\theta}^{W_\theta} \exp[-j\omega\left(\frac{\pi}{W}(m \cos\theta + n \sin\theta) - u\right)] d\omega \quad (3.60)$$

where

$$W_{\theta} = W/\max\{|\cos\theta|, |\sin\theta|\}$$

$$p_{\theta}(u) = \frac{\pi}{2W^2} \sum_{m=-\infty}^{\infty} \sum_{n=-\infty}^{\infty} f\left(\frac{m\pi}{W}, \frac{n\pi}{W}\right) \frac{\sin[W_{\theta}\left(\frac{\pi}{W}(m \cos\theta + n \sin\theta) - u\right)]}{\frac{\pi}{W}(m \cos\theta + n \sin\theta) - u} \quad (3.61)$$

$$p_{\theta}(u) = \frac{1}{2W} \sum_{m=-\infty}^{\infty} \sum_{n=-\infty}^{\infty} f\left(\frac{m\pi}{W}, \frac{n\pi}{W}\right) \frac{\sin[W_{\theta}\left(\frac{\pi}{W}(m \cos\theta + n \sin\theta) - u\right)]}{m \cos\theta + n \sin\theta - \frac{W}{\pi} u} \quad (3.62)$$

Equation (3.62) represents an equation for computing the projection from samples of the unknown. The actual procedure which was used to compute projections simply represents an approximation to it.

3.6.2 Aliasing and Transforming

If one wishes to have N evenly spaced samples of the Fourier transform of a one-dimensional bandlimited function of order M there are several methods for computing these samples depending on the relative sizes of M and N . If $M = N$ then we simply perform a discrete Fourier transform on the sequence of samples of the function taken at the Nyquist rate. If $M < N$ then we can append $N - M$ samples with zero value to the sequence, thus making it an N point sequence and then perform a DFT. If $M > N$ then we want to perform the sum

$$F(k) = \sum_{n=0}^{N-1} f(n) \exp[-j \frac{2\pi kn}{N}] \quad , \quad k = 0, 1, \dots, N-1 \quad (3.63)$$

$$F(k) = \sum_{i=0}^{L-1} \sum_{n=0}^{N-1} f(iN + n) \exp[-j \frac{2\pi k}{N}(iN + n)] , k = 0, 1, \dots, N-1 \quad (3.64)$$

for some integer L. It is assumed that the sequence is padded with sufficient zeros so that $M = LN$ is a multiple of N . Thus

$$F(k) = \sum_{n=0}^{N-1} \exp[-j \frac{2\pi}{N} nk] \sum_{i=0}^{L-1} f(iN + n) \quad k = 0, 1, \dots, N-1 \quad (3.65)$$

From (3.65) we observe that $F(k)$ corresponds to the N point DFT of the N point sequence

$$\hat{f}(n) = \sum_{i=0}^{L-1} f(iN + n)$$

The process of obtaining $\hat{f}(n)$ from $f(n)$ we refer to as aliasing.

3.6.3 Origin Centering

If we are going to reconstruct a picture $f(x,y)$, we can choose the origin of our coordinate system to be anywhere - the center of the picture, one of the corners or some other point. Once chosen, of course, we must abide by that decision for the choice of origin marks the pivot point for computing each projection and it also marks the origin of each projection. Suppose that we have two picture functions $f(x,y)$ and $g(x,y) = f(x - x_0, y - y_0)$. Then $G(\omega_x, \omega_y) = \exp[j(x_0 \omega_x + y_0 \omega_y)] F(\omega_x, \omega_y)$. The Fourier transforms of the two shifted sequences are the same except for a linear phase term. This linear phase term multiplies $F(\omega_x, \omega_y)$ by a

complex sinusoid and thus for some choices of origin, i.e. some choices of x_0, y_0 , $G(\omega_x, \omega_y)$ can have noticeable ripples in it due to this multiplicative sinusoid. These oscillations can affect any algorithms which assume a slowly varying $F(\omega_x, \omega_y)$ such as linear interpolation or smearing adversely. For these algorithms then we want to choose our origin so that $F(\omega_x, \omega_y)$ is as smooth as possible. Under the assumption that what we are trying to reconstruct is in the center of the picture and thus that the center of the picture has a higher gray level than the background, the origin should be chosen to be at the center of the picture. In the case where we are reconstructing from real projections, we have no choice for the origin, we must use the point about which the unknown was pivoted, but this is often in the center of the unknown picture anyway.

3.6.4 Block Floating Point

All calculations were done in 18 bit block floating point arithmetic, representing a compromise between the dynamic range of floating point and the speed of a fixed point realization.

In this work computation speed has not been a goal and the author has made no particular effort to minimize it, although some time saving tricks have been used. Another area to which the author has not dedicated much effort is the area of displays. The examples presented in this dissertation are plotted as 64 non-equally spaced gray levels using a single intensity level on a cathode ray tube with time duration modulation. This was recorded with a time exposure made by a Polaroid camera.

Chapter IV

RECONSTRUCTION FROM A CONCENTRIC SQUARES RASTER

4.1 Introduction

In the algorithms of Chapter III we implicitly assumed that the picture functions being reconstructed were bandlimited when we assumed that the projections could be represented by their samples. This condition is guaranteed if the picture is a two-dimensional bandlimited function provided that the projections are sampled sufficiently often. We also implied bandlimitedness when we assumed that it was sufficient to reconstruct our unknown two-dimensional function at only a finite number of points from which, by means of the sampling theorem, the whole unknown could be specified. In this chapter we shall explicitly utilize a specific bandlimitedness assumption in the design of a number of algorithms, which, although similar to those of Chapter III, and in fact inspired by them, will be seen to yield improved reconstructions.

For the purposes of the remainder of this thesis, a function will be said to be bandlimited if its Fourier transform is non-zero only over a square of half-side W in the Fourier plane as illustrated in figure 4.1. For such a function, because of the projection/slice theorem, each projection is seen to be a bandlimited function whose bandwidth is a function of the projection angle, θ . Thus, if $p_{\theta}(u)$ represents the

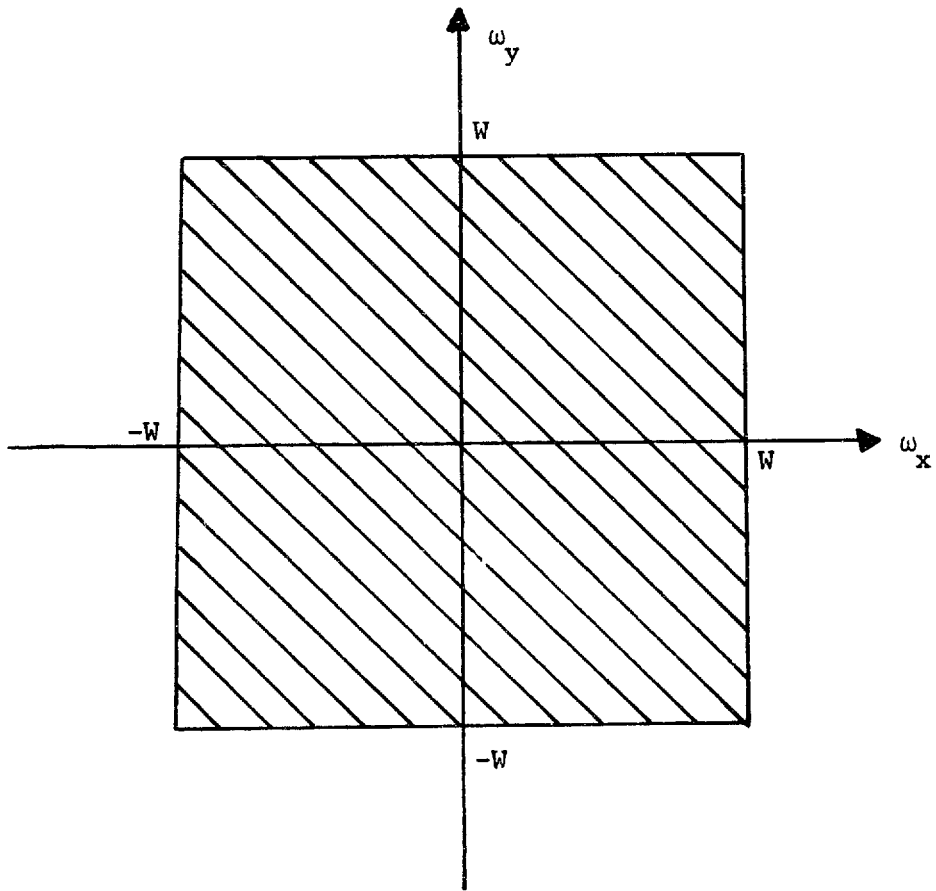


Figure 4.1

The region of the Fourier plane over which the transform of a bandlimited picture is non-zero.

projection at angle θ , we can reconstruct $p_\theta(u)$ from its samples as in equation (4.1).

$$p_\theta(u) = \sum_{n=-\infty}^{\infty} p_\theta\left(\frac{n\pi}{W_\theta}\right) \frac{\sin W\left(u - \frac{n\pi}{W_\theta}\right)}{\left(u - \frac{n\pi}{W_\theta}\right)} \quad (4.1)$$

where

$$W_\theta > \frac{W}{\max\{|\cos\theta|, |\sin\theta|\}} \quad (4.2)$$

The quantity on the right-hand side of equation (4.2) represents the bandwidth of the projection at angle θ .

In Chapter III, we chose our sampling rate by setting

$$W_\theta = \sqrt{2} W \quad (4.3)$$

for all values of θ . This choice of W_θ satisfies the condition of (4.2) and has the advantage that each projection is treated identically. When each projection is sampled with the sampling rate implied by (4.3) and the resulting sequences transformed using the DFT we obtain the familiar polar raster of samples of $F(\omega_x, \omega_y)$.

Choosing to sample all of the projections at the same rate is convenient but it is not the only approach that can be followed, nor is it necessarily the best approach. In fact, the fact that $F(\omega_x, \omega_y)$ is confined to a square in the Fourier plane suggests that perhaps a sampling scheme that yields Fourier samples on a square grid might be preferable to a scheme which yields its samples on a polar grid.

4.2 The Concentric Squares Raster

The right-hand side of equation 4.2 specifies the minimum sampling rate that can be used to sample the projection of a bandlimited function at angle Θ . If a lower sampling rate is used, information will be lost through the sampling process. Therefore suppose that the projection $p_{\Theta}(u)$ is sampled at a rate W_{Θ} where

$$W_{\Theta} = \frac{W}{\max\{|\cos\Theta|, |\sin\Theta|\}} \quad (4.4)$$

We see that the sampling rate can vary as a function of the projection angle. This is in contrast to the strategy of Chapter III where a single sampling rate was specified for all of the projections. In general these sequences of samples will be infinitely long, as they were in Chapter III. From these long sequences we can compute N samples of the slice $S_{\Theta}(\omega)$ by using a DFT to calculate the sum

$$S_{\Theta}(k\Delta\omega) = \sum_{n=-\infty}^{\infty} p_{\Theta}\left(\frac{n\pi}{W_{\Theta}}\right) \exp[-j \frac{2\pi}{N} nk] \quad , \quad k = -\frac{N}{2} + 1, \dots, 0, 1, \dots, \frac{N}{2} \quad (4.5)$$

The difference in the two sampling strategies results in different sets of slice samples being computed. In fact, we can in general control what samples of $S_{\Theta}(\omega)$ are computed by controlling the sampling interval used for the projection $p_{\Theta}(u)$.

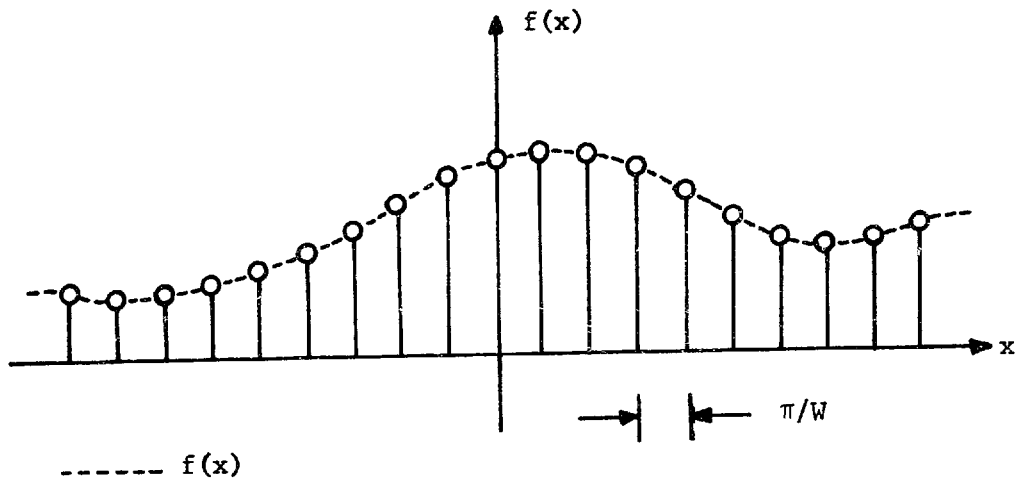
To see where the samples of $S_{\Theta}(\omega)$ lie in the two-dimensional Fourier plane, let us suppose that we take a one-dimensional bandlimited

function, sample it at its Nyquist rate and compute N values of its Fourier transform by an equation similar to 4.5. If we do this those N frequency samples are seen to be evenly spaced along the ω - axis and to extend over the entire non-zero frequency band as illustrated in figure 4.2. Similarly the samples of $S_{\Theta}(\omega)$ computed by equation 4.5 are evenly spaced and they extend over the entire band so that

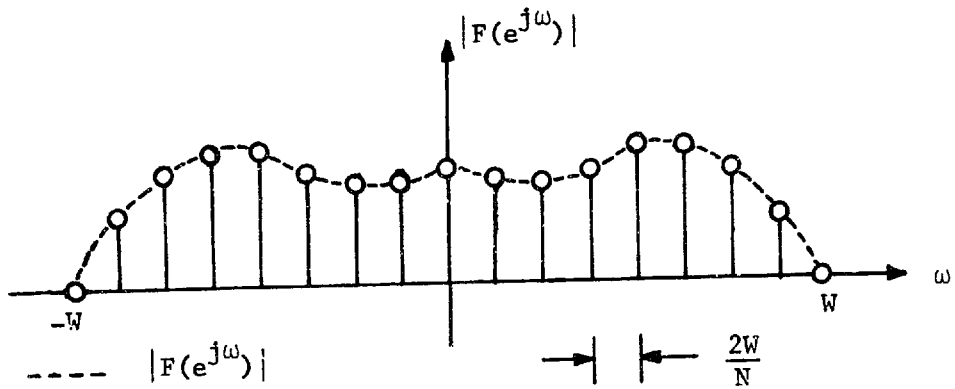
$$S_{\Theta}(k\Delta\omega) = F\left(\frac{2W_{\Theta}k}{N} \cos\Theta, \frac{2W_{\Theta}k}{N} \sin\Theta\right) \quad (4.6)$$

The radial spacing of the samples along each slice is seen to vary as a function of Θ , the angle of the slice. In Chapter III when the spacing of slice samples was not allowed to vary with Θ , we obtained a polar raster of samples; if the spacing of samples varies according to equation (4.6), we obtain a concentric squares raster of samples. A concentric squares raster is illustrated in figure 4.3. This name is motivated by the fact that if we set $k = \text{constant}$ in equation (4.6) and then allow Θ to vary continuously from 0 to 2π , the coordinates $\left(\frac{2W_{\Theta}k}{N} \cos\Theta, \frac{2W_{\Theta}k}{N} \sin\Theta\right)$ trace out a square contour which is concentric with the square region which defines the non-zero frequency components of $F(\omega_x, \omega_y)$.

One advantage of the concentric squares raster over the polar one is that it provides us with more frequency samples close to the origin where $|F(\omega_x, \omega_y)|$ takes on its largest values. This is due to the fact that $F(\omega_x, \omega_y)$ is by assumption bandlimited within a square rather than a circle. To illustrate this point consider the simplified case illustrated in figure 4.4. In this figure we have superimposed an 8 x 8 polar raster and an 8 x 8 concentric squares raster. The dashed square represents the



○ locations of samples of $f(x)$



○ samples which correspond to the DFT of $f(x)$

Figure 4.2

Relation between the Fourier transform of a band-limited function and the N point DFT of the sampled function when the sampling is performed at the Nyquist rate.

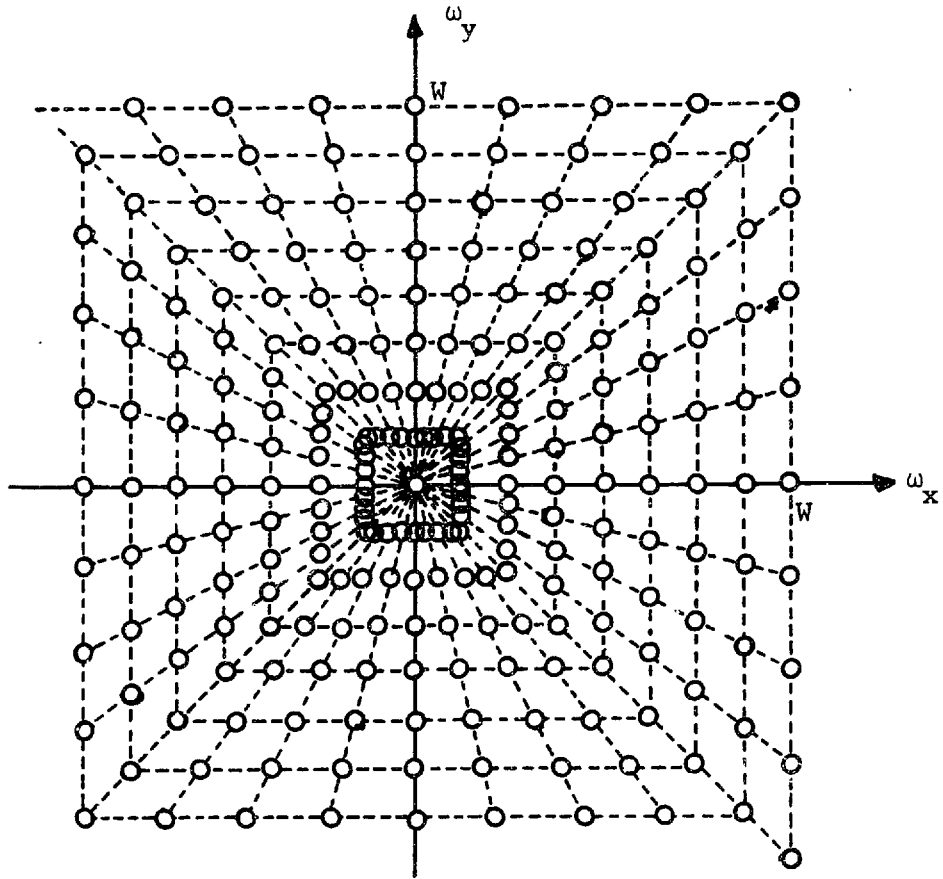


Figure 4.3

A concentric squares raster.

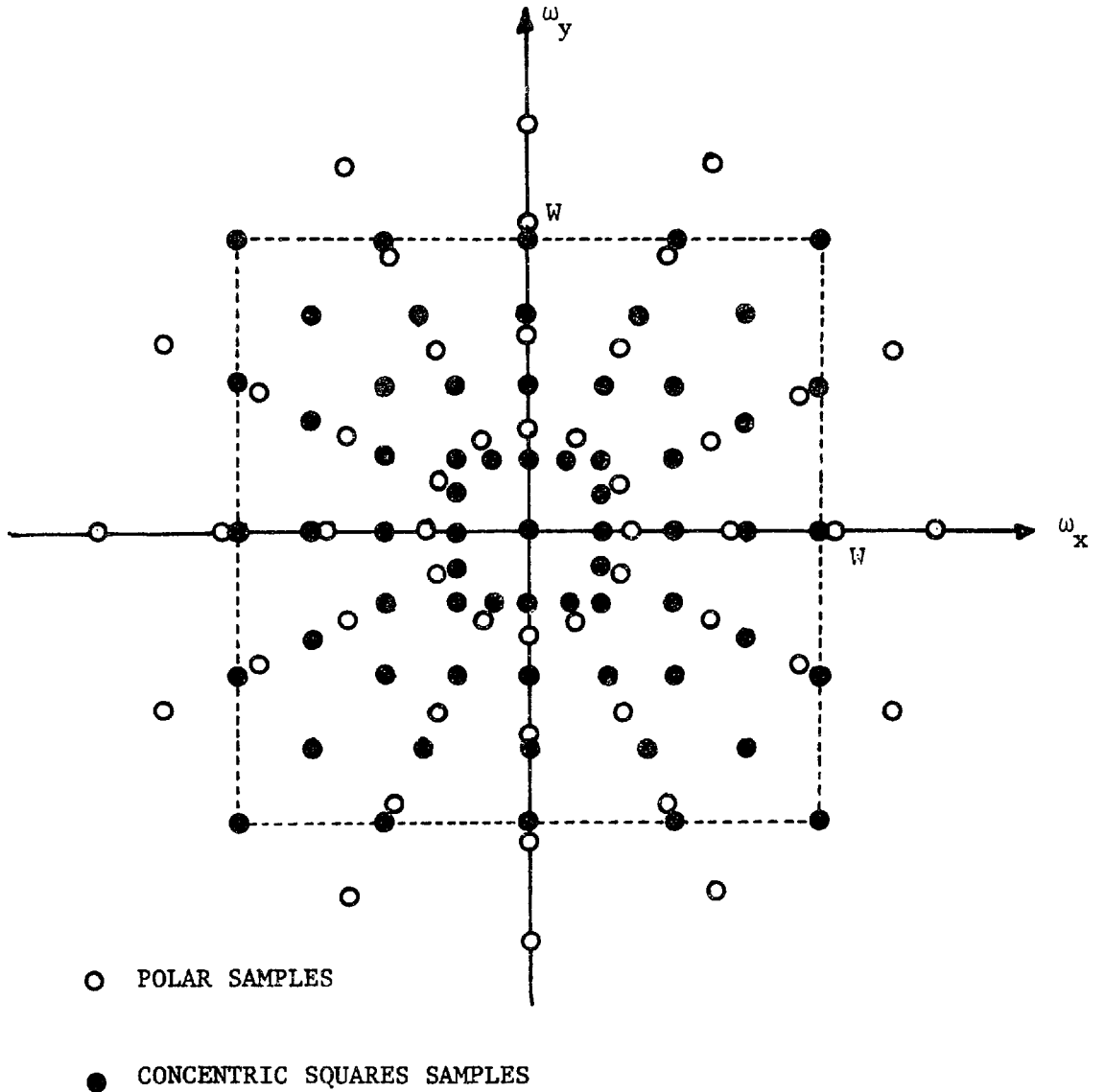


Figure 4.4

An 8 x 8 polar raster superimposed on an 8 x 8 concentric squares raster for comparing differences in resolution.

bandwidth of the unknown function. Each raster provides us with 57 distinct samples of $F(\omega_x, \omega_y)$. (Because of the redundancy at the central sample we do not get 64 distinct samples). It should be noted that more information is obtainable from the concentric squares samples than from the polar ones. Ten of the polar samples fall outside of the non-zero frequency band and thus contribute no information whatsoever. For larger rasters approximately 35% of the polar samples will fall outside this band. In contrast, none of the concentric squares samples lie outside the band.

Further relative advantages for the concentric squares raster can be ascertained in the special case when $f(x,y)$ is a function of finite order. Such a function can be expressed as

$$f(x,y) = \sum_{m=0}^{N-1} \sum_{n=0}^{N-1} f\left(\frac{m\pi}{W}, \frac{n\pi}{W}\right) \frac{\sin\frac{W}{\pi}\left(x - \frac{m\pi}{W}\right) \sin\frac{W}{\pi}\left(y - \frac{n\pi}{W}\right)}{\frac{W^2}{\pi^2}\left(x - \frac{m\pi}{W}\right)\left(y - \frac{n\pi}{W}\right)} \quad (4.7)$$

or

$$F(\omega_x, \omega_y) = \frac{\pi^2}{W^2} \sum_{m=0}^{N-1} \sum_{n=0}^{N-1} f\left(\frac{m\pi}{W}, \frac{n\pi}{W}\right) \exp[-j\frac{\pi}{W}(m\omega_x + n\omega_y)] b_{WW}(\omega_x, \omega_y) \quad (4.8)$$

where $b_{WW}(\omega_x, \omega_y)$ is the by now familiar indicator function which is zero outside the non-zero frequency band and one within it. We further recall from Chapter II that bandlimited functions of order N are completely specified by their $N \times N$ point DFT's. The DFT of $f(x,y)$ is

$$\hat{F}(k, \ell) \triangleq F(\omega_x, \omega_y) \Big|_{\substack{\omega_x = \frac{2W}{N} k \\ \omega_y = \frac{2W}{N} \ell}}, \quad 0 \leq k, \ell \leq N-1 \quad (4.9)$$

Thus the DFT corresponds to a set of samples of $F(\omega_x, \omega_y)$ which lie on a Cartesian raster, i.e. they lie on the intersections of an array of horizontal and vertical lines in the Fourier plane. The concentric squares samples are also seen to lie along horizontal and vertical lines in the Fourier plane. In fact the concentric squares samples lie along the same horizontal and vertical lines as the DFT. Thus if linear interpolation is used to estimate the DFT samples from the concentric squares samples we only need to interpolate along these horizontal and vertical lines and the interpolation is one-dimensional rather than two-dimensional as it was in the polar case. As a result we would expect better reconstructions from concentric squares linear interpolation than from polar linear interpolation.

As a comment it should be noted that if the projections are made by a source of collimated radiation such as an x-ray source then concentric squares samples can be obtained with a hardware scanner which does not have an adjustable sampling interval. This technique is illustrated in figure 4.5. Assume that the object which we wish to identify is irradiated by a collimated x-ray beam and that it lies between the beam source and a recording surface such as a photographic plate. Instead of rotating the unknown to produce different projections, assume that we rotate the x-ray source and the photographic plate simultaneously, while keeping the y-distance from the plate to the center of the unknown constant and maintaining the plate parallel to the x-axis of a hypothesized Cartesian coordinate system. When the projection angle exceeds 45° , the plate is rotated by 90° so that it now is parallel to the y-axis. Now as the projection angle is increased still further the plate is maintained at this orientation

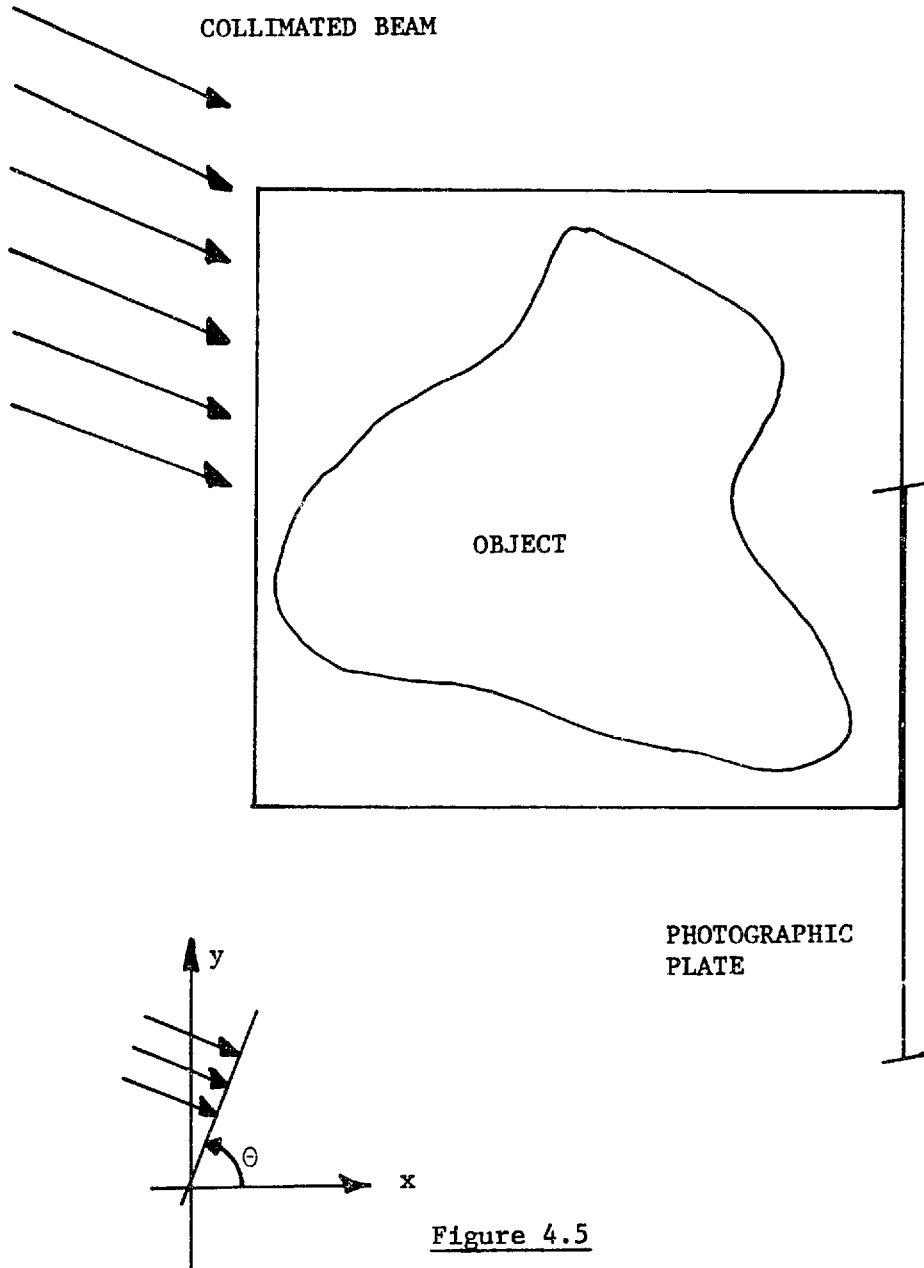


Figure 4.5

A configuration for recording concentric squares projections, such that all projections can be sampled without varying the sampling interval on a hardware scanner.

and moved around the unknown in such a fashion that the x-distance from the center of the object to the photographic plate is held constant. Once the projection angle reaches 135° , the plate is again rotated so that it is oriented parallel to the x-axis. Thus the photographic plate is moved in such a way that its center traces out a square. In this way the recorded picture is seen to be expanded by a factor of $\frac{1}{\max\{|\cos\theta|, |\sin\theta|\}}$ by the obliqueness of the recording surface. If all projections are now sampled with the same sampling interval, π/W , the resulting sequences correspond to a set of concentric squares sampled projections.

4.3 Bandlimited Functions of Finite Order

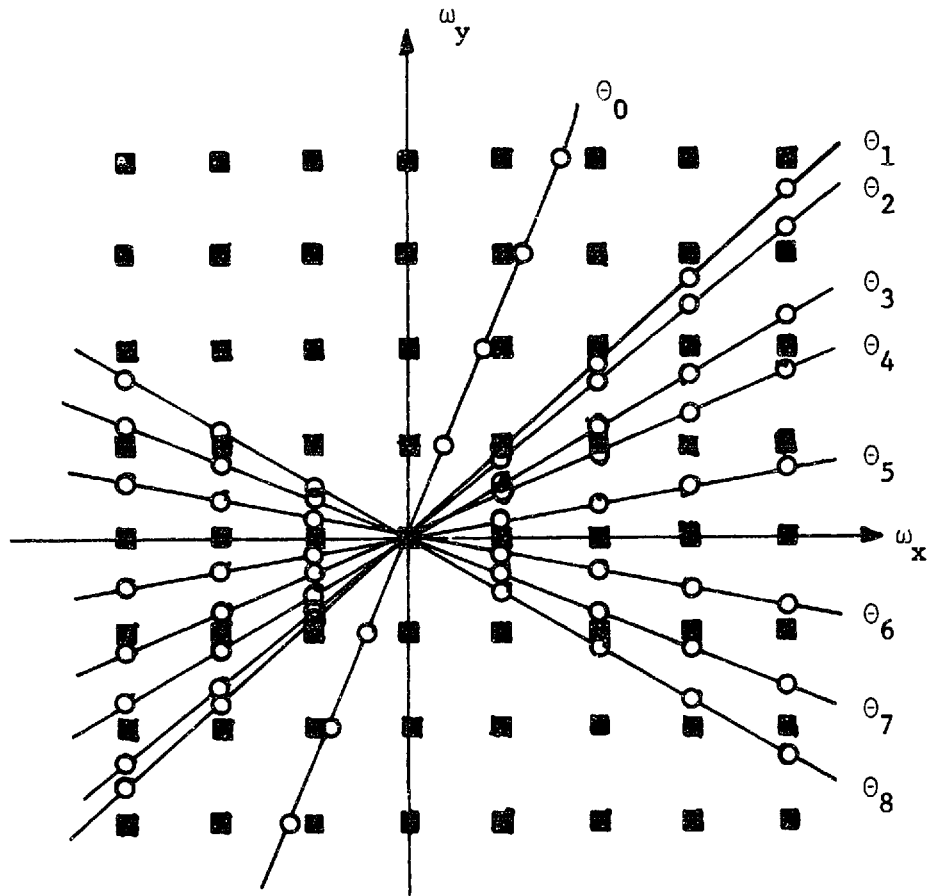
There exists a set of $N + 1$ concentric squares projections from which a bandlimited function of order N can be reconstructed exactly. In this section we shall outline a procedure for accomplishing this.

First it has been noted that bandlimited functions of finite order are completely specified by the DFT's of their non-zero samples (where the sampling is done at the Nyquist rate). Furthermore we note from equation (4.8) that the Fourier transforms of these functions are (over the passband) two-dimensional polynomials of degree $N - 1$ in each of the variables $\exp[-j\frac{\pi}{W}\omega_x]$ and $\exp[-j\frac{\pi}{W}\omega_y]$. Thus along those horizontal and vertical lines in the Fourier plane along which both the DFT samples and the concentric squares samples are defined, $F(\omega_x, \omega_y)$ varies as a one-dimensional polynomial of degree $N - 1$ in either $\exp[-j\frac{\pi}{W}\omega_x]$ or $\exp[-j\frac{\pi}{W}\omega_y]$. From a theorem of linear algebra we know that a one-dimensional polynomial of degree d is completely specified by any $d + 1$ independent sample values of that polynomial. (If a polynomial is

completely specified, an analytical expression for that polynomial can be written). Thus if we know the value of $F(\omega_x, \omega_y)$ at N distinct points on any horizontal or vertical line in the passband we can find $F(\omega_x, \omega_y)$ at any other point on that line. In particular if we can ascertain N different samples along any concentric square side, from the intersections of N slices, then any DFT samples which either lie on that side or on its extensions can be computed exactly. From this result we can show that a bandlimited function of order N can be reconstructed exactly from a particular set of $N + 1$ projections.

Assume that we wish to reconstruct an unknown and that we have the capability of obtaining projections at any angles which we desire. This being the case, let us require that N projections be taken at N distinct angles in the range $-45^\circ < \theta \leq 45^\circ$ and in addition we require one additional projection from outside this range. Ultimately we shall see that there are some restrictions on this last projection, but for the moment let its angle be anywhere in the range $45^\circ < \theta \leq 135^\circ$. We shall designate its angle by θ_0 . All $N + 1$ of these projections should be sampled and transformed so that the N point DFT's of these sequences lie on a concentric squares raster as is illustrated in figure 4.6 for the special case $N = 8$. At this point it should be noticed that we have specified the Fourier transform of $f(x, y)$ at $(N + 1)N - N = N^2$ distinct points and that our goal is to compute the N^2 non-zero picture samples.

Along each vertical side of the concentric squares we thus have N samples, one from each of the N slices in the range $-45^\circ < \theta \leq 45^\circ$. Since along each of these sides $F(\omega_x, \omega_y)$ varies as a complex one-dimensional polynomial of degree $N - 1$ in the variable $\exp[-j \frac{\pi}{W} \omega_y]$, we can



○ SAMPLES OBTAINED FROM PROJECTIONS

■ DFT SAMPLES

Figure 4.6

Set of Fourier plane samples from which an 8 x 8 picture can be reconstructed exactly, under the assumption that the picture is bandlimited and of order 8.

completely specify $F(\omega_x, \omega_y)$ along each of these vertical lines, except for the ω_y -axis (since the samples along this line are not distinct). Thus by means of a divided difference table or by Lagrange interpolating polynomials we can compute the value of $F(\omega_x, \omega_y)$ at all of those points that constitute the two-dimensional DFT except for the ones which lie along the ω_y -axis.

To fill in these remaining points we can use the extra projection at θ_0 . If $\theta_0 = 90^\circ$ then the remaining DFT samples are determined directly and we are done. If this last projection was taken at some other angle in the range $45^\circ < \theta \leq 135^\circ$, then consider the horizontal sides of the concentric squares raster. Along each of these sides we have a one-dimensional complex polynomial of degree $N - 1$ in the variable $\exp[-j \frac{\pi}{W} \omega_x]$. However, along each of these horizontal sides we also know N sample values, since along each line there are $N - 1$ DFT samples which have already been determined and one sample which is available from the last projection. (At this point we can observe that θ_0 must be chosen so that this last slice does not pass through any of the DFT samples already computed except for the one at the origin, otherwise we will not have N distinct sample values along each line. It is sufficient that the slope of this last slice be irrational). From the N values which we have along each line we can again use polynomial interpolation to determine those DFT samples along the ω_y -axis. Now the complete DFT of the picture is known. We can perform an inverse DFT to recover the N^2 non-zero picture samples and then apply the sampling theorem to obtain the complete picture.

This derivation, although useful for theoretical purposes does not necessarily lead to a useful reconstruction algorithm because of the

difficulty of performing the necessary interpolations, particularly on the inner columns of figure 4.6, where we must extrapolate values of a fairly high order polynomial from samples which are spaced closely together. This procedure is subject to large computational errors if the slice samples are not known exactly, which is invariably the case. An algorithm for performing the interpolation and inverse DFT simultaneously is derived in section 5.4, and the unavoidable computational errors which it introduces are estimated in the following section.

4.4 Approximate Reconstructions from a Concentric Squares Raster

Instead of trying to reconstruct $f(x,y)$ exactly as described in the preceding section because of the attendant computational problems with this approach let us consider some algorithms which will make an approximate reconstruction from a concentric squares raster. All three of the algorithms of Chapter III - linear interpolation, high order interpolation in polar coordinates, and smearing - can be adapted to perform reconstructions from concentric squares samples of $F(\omega_x, \omega_y)$. Let us therefore consider adapting each of these algorithms in turn.

4.4.1 Linear Interpolation

We can use linear interpolation to find the values of the $N \times N$ DFT of $f(x,y)$ from the concentric squares samples of $F(\omega_x, \omega_y)$. As we noted in section 4.2, this can be accomplished by interpolating in only one dimension because the DFT samples lie on the same horizontal and vertical lines as the concentric squares. If $f(x,y)$ is bandlimited and of

an order which is less than or equal to N then it is specified by its DFT. If it is not so well behaved but can be closely approximated by such a function, then hopefully the reconstruction obtained by this technique will closely approximate $f(x,y)$.

In figure 4.7 are some reconstructions made using linear interpolation from 64 projections, evenly spaced in angle from 0° to 180° . Each projection was obtained by a technique similar to the one used in Chapter III except that the width of the bins used to compute the projections were expanded by a factor of

$$\frac{1}{\max\{|\cos\theta|, |\sin\theta|\}}$$

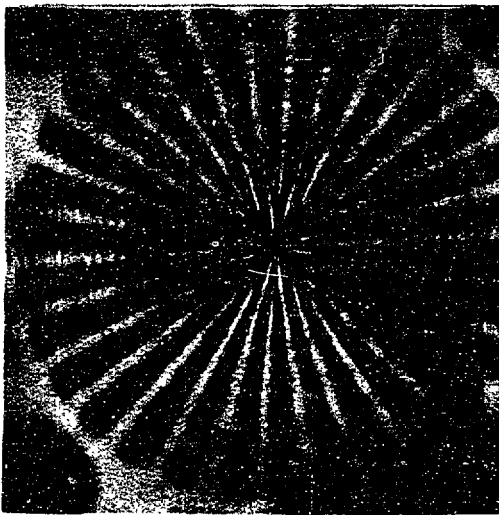
where θ represents the angle of the projection. In figure 4.8 we have used the same algorithm with a different set of projection angles. Instead of choosing the angles to be evenly spaced we have chosen them so that the intersections of the slices with the concentric squares are evenly spaced on each square. This set of projections yields a computationally simpler algorithm and it results in a higher density of samples in the "corners" of the non-zero region of $F(\omega_x, \omega_y)$. In figure 4.9 we have taken the latter set of projection angles and examined reconstructions made with 16, 32, 64, and 128 projections to see what improvement in reconstruction quality could be gained by adding more projections. In figure 4.10 we compare reconstructions made from 64 polar projection/slices and 64 concentric squares projection/slices. In all other details the two algorithms were identical.



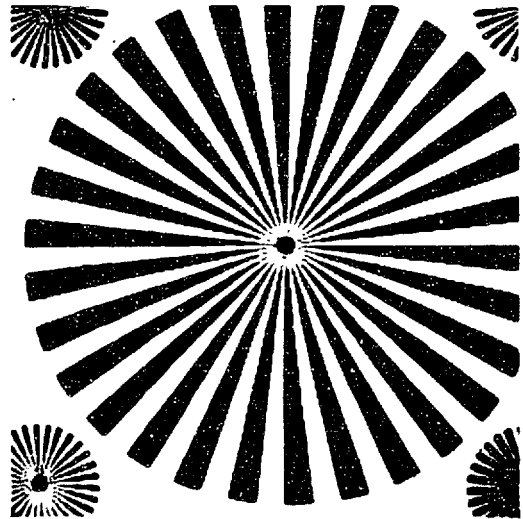
(a)



(b)



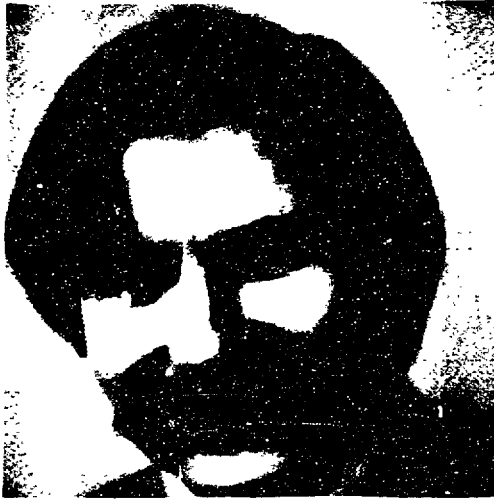
(c)



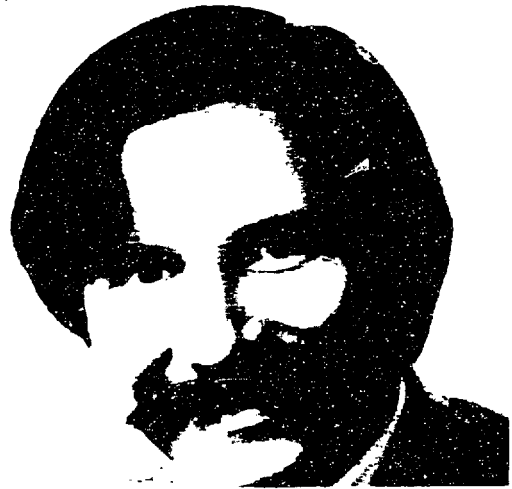
(d)

Figure 4.7

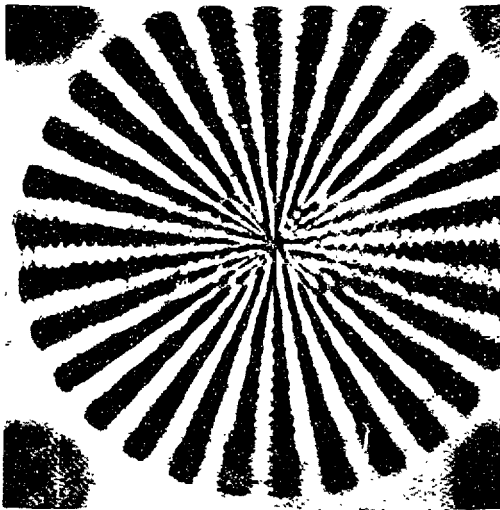
Reconstructions obtained by using linear interpolation on a concentric squares raster with 64 evenly spaced projections. Parts (a) and (c) correspond to reconstructions and parts (b) and (d) correspond to originals.



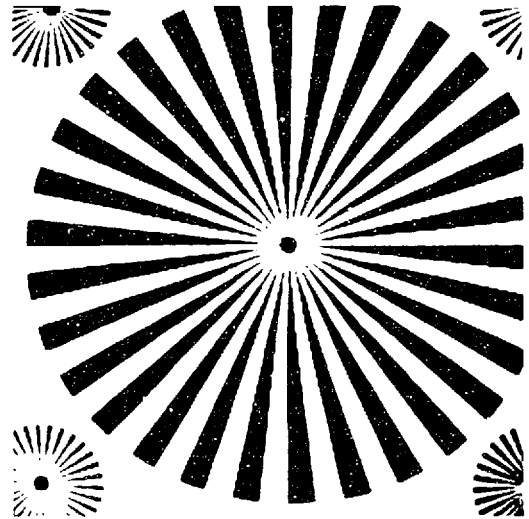
(a)



(b)



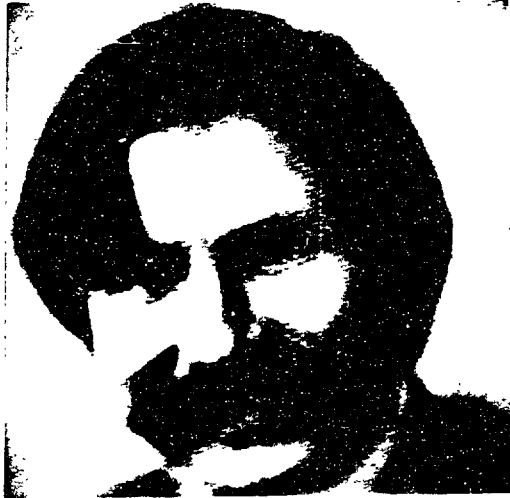
(c)



(d)

Figure 4.7

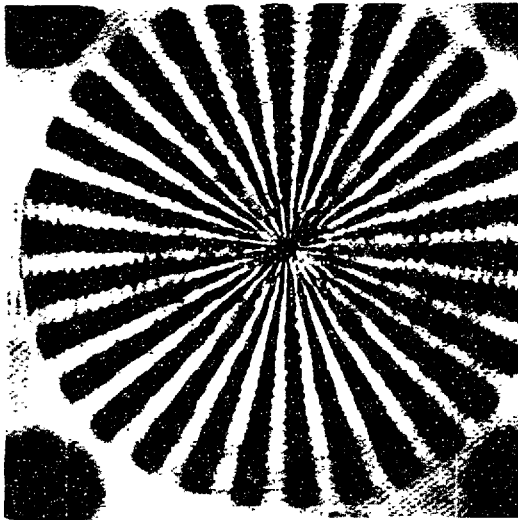
Reconstructions obtained by using linear interpolation on a concentric squares raster with 64 evenly spaced projections. Parts (a) and (c) correspond to reconstructions and parts (b) and (d) correspond to originals.



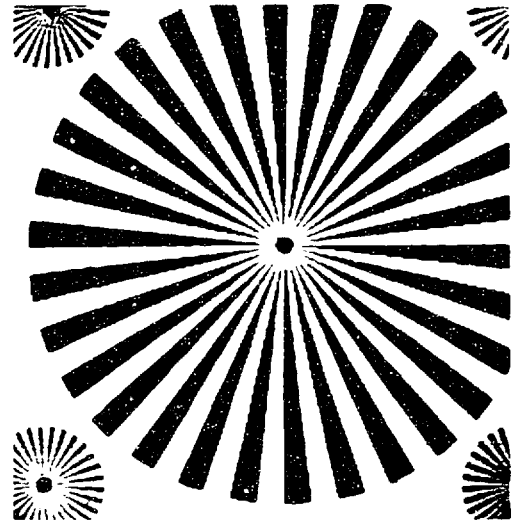
(a)



(b)



(c)



(d)

Figure 4.8

Reconstructions obtained using linear interpolation on a concentric squares raster from 64 projections which have evenly spaced intersections with the sides of the concentric squares. (a) and (c) correspond to reconstructions. (b) and (d) are originals.



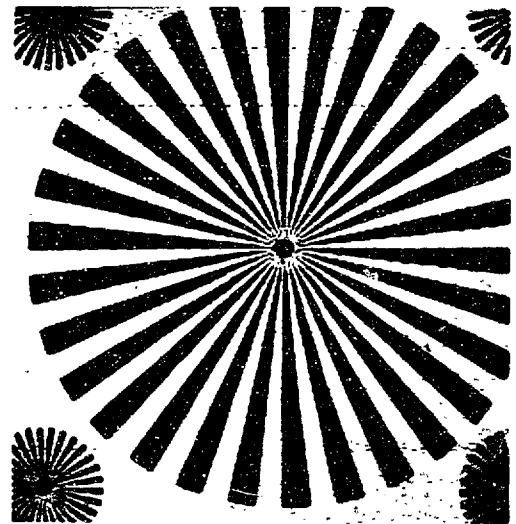
(a)



(b)



(c)



(d)

Figure 4.8

Reconstructions obtained using linear interpolation on a concentric squares raster from 64 projections which have evenly spaced intersections with the sides of the concentric squares. (a) and (c) correspond to reconstructions. (b) and (d) are originals.



(a)



(b)



(c)



(d)

Figure 4.9

Reconstructions by linear interpolation from a concentric squares raster. (a) 16 projections (b) 32 projections (c) 64 projections (d) 128 projections.



(a)



(b)



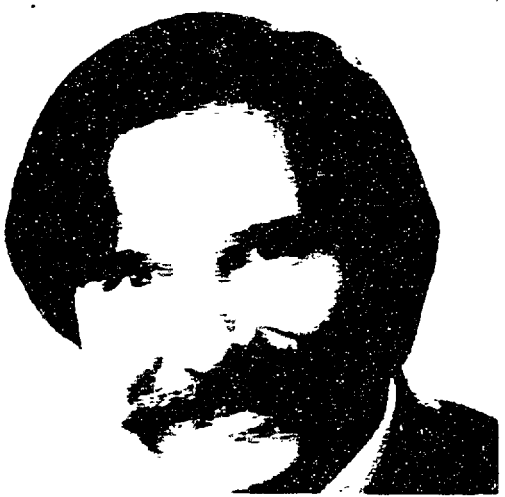
(c)



(d)

Figure 4.9

Reconstructions by linear interpolation from a concentric squares raster. (a) 16 projections (b) 32 projections (c) 64 projections (d) 128 projections.



(a)



(b)



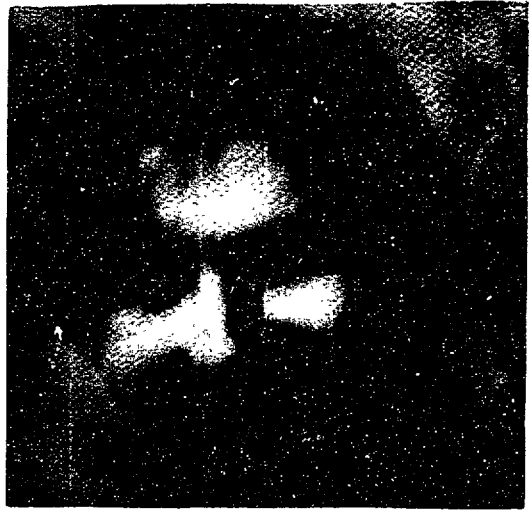
(c)

Figure 4.10

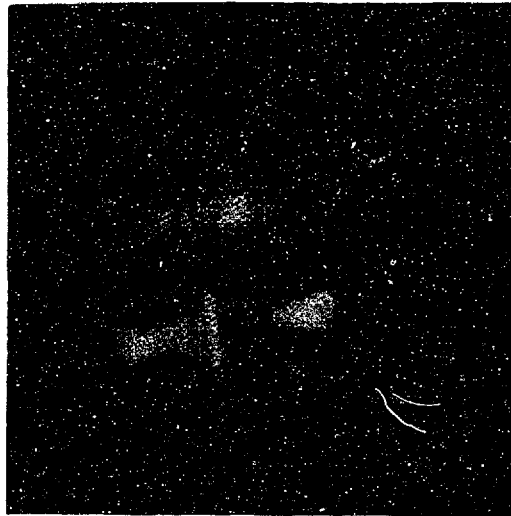
Comparison of the linear interpolation algorithm for polar samples and concentric squares samples. (a) original (b) reconstruction from 64 polar projections (c) reconstruction from 64 concentric squares projections.



(a)



(b)



(c)

Figure 4.10

Comparison of the linear interpolation algorithm for polar samples and concentric squares samples. (a) original (b) reconstruction from 64 polar projections (c) reconstruction from 64 concentric squares projections.

Let us examine each of these figures in turn. In figure 4.6 in the portrait we see that many features are reconstructed clearly. Some of the fine structure in the eyes and mouth is noticeable and the collar area is rather well resolved. Comparison with the original, however, shows us that the edges in the collar are not as sharp as they might be and that the hair, mustache, and eyes are not as detailed as in the original. The backgrounds in both the test pattern and the portrait are regular. In the test pattern the corner patterns are not resolved and the rays of the center pattern although resolved do not have sharp edges. There is also a slight directional bias in that the vertical rays are resolved better than the horizontal ones. This same observation was made concerning linear interpolation reconstructions made from a polar raster.

In comparing figures 4.7 and 4.8 we see that there are virtually no differences between the reconstructions made from the two different concentric squares rasters, at least for these examples. This is not entirely unexpected since the two rasters are quite similar.

In figure 4.9 we see the effect of varying the number of projections. Reconstruction quality improves with the number of projections as we would expect, but even the reconstruction made from 128 projections has its deficiencies. The details in the hair and mustache are not resolved and the whole reconstruction appears somewhat blurred. One possible explanation for these shortcomings is that this algorithm, like its polar counterpart ignores many of the polar samples near the center of the concentric squares raster, where $|F(\omega_x, \omega_y)|$ is large.

In figure 4.10 we compare the concentric squares and polar linear interpolation algorithms. For this example, at least, the concentric

squares reconstruction is better. In fact this same result is true for all other examples that have been tried as well. The background which should be regular is regular on the concentric squares reconstruction, but not the polar one. Also the hair, eyes, nose, mouth and collar are clearer in the squares reconstruction than in the polar one. This is probably due to the fact that the interpolation from the concentric squares raster is one-dimensional whereas it is two-dimensional from the polar one.

4.4.2 Reconstruction by High Order Interpolation along the Squares

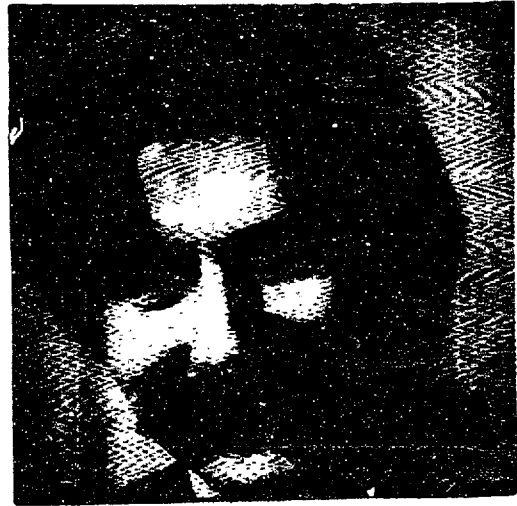
One difficulty with straightforward linear interpolation is that it does not utilize all of the information that is available from the projections, because it does not use all of the slice samples present in the concentric squares raster. We can modify the interpolation in polar coordinates algorithm to give a reconstruction technique which does use all of the slice samples. Instead of interpolating in polar coordinates, however, we wish to interpolate in "concentric squares coordinates" i.e. along the slices and along the squares. Any interpolation along slices is unnecessary since all of the concentric squares samples already lie on the squares which contain all of the DFT samples - such is the big advantage of concentric squares coordinates. Thus our algorithm reduces to the fairly simple task of making a high order polynomial interpolation along the sides of a series of concentric squares, a task which can be accomplished using a DFT.

Suppose for example that N_V slices intersect the vertical sides of an array of concentric squares where $N_V < N$. (If $N_V \geq N$, then by the arguments of section 4.3, exact reconstruction can be performed). We can approximate $F(\omega_x, \omega_y)$ along each vertical side by a polynomial of degree $N_V - 1$ in the variable $\exp[-j \frac{\pi}{W} \omega_y]$. Similarly if each horizontal side is intersected by N_H slices ($N_H < N$), we can approximate $F(\omega_x, \omega_y)$ along these lines by a polynomial of degree $N_H - 1$ in the variable $\exp[j \frac{\pi}{W} \omega_x]$. We know, however, that $f(x,y)$ is of finite order and that in fact $F(\omega_x, \omega_y)$ varies as a polynomial of degree $N - 1$ in the appropriate variable along all of these lines. Thus to the extent that the higher order polynomial can be closely approximated by the lower ones, we can expect an accurate reconstruction.

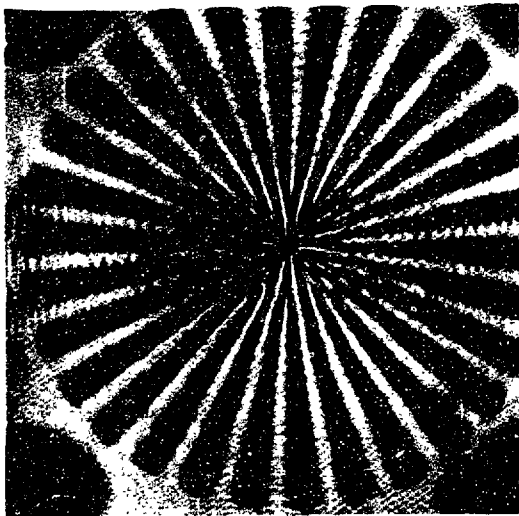
In figure 4.11 are two reconstructions performed by this technique. They are virtually identical to the reconstructions in figure 4.7 which were performed by linear interpolation. A similar result was observed in Chapter III when we compared the related polar algorithms. One possible explanation for the shortcomings of this algorithm is that in fact polynomials of degree $N_H - 1$ and $N_V - 1$ are not good approximations to polynomials of degree $N - 1$. (In these reconstructions $N_H = N_V = 32$, $N = 64$). It is known from results of numerical analysis that such is frequently the case. The approximation can be particularly bad near the extrema of the high order polynomial. It is also known that frequently an $N - 1$ st degree polynomial is better approximated by a series of lower order polynomial sections (or splines), such as linear or parabolic sections, than by higher order ones. It is possible that by using sections of intermediate order better reconstructions might be obtained than by either linear or maximum degree interpolation.



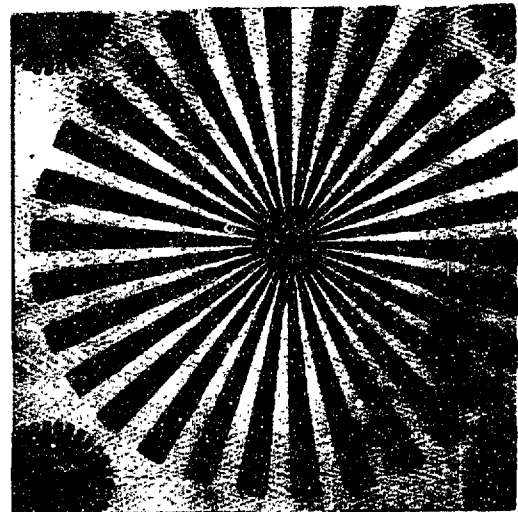
(a)



(b)



(c)



(d)

Figure 4.11

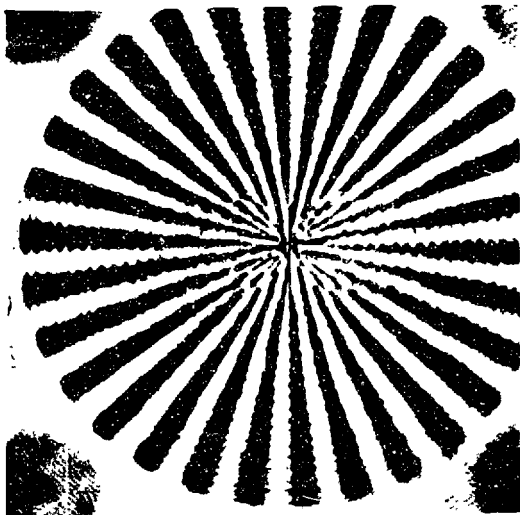
Reconstructions from 64 projections by approximating $F(\omega_x, \omega_y)$ along each side of the concentric squares by a polynomial of 32nd degree. (a) and (c) are reconstructions. (b) and (d) are originals.



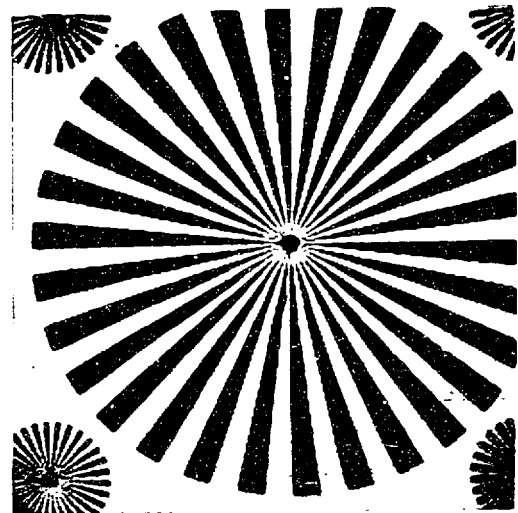
(a)



(b)



(c)



(d)

Figure 4.11

Reconstructions from 64 projections by approximating $F(\omega_x, \omega_y)$ along each side of the concentric squares by a polynomial of 32nd degree. (a) and (c) are reconstructions. (b) and (d) are originals.

4.4.3 Concentric Squares Smearing

As a final step in our development of parallel polar and concentric squares reconstruction algorithms, it remains to implement the smearing algorithm in concentric squares fashion. This is straightforwardly done.

First we express $F(\omega_x, \omega_y)$ in concentric squares coordinates where the variable ω designates the square and Θ designates the angular position on the square. Doing this we get

$$f(x,y) = \frac{1}{4\pi^2} \int_0^W \int_{-\pi}^{\pi} \frac{\hat{F}(\omega, \Theta)}{[\max(\cos^2 \Theta, \sin^2 \Theta)]} \exp[-j \frac{x\omega \cos \Theta + y\omega \sin \Theta}{\max(|\cos \Theta|, |\sin \Theta|)}] d\Theta d\omega \tag{4.10}$$

Let us now replace the integration in equation (4.10) by a sum where each summand represents the contribution to (4.10) from a small area in the (ω, Θ) plane as illustrated in figure 4.12. Our expressions and in fact the whole algorithm will be considerably simplified if the slices are assumed to intersect the concentric squares at evenly spaced points. In this special case the weighting factors which multiply the samples of $\hat{F}(\omega, \Theta) \exp [.]$ depend only on ω , not on Θ , which allows all projections to be treated identically. If we assume that N projections are taken and that M concentric squares are formed, then (4.10) can be approximated by:

$$f(x,y) \approx \frac{F(0,0)}{4\pi^2} + \frac{1}{N\pi^2} \sum_{i=-M/2+1}^{M/2} \sum_{k=0}^N \hat{F}(\frac{2W}{M} i, \Theta_k) \exp[j \frac{2W}{M} i \frac{(x \cos \Theta + y \sin \Theta)}{\max\{|\cos \Theta|, |\sin \Theta|\}}] \frac{2W}{M} i \tag{4.11}$$

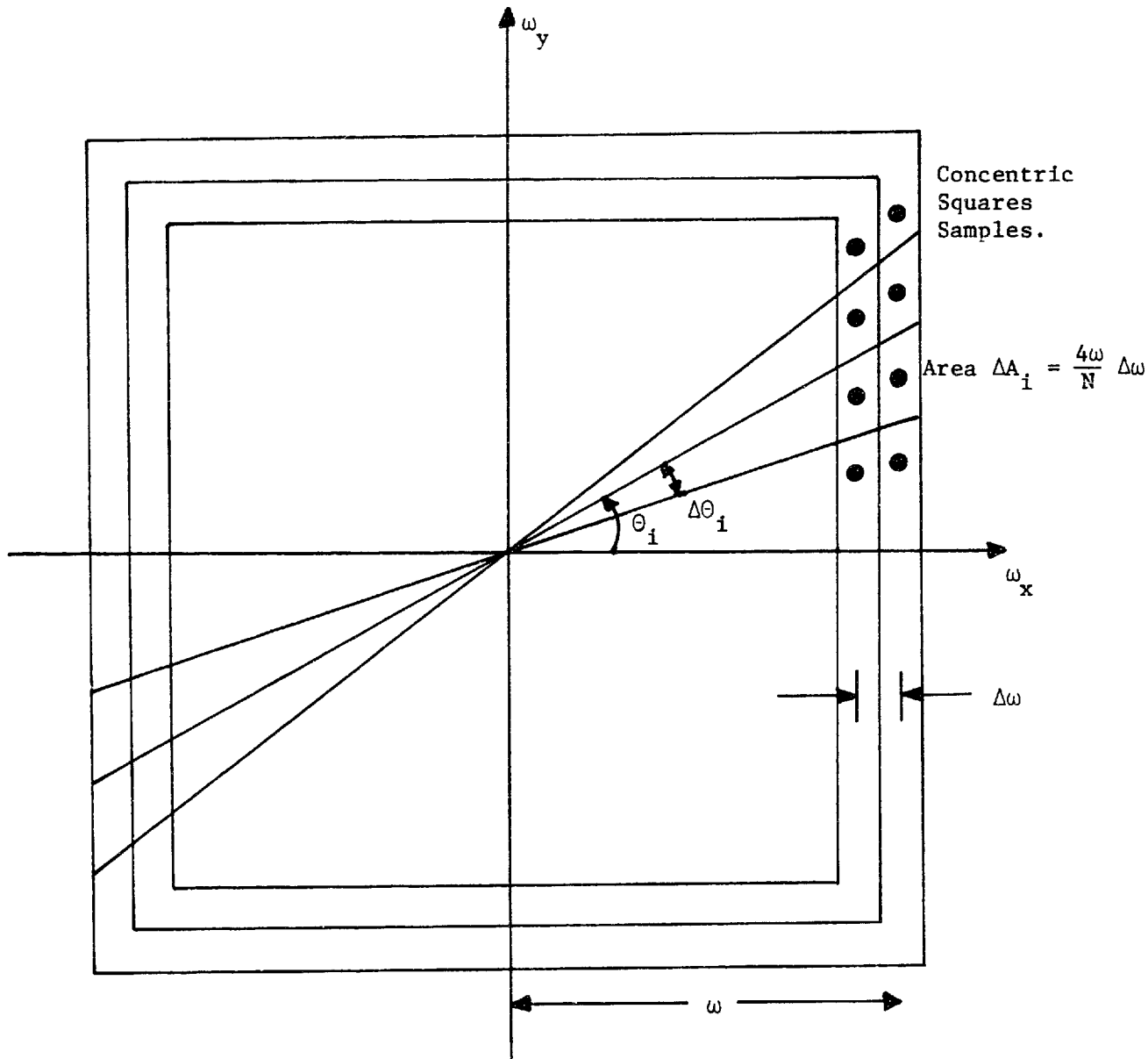


Figure 4.12

The area ΔA_i associated with one concentric squares sample when there are N projections with angles chosen so that the concentric squares samples are evenly spaced around the squares. In this special case ΔA_i is a function only of ω .

which can be rewritten in terms of the slices $\{S_{\theta_k}(\omega), 0 \leq k \leq N-1\}$ as

$$f(x,y) \approx \frac{S_{\theta_0}(0)}{4\pi^2} + \frac{2W}{Nm\pi^2} \sum_{i=-M/2+1}^{M/2} \sum_{k=0}^N i \hat{F}\left(\frac{2W}{M} i, \theta_k\right) \exp\left[j \frac{2Wi(x \cos\theta_k + y \sin\theta_k)}{M \max[\cos\theta_k, \sin\theta_k]}\right] \quad (4.12)$$

Equation (4.12) can be shown to have an interpretation in terms of smearing exactly as in the polar case. Each projection is taken, sampled, and transformed to give concentric squares samples of $F(\omega_x, \omega_y)$. They are then multiplied by the weighting function $|\omega|$, inverse transformed and back projected as before. As in the polar case, the mean gray levels of the original and of the reconstruction are constrained to be equal.

In figure 4.13 are presented some reconstructions generated by concentric squares smearing. It should be first noted that the quality of the reconstructions is very good. In the portrait all of the fine structure of the eyes is apparent, the edges around the collar are sharp and the background is fairly regular. The most obvious differences between the original and the reconstruction are in the hair, and mouth areas. With the test pattern all 4 of the corner patterns are resolved and the rays of the central pattern have fairly well defined edges. Here the major differences between original and reconstruction are in the center of the central test pattern and in the background. These reconstructions are also superior to the polar smearing reconstruction in figure 3.9.

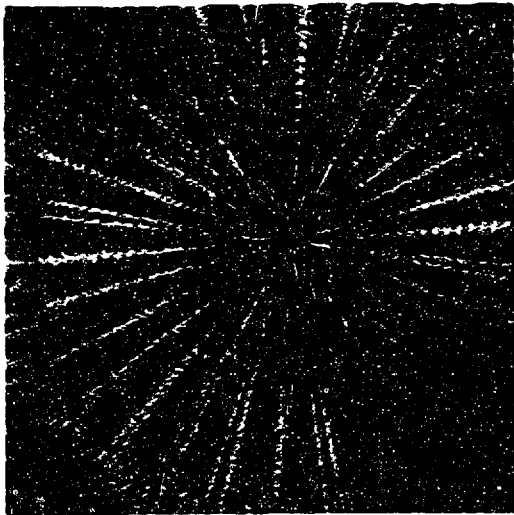
The good quality of the concentric squares reconstructions is somewhat surprising. In the case of linear interpolation it could be



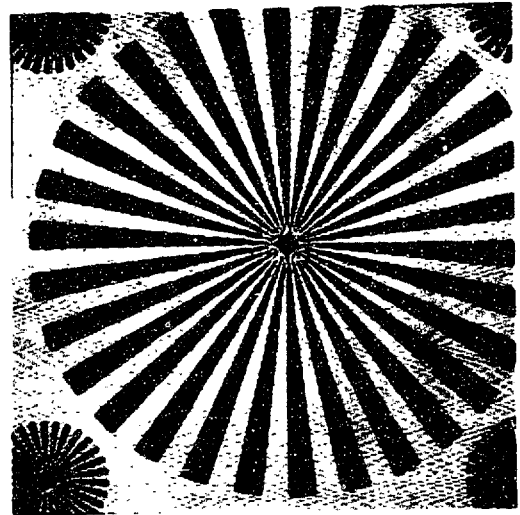
(a)



(b)



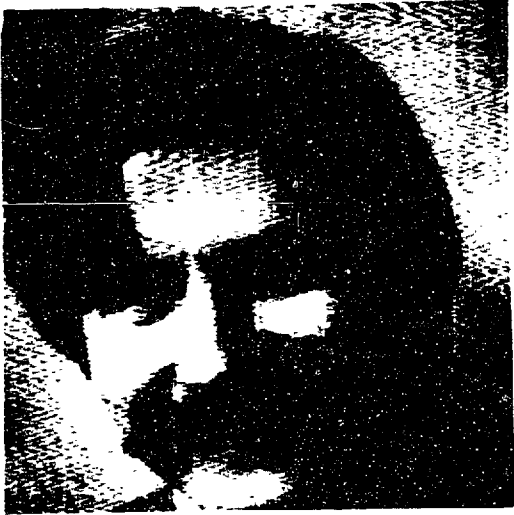
(c)



(d)

Figure 4.13

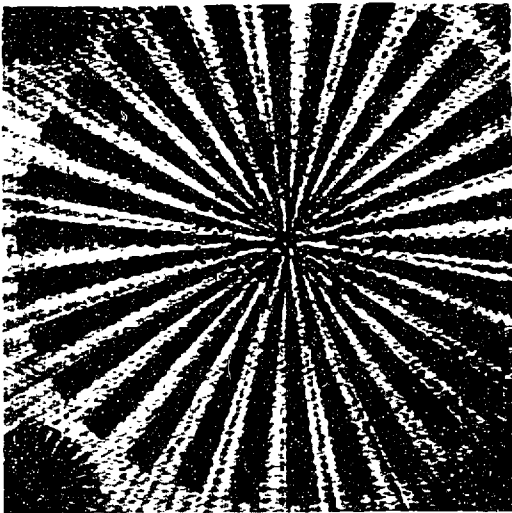
Some reconstructions made by smearing 64 concentric squares projections. (a) and (c) correspond to reconstructions. (b) and (d) are originals.



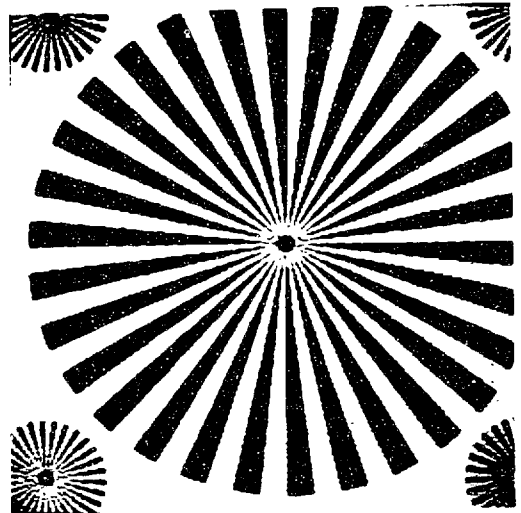
(a)



(b)



(c)



(d)

Figure 4.13

Some reconstructions made by smearing 64 concentric squares projections. (a) and (c) correspond to reconstructions. (b) and (d) are originals.

argued that improvement was due to the fact that one-dimensional interpolation could be performed instead of two-dimensional interpolation, but no such computations were carried out in the case of smearing. The noticeable difference in performance was probably due to the fact that concentric squares sampling gives more samples in the passband of $F(\omega_x, \omega_y)$ than does polar sampling.

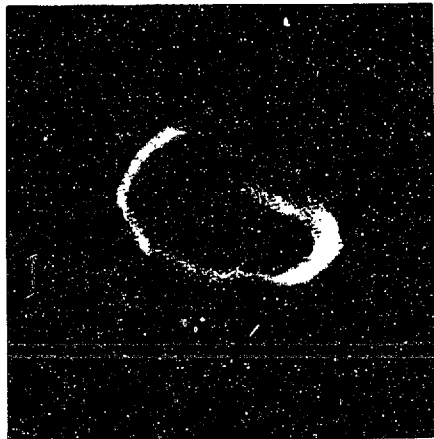
4.4.4 Reconstructions from Real Data

In an effort to see how well one of these algorithms would perform on real data, a series of x-rays of an excised human femur were obtained.* The complete series consisted of 36 x-rays which were taken normal to the long axis of the bone at 5° intervals. Since the algorithms were all designed to perform two-dimensional reconstructions from one-dimensional projections, each of the x-rays was sampled logarithmically along a single line normal to the long axis and a single cross section of the bone was reconstructed. Each projection was sampled at 256 by 256 points and the sampling interval was the same for each projection. These samples were used to compute both polar slice samples and concentric squares slice samples. The concentric squares linear interpolation reconstruction is presented in figure 4.14b and one of the x-rays from which it was produced is in 4.14a. The hollow tubular structure of the bone is evident from this reconstruction. In addition material of lighter density is seen inside the bone. The reconstruction from a polar grid was virtually identical. The other algorithms were not tried.

* The x-rays were provided by Dr. Oleh Tretiak



(a)



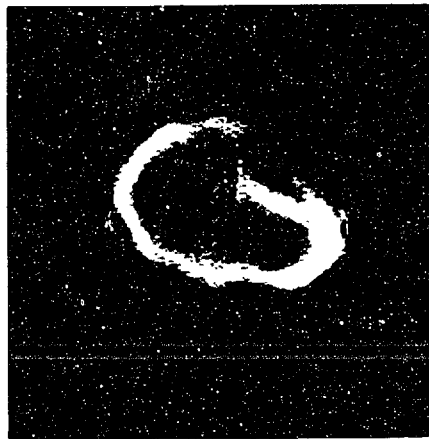
(b)

Figure 4.14

Reconstruction of a section of a leg bone from 36 evenly spaced projections by using linear interpolation from a concentric squares raster. (a) bone section at 30° angle (positive) (b) reconstruction of section at level of solid line in (a) (negative).



(a)



(b)

Figure 4.14

Reconstruction of a section of a leg bone from 36 evenly spaced projections by using linear interpolation from a concentric squares raster. (a) bone section at 30° angle (positive) (b) reconstruction of section at level of solid line in (a) (negative).

4.5 The Use of Projections to Characterize Pictures

It has been suggested that since pictures and other multidimensional signals can be approximated in terms of their projections then projections must characterize those pictures. Thus instead of storing an entire digitized picture which requires a large number of bits, perhaps just a limited number of projections can be stored, and when needed the picture can be reconstructed. This is a worthwhile procedure only if the total storage required is less than that required for the actual digitized picture, if a satisfactory image can be reconstructed, and if the process of reconstruction is computationally straightforward. In this section we shall consider the first of these three conditions without discussing the latter two, which should not imply that they are not definite issues.

Straightforward Cartesian sampling of pictures is often highly inefficient in that the total number of bits required to represent a picture in this fashion is considerably higher than can be achieved using other techniques. Straightforward sampling requires 5-6 bits per sample whereas it is believed to be possible to code a photograph exactly using only about 2 bits per sample. One can, of course, approximate a photograph with fewer bits. State of the art techniques for picture coding provide very good approximations to pictures using $1/2$ to 1 bit per sample.

We shall consider coding pictures by simply coding the projections. From the projections we can later approximate the picture. We shall assume that the projections are coded by sampling, although perhaps if more sophisticated techniques were used, the total number of bits employed could be reduced still further. The total number of bits/sample

needed to specify a picture can then be expressed as:

$$B = LMb/N^2 \quad (4.13)$$

where

B = total number of bits/sample

L = number of projections

M = number of samples/projection

b = number of bits/sample

N^2 = number of samples in reconstructed picture

In this section we shall vary the parameters L, M and b and see what effect these have on reconstruction quality. This study is not meant to be exhaustive but it will give us some feel for the relative importance of each of these parameters. This is perhaps the most important result of this section. We shall perform a number of reconstructions using the portrait photograph, and the concentric squares smearing algorithm. Some of these results are included in figure 4.15. Let us consider the effect of each of these parameters in turn.

Number of Projections (L)

Controlling the number of projections is the most obvious way to affect reconstruction quality. This is true for all of the reconstruction algorithms which have been tried. As a preliminary comment it should be noted that in many applications the number of projections is not control-



(a)



(b)



(c)



(d)

Figure 4.15

A comparison of different values of L , M , and b in the smearing algorithm. (a) $L=64$, $M=256$, $b=17$, ($4 \frac{1}{4}$ b/s)
(b) $L=64$, $M=32$, $b=8$ ($\frac{1}{4}$ b/s) (c) $L=64$, $M=64$, $b=8$,
($\frac{1}{2}$ b/s) (d) $L=64$, $M=128$, $b=8$ (1 b/s)



(a)



(b)



(c)



(d)

Figure 4.15

A comparison of different values of L , M , and b in the smearing algorithm. (a) $L=64$, $M=256$, $b=17$, ($4 \frac{1}{4}$ b/s) (b) $L=64$, $M=32$, $b=8$ ($\frac{1}{4}$ b/s) (c) $L=64$, $M=64$, $b=8$, ($\frac{1}{2}$ b/s) (d) $L=64$, $M=128$, $b=8$ (1 b/s)



(e)



(f)



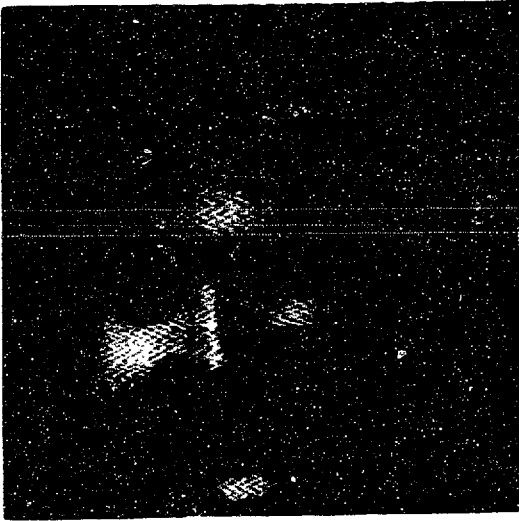
(g)



(h)

Figure 4.15 (cont'd)

(e) $L=64$, $M=256$, $b=8$ (2 b/s) (f) $L=32$, $M=64$, $b=8$
(1/4 b/s) (g) $L=128$, $M=64$, $b=8$ (1 b/s) (h) $L=128$,
 $M=128$, $b=8$ (2 b/s).



(e)



(f)



(g)



(h)

Figure 4.15 (cont'd)

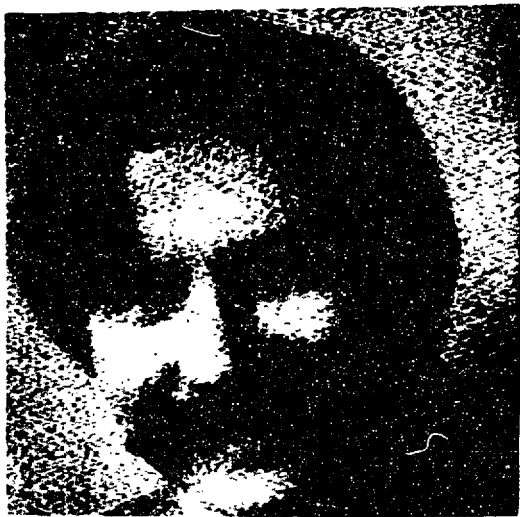
(e) $L=64$, $M=256$, $b=8$ (2 b/s) (f) $L=32$, $M=64$, $b=8$.
(1/4 b/s) (g) $L=128$, $M=64$, $b=8$ (1 b/s) (h) $L=128$,
 $M=128$, $b=8$ (2 b/s).



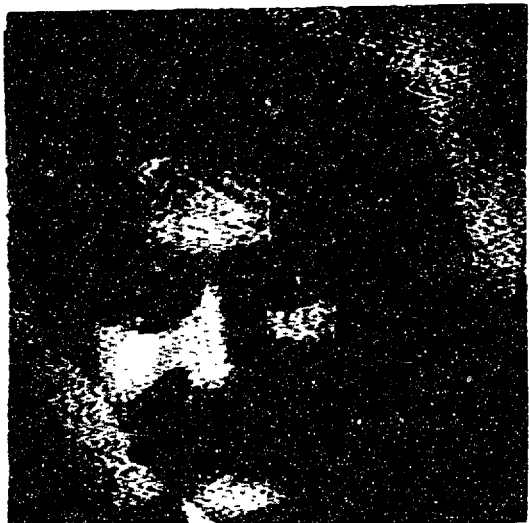
(i)



(j)



(k)



(l)

Figure 4.15 (cont'd)

(i) $L=64$, $M=64$, $b=5$ ($5/16$ b/s) (j) $L=64$, $M=128$,
 $b=5$ ($5/8$ b/s) (k) $L=64$, $M=256$, $b=5$ ($1\ 1/4$ b/s)
(l) $L=128$, $M=128$, $b=5$ ($1\ 1/4$ b/s).



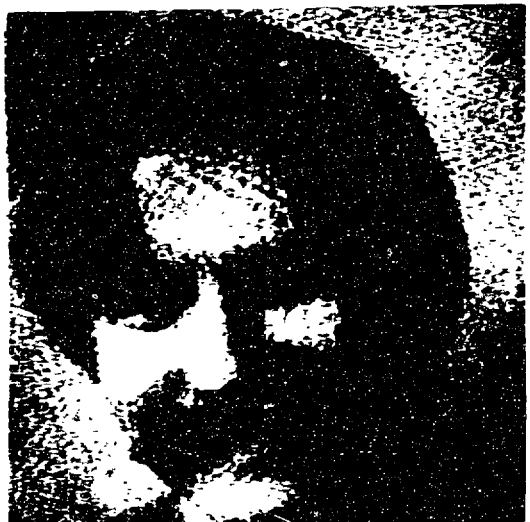
(i)



(j)



(k)



(l)

Figure 4.15 (cont'd)

(i) $L=64$, $M=64$, $b=5$ ($5/16$ b/s) (j) $L=64$, $M=128$,
 $b=5(5/8$ b/s) (k) $L=64$, $M=256$, $b=5$ ($1\ 1/4$ b/s)
(l) $L=128$, $M=128$, $b=5$ ($1\ 1/4$ b/s).

lable. In these cases one must of course use all of the projections that are available. In figures 4.15(c), (f) and (g) the same reconstruction was performed from 64, 32, and 128 projections respectively. It is perhaps also instructive to consider figures 3.10 and 4.9 where this effect was also considered for the polar coordinates smearing algorithm and concentric squares linear interpolation algorithm.

We first note that as the number of projections is increased the reconstructions become better. This is certainly not surprising. From a subjective evaluation of the portrait reconstructions it also appears that the incremental improvement in going from 32 to 64 projections is greater than that for going from 64 to 128. Although this may not be true for all pictures we have nonetheless used this fact so that most of the reconstructions in this dissertation are made from 64 projections.

Another item which must be mentioned whenever we address ourselves to the question of how many projections are necessary is - what resolution is required for the reconstruction being performed? At all times the relative cost of taking more projections must be balanced against the relative value of improved resolution. Furthermore the resolution of the reconstruction is limited by the resolution of each projection.

Number of Bits per Sample (b)

We can examine the effect of quantizing projections by comparing part (a) of figure 4.12 which was made using 17 bits with part (e) which was made with 8 bits and by comparing parts (c), (d), (e) and (h) which are made from 8 bit projections with (i), (j), (k), and (l) respectively which are made with 5 bit projections. The 17 bit reconstruction and the

8 bit reconstruction are virtually identical, but the 5 bit reconstructions are definitely degraded. Furthermore this degradation takes a specific form; the over-quantized projections yield reconstructions that have a mottled or snowy appearance as if an additive noise were added to them. Increasing the number of samples per projection atlers this noise but does not make it go away and increasing the number of projections will not remove it either.

Although any reconstruction algorithm can be expected to give degraded performance if the quantization is sufficiently severe, one should not infer that these results based on the smearing algorithm can be directly extended. This is due to the high frequency emphasis filter that is employed in the smearing algorithm. Since it represents essentially a numerical differentiator we expect it to magnify the quantization errors, present in the input projections. As a result, one might expect (although this fact has not been tested) that the parameter b has a greater effect on the smearing algorithm than on other algorithms.

Thus to yield good reconstructions more than 5 bits/sample are needed and 8 bits/sample seem to be sufficient. These results, however, are subjective and are based on a single example.

Number of Samples per Projection (M)

Here we can compare parts (b), (c), (d), and (e) of figure 4.12. The conclusion is obvious - reconstruction quality improves as the number of samples/projection increases, although for this example the improvement in going from 128 samples to 256 samples is small. Thus a reasonable strategy seems to be sample the projections as often as is feasible. Sam-

pling faster than the resolution implied by the projections does not bring much improvement in reconstruction quality but the costs of doing this are generally not great either, unless of course we put a large cost on the total number of bits required for storage of a picture. Doubling the number of projections to perform a reconstruction roughly doubles the effort required to obtain the projections, doubles the machine storage required to store them, and doubles the computation time for a reconstruction. Doubling the number of samples per projection, however, still doubles the storage requirement, but has only a small effect on the labor involved in obtaining projections and only a small effect on the total computation time. Thus increasing L is expensive while increasing M is fairly inexpensive. Thus projections should be sampled as often as machine storage will permit.

This result is in conflict with some earlier suggestions by other workers who expressed the belief that the radial frequency resolution should be constrained to be the same as the angular frequency resolution. This implies $L \approx M$. A comparison of the reconstructions in (c) and (e), however, shows that this constraint limits reconstruction quality.

The final measure of how many bits are required to store a picture in projection form depends to a large extent on how accurate we require the reconstructed picture to be, although it appears that good approximations can be obtained using less than 1 bit/sample.

Chapter V

EXACT RECONSTRUCTION FROM A SINGLE PROJECTION

5.1 Introduction

How many projections are needed to reconstruct a function exactly? In Chapter IV we saw that a bandlimited function of order N could be reconstructed exactly from $N + 1$ projections. If we impose no constraints whatsoever on the functions to be reconstructed then an infinite number of projections are required since each projection constrains $F(\omega_x, \omega_y)$ along only a single slice while it takes an infinite number of slices to span the whole Fourier plane. If we impose sufficient constraints on the unknown function then only a single projection might be necessary. For example, if we require that $f(x,y)$ be circularly symmetric, i.e. that $f(x,y) = g(\sqrt{x^2 + y^2})$ then only one projection is necessary. For these functions all of the projections are identical and therefore only one of them need actually be measured. This class of functions, unfortunately, is not particularly interesting because it is too restricted to represent most unknowns of interest. There is another class of functions, however, that can provide a good approximation to many frequently encountered unknowns and functions of this class can also be reconstructed from one projection. These are the bandlimited functions of finite order whose reconstruction from more than one projection was considered in Chapter IV. Unfortunately there are

difficulties associated with reconstructing these functions from a single projection and these will be discussed later in the chapter.

5.2 The One-Projection Theorem

The one-projection theorem which is presented below shows that bandlimited functions of finite order can be reconstructed from a single projection. It represents a specific case of a more general theorem which appears later in the section. It is perhaps instructive, however, to consider the special case first, for it is thus easier to understand the general theorem and the motivation for it.

Theorem (one-projection theorem): A bandlimited function $f(x,y)$ of order N can be reconstructed exactly from the single projection at angle $\theta_0 = \tan^{-1} 1/N$.

Proof: We can write $f(x,y)$ in terms of its Nyquist samples as

$$f(x,y) = \frac{\pi}{W^2} \sum_{m=0}^{N-1} \sum_{n=0}^{N-1} f\left(\frac{m\pi}{W}, \frac{n\pi}{W}\right) \frac{\sin\frac{W}{\pi}(x - \frac{m\pi}{W}) \sin\frac{W}{\pi}(y - \frac{n\pi}{W})}{(x - \frac{m\pi}{W})(y - \frac{n\pi}{W})} \quad (5.1)$$

From (5.1) we see that it is sufficient to specify $\{f(\frac{m\pi}{W}, \frac{n\pi}{W}), 0 \leq m, n \leq N - 1\}$ in order to completely specify $f(x,y)$. Evaluating the Fourier transform of $f(x,y)$ along a line at angle θ we obtain the slice at angle θ .

$$S_{\theta}(\omega) = F(\omega \cos\theta, \omega \sin\theta) = \frac{\pi}{W^2} \sum_{m=0}^{N-1} \sum_{n=0}^{N-1} f\left(\frac{m\pi}{W}, \frac{n\pi}{W}\right) \exp[-j\frac{\pi\omega}{W}(m \cos\theta + n \sin\theta)]$$

$x \qquad b_{\frac{W}{W}}(\omega \cos\theta, \omega \sin\theta)$ (5.2)

where as before W represents the bandwidth and

$$b_{WW}(\omega_x, \omega_y) = \begin{cases} 1 & |\omega_x| \leq W, |\omega_y| \leq W \\ 0 & \text{otherwise} \end{cases} \quad (5.3)$$

Setting $\theta = \theta_0 = \tan^{-1} 1/N$ it is straightforwardly seen that

$$\cos(\tan^{-1} 1/N) = \frac{N}{\sqrt{N^2 + 1}}$$

$$\sin(\tan^{-1} 1/N) = \frac{1}{\sqrt{N^2 + 1}}$$

$$S_{\theta_0}(\omega) = \frac{\pi^2}{W^2} \sum_{m=0}^{N-1} \sum_{n=0}^{N-1} f\left(\frac{m\pi}{W}, \frac{n\pi}{W}\right) \exp\left[-j \frac{\pi\omega(Nm + n)}{W\sqrt{N^2 + 1}}\right], \quad |\omega| < \frac{W}{N}\sqrt{N^2 + 1} \quad (5.4)$$

From (5.4) we see that $S_{\theta_0}(\omega)$ is a one-dimensional polynomial of degree $N^2 - 1$ in the variable $\exp\left[-j \frac{\pi\omega}{W\sqrt{N^2 + 1}}\right]$ and thus the coefficients of

that polynomial which are the function samples can be determined from any N^2 samples of $S_{\theta_0}(\omega)$ taken in the range $-\frac{W}{N}\sqrt{N^2 + 1} \leq \omega \leq \frac{W}{N}\sqrt{N^2 + 1}$.

Since these N^2 samples all lie on a single slice, they can be obtained from a single projection. This completes the proof.

In order to generalize the one projection theorem we might ask whether or not there are other slices which by themselves can reconstruct $f(x,y)$ (or its N^2 samples). We shall call such a slice a critical slice.

In general the set of angles which correspond to critical slices will be dependent on N, the order of $f(x,y)$.

From the one projection theorem we might wish to examine other slices which correspond to polynomials in one-variable to see if they too can be critical slices and if the coefficients of these polynomials can be related to picture samples. The following lemma tells us which slices represent polynomials.

Lemma: If A and B are positive integers, the Fourier transform of a bandlimited function of order N evaluated along the slice whose angle is $\theta = \tan^{-1} A/B$ corresponds to a polynomial over the range $|\omega_x| \leq W$, $|\omega_y| \leq W$, where W represents the bandwidth.

Proof: Using equation (5.2) to express $F(\omega_x, \omega_y)$ along this slice, we see that

$$\cos(\tan^{-1} A/B) = \frac{B}{\sqrt{A^2 + B^2}}$$

$$\sin(\tan^{-1} A/B) = \frac{A}{\sqrt{A^2 + B^2}}$$

$$S_{\theta}(\omega) = F\left(\frac{\omega B}{\sqrt{A^2 + B^2}}, \frac{\omega A}{\sqrt{A^2 + B^2}}\right) = \frac{\pi}{W^2} \sum_{m=0}^{N-1} \sum_{n=0}^{N-1} f\left(\frac{m\pi}{W}, \frac{n\pi}{W}\right) \exp\left[-j \frac{\pi\omega}{W\sqrt{A^2+B^2}}(Bm+An)\right] b_W(\omega)$$

(5.6)

where

$$b_W(\omega) = \begin{cases} 1 & , \quad |\omega| \leq \frac{W\sqrt{A^2 + B^2}}{\max[|A|, |B|]} \\ 0 & , \quad \text{otherwise} \end{cases}$$

From (5.6) it can be seen that $S_\Theta(\omega)$ corresponds to a polynomial in the variable $\exp[-j\frac{\pi\omega}{W\sqrt{A^2 + B^2}}]$ of degree $(A + B)(N - 1)$, for

$$\frac{-W\sqrt{A^2 + B^2}}{\max[|A|, |B|]} \leq \omega \leq \frac{W\sqrt{A^2 + B^2}}{\max[|A|, |B|]} \quad \text{QED.}$$

The conditions of this lemma are more restrictive than necessary. It is actually not necessary that A and B be positive. If A and B are both positive then the slice represents a polynomial of the form $P(Z) = a_Q Z^Q + a_{Q-1} Z^{Q-1} + \dots + a_0$ where $Q = (A + B)(N-1)$ and $Z = \exp[-j\frac{\pi\omega}{W\sqrt{A^2 + B^2}}]$. If we do not restrict the signs of A and B the slice will correspond to a polynomial of the form $P(Z) = a_Q Z^Q + a_{Q-1} Z^{Q-1} + \dots + a_P Z^P$ where $Z = \exp[-j\frac{\pi\omega}{W\sqrt{A^2 + B^2}}]$, $Q = \max(Bm + An)$, $0 \leq m, n \leq N-1$, and $P = \min(Bm + An)$, $0 \leq m, n \leq N-1$. P can and in general will be negative. Both polynomials are completely specified by $(|A| + |B|)(N-1) + 1$ samples. Therefore we shall say that the slice at angle $\Theta = \tan^{-1} A/B$ where A and B are (positive or negative) integers corresponds to a polynomial in $\exp[-j\frac{\pi\omega}{W\sqrt{A^2 + B^2}}]$ where the degree of that polynomial is defined by:

$$\begin{aligned} \text{degree of } S_\Theta(\omega) &= \max(Bm + An) - \min(Bm + An) \\ &\quad 0 \leq m, n \leq N-1 \quad 0 \leq m, n \leq N-1 \\ &= (|A| + |B|)(N - 1) \end{aligned} \quad (5.7)$$

From this lemma then, we see that slices with rational slopes satisfy our first requirement - they are polynomials. Furthermore as we can see from equation (5.6) the coefficients of these polynomials are either picture samples or sums of picture samples. In order that all of the picture samples be determinable from a single projection we must therefore impose the additional requirement that the coefficients of the slice polynomial each correspond to at most one picture sample. If a coefficient corresponded to a sum of picture samples, we would be able to determine the sum, but would have no means for determining the individual samples from the sum. We might at this point mention as an aside that perhaps if we allow ourselves to look at two or three projections we could relax this requirement. This we shall do in section 5.7 when we generalize these ideas to performing reconstructions from more than one projection. This additional requirement implies that the degree of the slice polynomial along a critical slice must be at least $N^2 - 1$, since there are N^2 different coefficients. Therefore we must require

$$(|A| + |B|)(N - 1) \geq N^2 - 1 \quad (5.8)$$

or

$$|A| + |B| \geq N + 1$$

This condition is necessary but not sufficient. In the next theorem we establish a necessary and sufficient condition on A and B for the slice at angle $\Theta = \tan^{-1} A/B$ to be a critical slice.

Theorem: If m, m', n and n' are integers in the range $0 \leq m, m', n, n' \leq N - 1$, if A and B have no common integer factor, and if the only solution to the equation

$$Bm + An = Bm' + An' \quad (5.9)$$

is the trivial solution $m = m', n = n'$ then the slice at $\Theta = \tan^{-1} A/B$ is a critical slice.

Proof: At this point the proof is nearly obvious. Since this slice has a rational slope we know that $S_{\Theta}(\omega)$ is a polynomial for $|\omega| \leq \frac{W\sqrt{A^2 + B^2}}{\max[|A|, |B|]}$. Furthermore if the conditions of this theorem are met then no two exponents in equation (5.6) can be equal. Thus no coefficients of the polynomial along this slice can correspond to the sum of two or more picture samples. Thus the polynomial corresponding to this slice must have at least N^2 distinct coefficients. Since every picture sample contributes to only one coefficient and since each coefficient depends on at most one sample, the picture samples can be determined from the coefficients. If the slice is completely specified (say by N^2 distinct samples) then since it is a polynomial its coefficients can be determined. Thus all N^2 picture samples can be determined from a single slice, which completes the proof.

Corollary: If N is the order of $f(x,y)$, then if P and N are relatively prime ($P \neq 0$), the slice at $\Theta = \tan^{-1} P/N$ is a critical slice.

Proof: Adapting equation (5.9) for this situation we see that the equation to test is

$$Nm + Pn = Nm' + Pn' \quad (5.10)$$

We wish to show that the only solution to (5.10) is the trivial one. Rearranging terms

$$N(m - m') = P(n' - n) \quad (5.11)$$

Here we see that since $N(m - m')$ is an integer and since N and P have no common factor, $P(n' - n)$ must be a multiple of both P and N . Thus for some integer i

$$P(n' - n) = iNP$$

or

$$n' - n = iN, \quad \text{since } P \neq 0 \quad (5.12)$$

However, due to constraints on the ranges of n and n' we know that $|n' - n| \leq N - 1$, which implies $i = 0$ in (5.12), which implies $n' - n = 0$. Substituting into (5.11) we also conclude that $m - m' = 0$. Therefore $n = n'$, $m = m'$. QED

Our original one projection theorem can be seen to follow directly from this corollary for the special case $P = 1$. In addition we

notice that in the special case where N is a power of two that the slices with slopes of $1/N, 3/N, 5/N, \dots, N-1/N$ are all critical slices.

Corollary: If $\theta = \tan^{-1} A/B$ is the angle of a critical slice, then $\theta_1 = \tan^{-1} B/A$, $\theta_2 = \tan^{-1} -A/B$, and $\theta_3 = \tan^{-1} -B/A$ are also the angles of critical slices.

(i) Proof for θ_1

We must test the equation

$$Am + Bn = Am' + Bn' \quad , \quad 0 \leq m, n, m', n' \leq N-1 \quad (5.13)$$

Since the range of all four variables is seen to be the same, we see that the solutions of (5.13) are the same as the solutions of

$$Bm + An = Bm' + An' \quad , \quad 0 \leq n, m, n', m' \leq N-1 \quad (5.14)$$

with the variables m and n interchanged and m' and n' interchanged. Since $\tan^{-1} A/B$ is a critical slice, however, the only solution to (5.14) is the trivial solution, hence this is the only solution to (5.13).

(ii) Proof for θ_2

Here we wish to test the equation

$$Bm - An = Bm' - An' \quad , \quad 0 \leq m, n, m', n' \leq N-1 \quad (5.15)$$

Substituting $r = N - 1 - n$, $r' = N - 1 - n'$ we get

$$B_m - AN + A + Ar = B_{m'} - AN + A + Ar'$$

or

$$B_m + Ar = B_{m'} + Ar' \tag{5.16}$$

However, we know that the only solution to (5.16) is $m = m'$, $r = r'$ which together imply, $n = n'$.

(iii) Proof for Θ_3

This can be shown by repeated application of the proofs for Θ_1 and Θ_2 .

QED

At this point several comments should be made. First all of the results derived in this chapter have assumed that the unknown signal could be represented by a square raster of samples N points on a side. We could, of course, have assumed with more generality that we had a rectangular raster of M samples in one dimension and N samples in the orthogonal dimension. None of our results would be substantially changed although the introduction of an additional parameter would have made the expressions slightly more complex. Seeing no particular reason (theoretical or practical) for introducing this extra parameter, we have chosen not to do so.

In addition we should comment on the degrees of the polynomials corresponding to the different critical slices. The preceding theorem has shown that there are an infinite number of critical slices. Each corresponds to a polynomial of degree at least $N^2 - 1$, since there are N^2 picture samples and thus N^2 different coefficients that each polynomial must contain. There is no maximum degree for these polynomials, however. For example consider the slice at $\theta = \tan^{-1} 1/2N$. From our theorems this is seen to be a critical slice and it corresponds to a polynomial of degree $2N^2 - N - 1$. Of the $2N^2 - N$ coefficients that it contains, however, only N^2 are non-zero (assuming that all of the picture samples are non-zero); $N^2 - N$ of the coefficients are identically zero. The slice at $\theta = \tan^{-1} 1/N$ can be seen to represent an optimum in the sense that of all the slices, this one is of minimum degree. As will be seen shortly, the ease of recovery of the picture samples from samples of a critical slice depends critically on the degree of the slice polynomial. The lower the degree of that polynomial, the easier it is to ascertain its coefficients. For this reason we shall consider the special case of the slice at $\theta = \tan^{-1} 1/N$ in the bulk of our discussions.

At this point we have also said nothing about how the projection corresponding to a critical slice should be sampled, or for that matter whether it should be sampled at all. Our sole requirement has been that a critical slice should be completely specified, presumably by a sufficient number of samples taken along the slice. In the special case $\theta_0 = \tan^{-1} 1/N$, N^2 samples are needed. These samples can be obtained by any method. If we wish to compute them digitally from a sampled projection, it is only necessary that the critical projection be sampled at a

rate higher than its Nyquist rate. Thus samples of the projection which correspond to concentric squares sampling, polar sampling, or some other sampling scheme could all be used. Each scheme when used with a DFT algorithm will produce its own set of slice samples. In practice some slice samples will prove more suitable than others for computing the coefficients but in theory the location of these samples along a critical slice is not important. As might be expected, the concentric squares type of sampling, since it corresponds to sampling at the Nyquist rate, an extremal value, yields the most tractable expressions for inversion, although there are severe difficulties with trying to invert from even these samples. Henceforth we shall assume this form of sampling in our discussions.

5.3 An Algorithm for Recovering the Picture Samples from One Projection

The problem at hand then is to estimate the samples $\{f(\frac{m\pi}{W}, \frac{n\pi}{W}), 0 \leq m, n \leq N-1\}$ of a bandlimited function of order N from samples of the slice at $\theta = \tan^{-1} 1/N$. Since this slice corresponds to a polynomial of degree $N^2 - 1$, we want to have N^2 samples along this slice. If they are obtained by sampling the projection at $\theta = \tan^{-1} 1/N$ at its Nyquist rate and then performing a DFT computation, the frequency samples will be equally spaced along the slice and they will extend along the whole non-zero frequency band. Since the width of this band is $\frac{2W\sqrt{N^2 + 1}}{N}$ the frequency spacing between adjacent samples is

$$\Delta\omega = \frac{2W}{N^3} \sqrt{N^2 + 1} \quad (5.17)$$

Thus substituting into equation (5.4), the values of the N^2 concentric squares slice samples are:

$$S_{\theta_o}(k\Delta\omega) = \frac{\pi}{W^2} \sum_{m=0}^{N-1} \sum_{n=0}^{N-1} f\left(\frac{m\pi}{W}, \frac{n\pi}{W}\right) \exp\left[-j\frac{2\pi k}{N^3}(Nm + n)\right] \quad (5.18)$$

$$k = -\frac{N^2}{2} + 1, \dots, 0, 1, \dots, \frac{N^2}{2}$$

For notational simplicity let us define $g(mN + n) = f\left(\frac{m\pi}{W}, \frac{n\pi}{W}\right)$. This mapping of a two-dimensional sequence to a one-dimensional sequence is unambiguous due to the limited ranges of m and n . Then setting $p = Nm + n$ it is seen that

$$S_{\theta_o}(k\Delta\omega) = \frac{\pi}{W^2} \sum_{p=0}^{N^2-1} g(p) \exp\left(-j\frac{2\pi kp}{N^3}\right), \quad k = -\frac{N^2}{2} + 1, \dots, \frac{N^2}{2} \quad (5.19)$$

Thus we have mapped the two-dimensional problem into a one-dimensional problem.

Before we discuss the problem of inverting equation (5.19) let us consider it for a moment. It says that to determine the slice samples $\{S_{\theta_o}(k\Delta\omega)\}$ from the N^2 picture samples, one should do the following: first take the array of picture samples and form an N^2 point, one-dimensional sequence from it by arranging the samples of the array column by column, then from this N^2 point sequence, an N^3 point sequence is formed by adding $N^3 - N^2$ samples of value zero, then an N^3 point DFT is taken of the whole sequence, from the resulting N^3 point sequence, the first $\frac{N^2}{2} + 1$ and the last $\frac{N^2}{2} - 1$ samples are saved and the rest are discarded.

These N^2 samples correspond to N^2 samples of the slice of the Fourier transform of the original array to within a multiplicative constant.

Some further insight can perhaps be gained into the relationships between bandlimited functions of finite order and their critical slices, by considering $S_{\Theta_0}(k\Delta\omega)$ over an extended range of k . The Fourier transform $F(\omega_x, \omega_y)$ can be determined from samples of $f(x, y)$ by means of

$$F(\omega_x, \omega_y) = \frac{\pi^2}{W^2} \sum_{m=0}^{N-1} \sum_{n=0}^{N-1} f\left(\frac{m\pi}{W}, \frac{n\pi}{W}\right) \exp[-j\frac{\pi}{W}(m\omega_x + n\omega_y)] b_{WW}(\omega_x, \omega_y) \quad (5.20)$$

If we ignore the box function we can define a periodically extended version of $F(\omega_x, \omega_y)$.

$$\tilde{F}(\omega_x, \omega_y) = \frac{\pi^2}{W^2} \sum_{m=0}^{N-1} \sum_{n=0}^{N-1} f\left(\frac{m\pi}{W}, \frac{n\pi}{W}\right) \exp[-j\frac{\pi}{W}(m\omega_x + n\omega_y)] \quad (5.21)$$

$\tilde{F}(\omega_x, \omega_y)$ is periodic in both ω_x and ω_y with period 2π in each. If we now consider the sequence $S_{\Theta_0}(k\Delta\omega)$ as defined by equation (5.19) over the extended range of k , $-\infty < k < \infty$, we see that $S_{\Theta_0}(k\Delta\omega)$ is a periodic sequence with period N^3 . If this slice is examined in the periodically extended Fourier plane we see that there are indeed N^3 samples of $S_{\Theta_0}(k\Delta\omega)$ between the origins of two periods of $\tilde{F}(\omega_x, \omega_y)$. We note the additional fact that a necessary and sufficient condition for the sequence $S_{\Theta_0}(k\Delta\omega)$ to be periodic is that the angle Θ_0 have a rational tangent. Also we see that from the periodicity of $\tilde{F}(\omega_x, \omega_y)$ all N^3 samples of $S_{\Theta_0}(k\Delta\omega)$ computed in accordance with (5.19) correspond to samples of $F(\omega_x, \omega_y)$ and that these samples lie on a series of parallel lines in the Fourier plane.

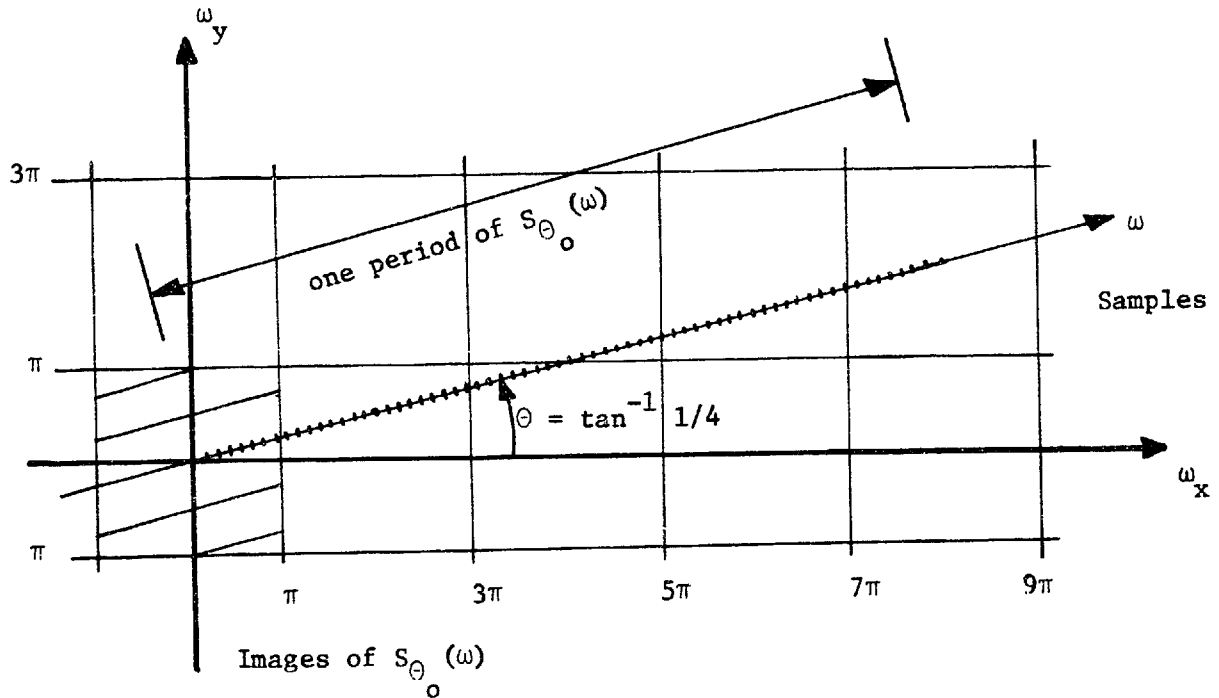


Figure 5.1

The samples corresponding to the extended definition of $S_{\theta_0}(k\Delta\omega)$ in terms of the periodically extended Fourier transform of a bandlimited function of order 4.

Thus if we know $F(\omega_x, \omega_y)$ we can generate the sequence $S_{\theta_0}(k\Delta\omega)$ for all k by sampling $F(\omega_x, \omega_y)$. This says, for example, that if we know only N^2 samples of $S_{\theta_0}(k\Delta\omega)$, it is in general difficult to extrapolate to compute the full N^3 values which constitute one period of $S_{\theta_0}(k\Delta\omega)$ and that simply assuming for example that these samples are all zero, will, in general, give poor results if this is tried as a means of estimating $\{f(\frac{m\pi}{W}, \frac{n\pi}{W})\}$.

These comments are intended to suggest that the inversion of (5.19) is not a simple operation. In the next section, however, we will present a technique for inverting it. Instead of inverting (5.19), however, we shall solve a slightly more general problem. This will be useful for slices other than the one at $\theta_0 = \tan^{-1} 1/N$. The algorithm for performing an inversion of an equation such as (5.19) has been called the Inverse Chirp z -Transform for reasons that will become evident in the next section.

5.4 The Inverse Chirp z -Transform Algorithm

Rabiner, Schafer, and Rader (44) have derived an algorithm which they call the Chirp z -Transform (CZT) algorithm, to efficiently compute the sum

$$X(z_k) = \sum_{n=0}^{L-1} x(n) z_k^{-n} \quad (5.22)$$

where $z_k = AW^{-k}$ for $k = 0, 1, \dots, M-1$.

The variable z_k is in general complex and thus the CZT is seen to be an efficient algorithm for evaluating a polynomial at points which are regularly spaced in the complex z -plane. In the special case $A = 1$,

$W = \exp[j \frac{2\pi}{L}]$, $M = L$ the CZT reduces to a computation of the DFT. If we set $A = \exp[-j \frac{2\pi}{N^2} (-\frac{N^2}{2} + 1)]$, $W = \exp[j \frac{2\pi}{N^3}]$, $L = M = N^2$, then we obtain equation (5.19). Therefore a procedure for inverting (5.22) will also invert equation (5.19). The $\{z_k\}$ correspond to M samples of a polynomial $X(z)$ by our generalized definition of a polynomial, and thus for $M \geq L$, if the $\{z_k\}$ are distinct, equation (5.22) can be inverted to yield $\{x(n)\}$.

A direct inversion using matrix techniques is impractical if L is large both because of large storage requirements and because of the amount of computation involved. Furthermore the matrix of coefficients $[z_k^{-n}]$ is nearly singular which makes a direct inversion highly sensitive to measurement or computational errors.

The approach which we will use is to employ Lagrange interpolating polynomials to reconstruct $X(z)$ from L of its samples, then use Cauchy's theorem to recover $x(n)$ from $X(z)$ by performing a contour integration in the complex z -plane. This latter step can be avoided by considering $x(n)$ as the unit sample response of a digital network and then exploiting the properties of digital networks.

Since $X(z)$ is a polynomial in z^{-1} of degree $L - 1$ which is specified at the points z_0, z_1, \dots, z_{L-1} (assume $M = L$) we can write

$$X(z) = \sum_{m=0}^{L-1} X(z_m) \ell_m(z^{-1}) \quad (5.23)$$

where $z_m = AW^{-m}$ and $\ell_m(z^{-1})$ is the Lagrange polynomial associated with z_m .

$$\ell_m(z^{-1}) = \frac{(z^{-1} - z_0^{-1})(z^{-1} - z_1^{-1}) \dots (z^{-1} - z_{m-1}^{-1})(z^{-1} - z_{m+1}^{-1}) \dots (z^{-1} - z_{L-1}^{-1})}{(z_m^{-1} - z_0^{-1})(z_m^{-1} - z_1^{-1}) \dots (z_m^{-1} - z_{m-1}^{-1})(z_m^{-1} - z_{m+1}^{-1}) \dots (z_m^{-1} - z_{L-1}^{-1})} \quad (5.24)$$

It can be noted that $\ell_m(z_m^{-1}) = 1$ and $\ell_m(z_n^{-1}) = 0$ if $m \neq n$. Since the denominator of the right-hand side of (5.24) is a constant which depends upon m but not upon z . Thus we shall call it $\frac{1}{C_m}$ and write (5.24) as

$$\ell_m(z^{-1}) = C_m (z^{-1} - z_0^{-1})(z^{-1} - z_1^{-1}) \dots (z^{-1} - z_{m-1}^{-1})(z^{-1} - z_{m+1}^{-1}) \dots (z^{-1} - z_{L-1}^{-1})$$

or

$$\ell_m(z^{-1}) = C_m \frac{\prod_{p=0}^{L-1} (z^{-1} - z_p^{-1})}{(z^{-1} - z_m^{-1})} \quad (5.25)$$

Thus substituting into (5.23)

$$X(z) = \sum_{m=0}^{L-1} C_m X(z_m) \frac{\prod_{p=0}^{L-1} (z^{-1} - z_p^{-1})}{(z^{-1} - z_m^{-1})} \quad (5.26)$$

The product term inside the summation is not a function of m , so it can be brought outside the summation

$$X(z) = \left[\prod_{p=0}^{L-1} (z^{-1} - z_p^{-1}) \right] \left[\sum_{m=0}^{L-1} \frac{-z_m C_m X(z_m)}{1 - z_m z^{-1}} \right] \quad (5.27)$$

We can consider $X(z)$ to be the z -transform of the unit sample response of a digital network, for which $x(n)$ is the unit sample response. Thus to determine $x(n)$ it is sufficient to simulate the digital network, excite it with a unit sample, and examine the output. From the form of (5.27) we see that the network can be realized as a cascade of a comb filter (the product term) and a bank of digital resonators (the sum term) as diagrammed in figure 5.2.

There is a further simplification that can be made. Let $h(n)$ represent the output of the bank of resonators. Then

$$h(n) = \sum_{m=0}^{L-1} z_m^n (-z_m C_m X(z_m)) \quad (5.28)$$

However, since $z_m = AW^{-m}$, (5.28) can be written as

$$\begin{aligned} h(n) &= \sum_{m=0}^{L-1} (-z_m C_m X(z_m)) A^n W^{-mn}, \quad n = 0, 1, \dots \\ &= A^n \sum_{m=0}^{L-1} (-z_m C_m X(z_m)) W^{-mn}, \quad n = 0, 1, \dots \end{aligned} \quad (5.29)$$

The only values of $x(n)$ which are needed are those for which $n = 0, 1, \dots, L-1$. Thus we only need to evaluate $x(n)$ for these L values. As a result since the comb filter can be realized as a causal filter, only the first L values of $h(n)$ need to be calculated. From (5.29) we see that if we restrict the range of n , $h(n)$ can be obtained by a CZT calculation. In particular if we introduce the notation

$$\text{CZT}(A, W, x(n), N) = \sum_{n=0}^{N-1} x(n) A^{-n} W^{nk} \quad (5.30)$$

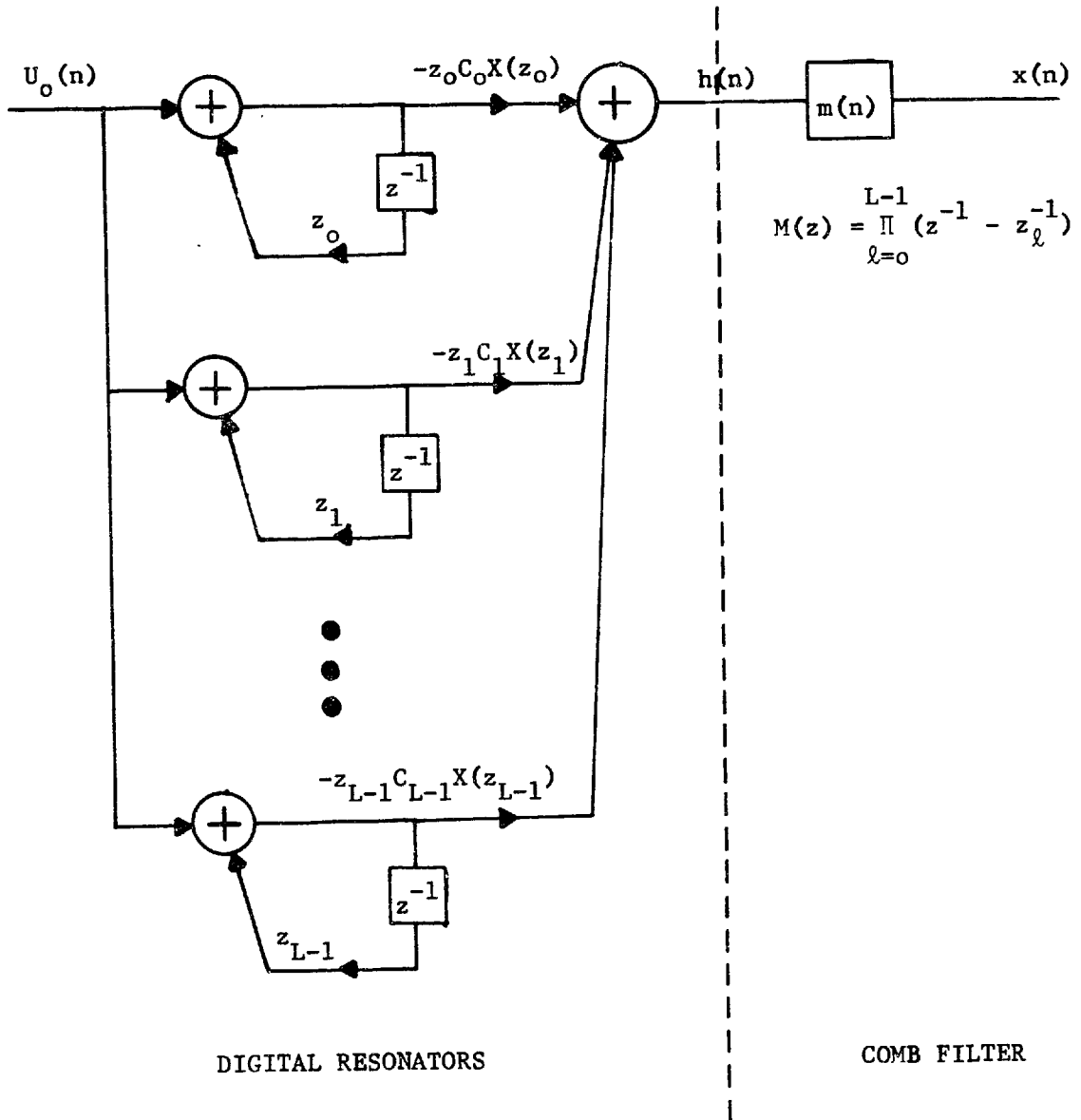


Figure 5.2

A digital network whose unit sample response is the solution to the inverse CZT problem.

then (5.29) becomes

$$h(n) = A^n \sum_{m=0}^{L-1} -z_m C_m X(z_m) W^{-mn} = -A^n \text{CZT}(1, W^{-1}, z_m C_m X(z_m), L) \quad (5.31)$$

Since the transfer function of the comb filter has only zeroes (except for poles at $z = 0$, its unit sample response is of finite length ($L + 1$ points) and thus the convolution implied by the cascade in our network structure can be implemented using high speed convolution techniques. Except for calculating the arrays $\{z_m C_m\}$ and $m(n)$ (the unit sample response of the comb filter), the only computations required for the inverse CZT are an array multiply, a CZT, and a high speed convolution. The arrays $\{z_m C_m\}$ and $m(n)$ require additional computation, of course, but they depend only upon A , W , and L and do not depend upon the data. Thus if several ICZT's are to be performed using the same parameters, these arrays do not have to be recomputed each time. The unit sample response of the comb filter $m(n)$ can be computed by actually iterating the comb filter network. The Lagrange coefficients can be generated recursively since

$$z_m C_m = z_{m-1} C_{m-1} \frac{W^{L-1} (W^{-m} - W^{-L})}{W^{-m} - 1} \quad (5.32)$$

$$z_0 C_0 = A^L \prod_{i=1}^{L-1} \frac{1}{1 - W^{-i}} \quad (5.33)$$

The Inverse CZT can be highly sensitive to errors in the values $X(z_k)$ and as a result, it is impractical for performing reconstructions

of large arrays of samples. This is not due to the specific algorithm presented here, but is due rather to equation (5.22) itself. The sensitivity of any technique for inverting equation (5.22) is discussed in the following section.

5.5 The Sensitivity of the Inverse Chirp z-Transform to Input Quantization Errors

In the last section an algorithm was presented for inverting the system of equations:

$$X(z_k) = \sum_{n=0}^{L-1} x(n) z_k^{-n} \quad (5.22)$$

$$z_k = A W^{-k}, \quad k = 0, 1, \dots, L-1$$

The sequence $X(z_k)$ can be considered as an input to the inverse CZT and $x(n)$ as an output. $X(z_k)$ will never be known exactly because of the effects of quantization when $X(z_k)$ is stored in a finite register length computer or because of measurement errors in determining $X(z_k)$. Furthermore we assumed in our derivation of the one-projection theorem, that $f(x,y)$ was a bandlimited function of finite order. Such may in fact not be the case and $f(x,y)$ may only be approximated by such a function. This will cause errors in the values of $X(z_k)$ as well.

We know that (5.22) can be inverted, for we have indeed found a technique for inverting it. Furthermore we know that the inverse mapping is linear. Thus we can write

$$x(n) = \sum_{i=0}^{L-1} P_{in} X(z_i) \quad (5.34)$$

The sensitivity of $x(n)$ to errors in $X(z_k)$ is due entirely to the magnitude of the $\{P_{in}\}$ and not to the technique by which they are evaluated, thus although there are severe difficulties in implementing the algorithm of section 5.4 this is not the fault of the algorithm, rather it is inherent in the problem itself. The analysis which follows is approximate so that a simple closed form result can be obtained, but experimental verification suggests that its predictions are reasonable. The simplifications which we shall make are appropriate if the inversion is used for the one-projection reconstruction of a large picture.

Assume that the input to the ICZT which ideally should be the sequence $X(z_i)$ is instead the sequence $X(z_i) + \Delta_i$ where Δ_i reflects the effect of measurement errors and is a complex random variable, which by assumption is independent of $X(z_i)$ and for which

$$E[\Delta_i] = 0 \quad , \quad i = 0, 1, \dots, L-1 \tag{5.35}$$

$$E[\Delta_i \Delta_j^*] = \sigma^2 \delta_{ij} \quad i, j = 0, 1, \dots, L-1$$

where $*$ denotes the complex conjugate, δ_{ij} denotes the Kronecker delta, and $E[\]$ denotes expected (mean) value. Let us further assume that the output of the ICZT to this input is $\{x(n) + \delta(n), n = 0, 1, \dots, L-1\}$ where $x(n)$ is the output when $\sigma^2 = 0$. Then

$$\begin{aligned} E[\delta(n)] &= E\left[\sum_{i=0}^{L-1} P_{in} (X(z_i) + \Delta_i) - \sum_{i=0}^{L-1} P_{in} X(z_i)\right] \\ &= E\left[\sum_{i=0}^{L-1} P_{in} \Delta_i\right] \\ &= \sum_{i=0}^{L-1} P_{in} E[\Delta_i] = 0 \end{aligned} \tag{5.36}$$

and

$$\begin{aligned}
 E[\delta(n) \delta^*(m)] &= E\left[\left(\sum_{i=0}^{L-1} P_{in} \Delta_i\right) \left(\sum_{j=0}^{L-1} P_{jm}^* \Delta_j^*\right)\right] \\
 &= \sum_{i=0}^{L-1} \sum_{j=0}^{L-1} P_{in} P_{jm}^* E[\Delta_i \Delta_j^*] \\
 &= \sum_{i=0}^{L-1} \sum_{j=0}^{L-1} P_{in} P_{jm}^* \sigma^2 \delta_{ji} \\
 &= \sigma^2 \sum_{i=0}^{L-1} P_{in} P_{im}^*
 \end{aligned} \tag{5.37}$$

To go further requires a specification of the matrix $[P_{ij}]$.

To determine $[P_{ij}]$ requires that we invert (5.20) which we can do by recognizing that $X(z)$ is a polynomial of degree $L-1$ and that the value of the polynomial can thus be determined at any point from M sample values of that polynomial which we have in the form of the samples $X(z_i)$. The sequence $x(n)$ can be obtained from $X(z)$ by finding the values of $X(z)$ at $z = \exp(j \frac{2\pi}{L} k)$ for $k = 0, 1, \dots, L-1$ and then performing an L - point inverse DFT.

$$\begin{aligned}
 x(n) &= \frac{1}{L} \sum_{k=0}^{L-1} \exp[j \frac{2\pi kn}{L}] \sum_{i=0}^{L-1} X(z_i) \ell_i(\exp[-j \frac{2\pi k}{L}]) \\
 &= \sum_{i=0}^{L-1} X(z_i) \frac{1}{L} \sum_{k=0}^{L-1} \ell_i(\exp[-j \frac{2\pi k}{L}]) \exp[j \frac{2\pi kn}{L}]
 \end{aligned} \tag{5.38}$$

where $\ell_i(\exp[-j\frac{2\pi k}{L}])$ is the Lagrange polynomial associated with z_i evaluated at $z = \exp[+j\frac{2\pi}{L}k]$. Comparing equations (5.38) and (5.34) we see that

$$P_{in} = \frac{1}{L} \sum_{k=0}^{L-1} \ell_i(\exp[-j\frac{2\pi k}{L}]) \exp[j\frac{2\pi nk}{L}] \quad (5.39)$$

thus we can write

$$\begin{aligned} E[\delta_n \delta_m^*] &= \sigma^2 \sum_{i=0}^{L-1} \left\{ \frac{1}{L} \sum_{k=0}^{L-1} \ell_i(\exp[-j\frac{2\pi k}{L}]) \exp[j\frac{2\pi kn}{L}] \right\} \left\{ \frac{1}{L} \sum_{p=0}^{L-1} \ell_i^*(\exp[-j\frac{2\pi p}{L}]) \exp[-j\frac{2\pi mp}{L}] \right\} \\ &= \frac{\sigma^2}{L^2} \sum_{k=0}^{L-1} \sum_{p=0}^{L-1} \exp[j\frac{2\pi}{L}(kn - mp)] \sum_{i=0}^{L-1} \ell_i(\exp[-j\frac{2\pi k}{L}]) \ell_i^*(\exp[-j\frac{2\pi p}{L}]) \end{aligned} \quad (5.40)$$

If we assume that $z_i = AW^{-i}$ where

$$\begin{aligned} W &= \exp[-j\frac{2\pi}{M}] \\ A &= \exp[j2\pi\theta_0] \end{aligned} \quad (5.41)$$

then

$$\ell_i(\exp[-j\frac{2\pi k}{L}]) = \frac{\prod_{\substack{s=0 \\ s \neq i}}^{L-1} (\exp[-j\frac{2\pi k}{L}] - \exp[-j2\pi(\theta_0 + \frac{s}{M})])}{\prod_{\substack{s=0 \\ s \neq i}}^{L-1} (\exp[-j2\pi(\theta_0 + \frac{i}{M})] - \exp[-j2\pi(\theta_0 + \frac{s}{M})])} \quad (5.42)$$

and

$$\ell_i(\exp[-j\frac{2\pi k}{L}])\ell_i^*(\exp[-j\frac{2\pi p}{L}]) =$$

$$\prod_{\substack{s=0 \\ s \neq i}}^{L-1} (\exp[-j\frac{2\pi k}{L}] - \exp[-j2\pi(\theta_o + \frac{s}{M})]) (\exp[j\frac{2\pi p}{L}] - \exp[j2\pi(\theta_o + \frac{s}{M})])$$

$$\prod_{\substack{s=0 \\ s \neq i}}^{L-1} (\exp[-j2\pi(\theta_o + \frac{i}{M})] - \exp[-j2\pi(\theta_o + \frac{s}{M})]) (\exp[j2\pi(\theta_o + \frac{i}{M})] - \exp[j2\pi(\theta_o + \frac{s}{M})])$$

$$= \frac{\prod_{\substack{s=0 \\ s \neq i}}^{L-1} \exp[j\pi(-\frac{k}{L} - \frac{s}{M} + \frac{p}{L} + \frac{s}{M})] 4 \sin(\pi(\theta_o + \frac{s}{M} - \frac{k}{L})) \sin(\pi(\theta_o + \frac{s}{M} - \frac{p}{L}))}{}$$

$$\prod_{\substack{s=0 \\ s \neq i}}^{L-1} 2(1 - \cos(\frac{2\pi}{M}(i - s)))$$

(5.43)

But

$$1 - \cos\frac{2\pi}{M}(i - s) = 2 \sin^2 \frac{\pi}{M}(i - s)$$

$$\approx 2(\frac{\pi}{M}(i - s))^2$$

This approximation is true if $\frac{\pi}{M}(i - s) \ll 1$ which is the case since for a 32 x 32 array $\frac{\pi}{M} \approx 10^{-4}$ and $|i - s| < 10^3$. Then

$$l_i \left(\exp \left[-j \frac{2\pi k}{L} \right] \right) l_i^* \left(\exp \left[-j \frac{2\pi p}{L} \right] \right) =$$

$$\frac{\prod_{\substack{s=0 \\ s \neq i}}^{L-1} \exp \left[j\pi \frac{(p-k)}{L} \right] \sin \left(\pi \left(\theta_o + \frac{s}{M} - \frac{k}{L} \right) \right) \sin \left(\pi \left(\theta_o + \frac{s}{M} - \frac{p}{L} \right) \right)}{}$$

$$\prod_{\substack{s=0 \\ s \neq i}}^{L-1} \frac{\pi^2}{M^2} (i-s)^2$$

$$= \frac{\exp \left[j\pi (p-k) \frac{L-1}{L} \right] \prod_{\substack{s=0 \\ s \neq i}}^{L-1} \sin \left(\pi \left(\theta_o + \frac{s}{M} - \frac{k}{L} \right) \right) \sin \left(\pi \left(\theta_o + \frac{s}{M} - \frac{p}{L} \right) \right)}{}$$

$$\left(\frac{\pi}{M} \right)^{2L-2} (i!)^2 ((L-i-1)!)^2$$

(5.44)

Now we shall make the assumption that $\sin \left(\pi \left(\theta_o + \frac{s}{M} - \frac{k}{L} \right) \right) \approx \sin \left(\pi \left(\theta_o - \frac{k}{L} \right) \right)$. This assumption is good if $\sin \left(\pi \left(\theta_o + \frac{s}{M} - \frac{k}{L} \right) \right) \approx 1$. If k is such that this sine is not approximately one, then this term will make a negligible contribution to the noise variance, so very little is lost by making this assumption.

Therefore,

$$l_i \left(\exp \left[-j \frac{2\pi k}{L} \right] \right) l_i^* \left(\exp \left[-j \frac{2\pi p}{L} \right] \right) \approx \frac{\exp \left(j \frac{L-1}{L} \pi (k-p) \right) \left[\sin \left(\frac{\pi k}{L} + \theta_o \right) \sin \left(\frac{\pi p}{L} + \theta_o \right) \right]^{L-1}}{\left(\frac{\pi}{M} \right)^{2L-2} (i!)^2 ((L-1-i)!)^2}$$

(5.45)

Thus

$$E[\delta_n \delta_m^*] = \frac{\sigma^2}{L^2} \left(\frac{M}{\pi}\right)^{2L-2} \sum_{k=0}^{L-1} \sum_{p=0}^{L-1} \exp\left[j\frac{2\pi}{L}(kn - pm + \frac{L-1}{L}(k - p))\right] \times$$

$$\left[\sin\left(\frac{\pi k}{L} + 2\pi\theta_o\right)\right]^{L-1} \left[\sin\left(\frac{\pi p}{L} + 2\pi\theta_o\right)\right]^{L-1} \sum_{i=0}^{L-1} \frac{1}{(i!)^2 ((L-1-i)!)^2}$$

(5.46)

Now we can consider the innermost summation. Using Sterling's approximation,

$$\sum_{i=0}^{L-1} \frac{1}{(i!)^2 ((L-1-i)!)^2} \approx \sum_{i=0}^{L-1} \frac{1}{i^{2i} e^{-2i} (L-i-1)^{2(L-i-1)} e^{-2(L-i-1)}}$$

$$\approx e^{2L-2} \left(\frac{2}{L}\right)^{2L-2}$$

(5.47)

The last step in the approximation is due to the fact that the only term in the summation which is significant is that for which $i \approx \frac{L}{2}$. With this approximation, equation (5.46) becomes

$$E[\delta_n \delta_m^*] = \frac{\sigma^2}{L^2} \left(\frac{2Me}{\pi L}\right)^{2L-2} \sum_{k=0}^{L-1} \sum_{p=0}^{L-1} \exp\left[j\frac{2\pi}{L}(kn - pm + \frac{L-1}{L}(k - p))\right] \times$$

$$\left[\sin\left(\frac{\pi k}{L} + 2\pi\theta_o\right) \sin\left(\frac{\pi p}{L} + 2\pi\theta_o\right)\right]$$

(5.48)

The double summation in (5.46) is dominated by the term $k = p \approx \frac{M}{2} - 2\pi\theta$ which has value approximately 1. Thus we finally get

$$E[\delta_n \delta_m^*] \approx \frac{\sigma^2}{L^2} \left(\frac{2Me}{\pi L}\right)^{2L-2} \quad (5.49)$$

For a 32 x 32 picture ($L = 10^3$, $M = 3 \times 10^4$) we find that $E[\delta_n \delta_m^*] \sim \sigma^2 \cdot 2^{12,000}$. Thus the ratio of the variance of the output noise to the variance of the input noise is roughly 12,000 bits! Thus equation (5.22) is ill-conditioned indeed for any but small values of L and M .

In table 5.1 some values of $\log_2 \frac{|\delta_n|^2}{\sigma^2}$ are computed for different values of L and M . It will be noted that the only sequences which are capable of being inverse chirp z-transformed are exceedingly short ones. In an effort to verify these figures, an inverse CZT was programmed using 36 bits for the representation of $X(z_k)$. According to (5.49) with this precision it should be possible to invert a 2 x 2 picture but not a 4 x 4 picture. The results of these inversions are summarized in tables 5.2 and 5.3. As expected the ICZT could invert a 2 x 2 picture, but we got meaningless results when we tried to recover a 4 x 4 picture from 16 samples of the slice at $\theta = \tan^{-1} 1/4$. Later results provided additional confirmation of equation (5.49).

The inverse CZT algorithm can also be used to recover a band-limited function of order N from $N + 1$ projections according to the procedure outlined in Chapter IV. In our demonstration that $N + 1$ projections were sufficient to specify the set of N^2 picture samples it was

<u>L</u>	<u>M</u>	<u>Bits</u>	<u>Corresponding Problem</u>
4	8	7	1 proj. reconst. 2 x 2 pict.
16	64	76	1 proj. reconst. 4 x 4 pict.
64	512	479	1 proj. reconst. 8 x 8 pict.
256	4096	2400	1 proj. reconst. 16 x 16 pict.
1024	32,768	11,800	1 proj. reconst. 32 x 32 pict.
4096	262,144	55,700	1 proj. reconst. 64 x 64 pict.
16,384	2,097,152	250,000	1 proj. reconst. 128 x 128 pict.
65,536	16,777,216	1,150,000	1 proj. reconst. 256 x 256 pict.
10	20	26	2 proj. reconst. 4 x 4 pict.
36	144	186	2 proj. reconst. 8 x 8 pict.
136	1088	1000	2 proj. reconst. 16 x 16 pict.
528	8448	5000	2 proj. reconst. 32 x 32 pict.
2080	66,560	24,000	2 proj. reconst. 64 x 64 pict.
22	44	64	4 proj. reconst. 8 x 8 pict.
76	304	400	4 proj. reconst. 16 x 16 pict.
380	3040	2900	4 proj. reconst. 32 x 32 pict.
1072	17,152	10,000	4 proj. reconst. 64 x 64 pict.

Table 5.1

The sensitivity of the inverse chirp z-transform for different values of L and M and the corresponding reconstruction problem for which these values are appropriate.

m	n	$f\left(\frac{m\pi}{W}, \frac{n\pi}{W}\right)$ actual	$f\left(\frac{m\pi}{W}, \frac{n\pi}{W}\right)$ reconstructed
0	0	0	$-3.045 \times 10^{-7} + j 2.808 \times 10^{-7}$
0	1	1.0	$.999992 - j 2.051 \times 10^{-7}$
1	0	0	$-1.926 \times 10^{-7} - j 1.365 \times 10^{-8}$
1	1	0	$-1.056 \times 10^{-7} - j 2.500 \times 10^{-7}$

Table 5.2

The reconstruction of a bandlimited picture of order 2
from the single projection at $\theta_0 = \tan^{-1} 1/2$.

m	n	$f\left(\frac{m\pi}{W}, \frac{n\pi}{W}\right)$ real	$f\left(\frac{m\pi}{W}, \frac{n\pi}{W}\right)$ reconstructed
0	0	1.0	$6.768 \times 10^2 + j 7.084 \times 10^2$
0	1	0	$-3.869 \times 10^2 + j 7.098 \times 10^2$
0	2	0	$-7.438 \times 10^2 + j 1.267 \times 10^3$
0	3	0	$-1.494 \times 10^2 + j 1.599 \times 10^3$
1	0	0	$-3.147 \times 10^3 + j 1.120 \times 10^3$
1	1	0	$1.451 \times 10^3 + j 3.532 \times 10^3$
1	2	0	$-5.072 \times 10^3 - j 2.434 \times 10^3$
1	3	0	$1.713 \times 10^3 + j 4.851 \times 10^3$
2	0	0	$-3.601 \times 10^3 - j 4.632 \times 10^3$
2	1	0	$-7.937 \times 10^2 + j 2.808 \times 10^3$
2	2	0	$5.742 \times 10^2 - j 2.580 \times 10^3$
2	3	0	$-2.739 \times 10^3 + j 3.110 \times 10^1$
3	0	0	$2.256 \times 10^3 - j 7.186 \times 10^2$
3	1	0	$-2.239 \times 10^3 - j 1.123 \times 10^5$
3	2	0	$2.223 \times 10^3 + j 6.109 \times 10^2$
3	3	0	$-1.454 \times 10^3 - j 6.536 \times 10^2$

Table 5.3

The reconstruction of a bandlimited picture of order 4
from the single projection at $\theta = \tan^{-1} 1/4$.

pointed out that a polynomial extrapolation was needed. For a judicious choice of projection angles, this can be accomplished using an ICZT. Here the values of L and M would be such that the computational errors might not be formidable. This algorithm has not been implemented, however.

5.6 Recovering a Bandlimited Three-Dimensional Function of Finite Order from a Single Projection

In section 5.3 we demonstrated that a two-dimensional bandlimited function of finite order could be reconstructed from a single projection. We then proceeded to show that this technique was in practice unusable because of computational difficulties. It is still an interesting and theoretically a potentially valuable technique, however. Here we shall consider three-dimensional functions of the same class. These can also be reconstructed in theory from a single projection although in practice, of course, we do not expect to be able to generate a viable reconstruction technique because of computational difficulties.

The simplest way to reconstruct a three-dimensional bandlimited function is to use the technique that was outlined in Chapter II and consider the three-dimensional unknown function as a stack of two-dimensional functions. We can consider these planar functions as lying parallel to the x - y plane of a coordinate system so that the variable z indexes a particular member of the stack. The two-dimensional projection is then taken by performing line integrals along lines normal to the projection plane, which we shall designate as the u - z plane. If the angle between the x - z plane and the u - z plane is chosen to be $\theta_0 = \tan^{-1} 1/N$

then the projection is a critical projection. Furthermore this two-dimensional critical projection can be considered to be a stack of one-dimensional projections each of which is a critical projection for one of the two-dimensional unknowns in the stack of unknowns. This is, of course, a straightforward extension of the two-dimensional problem and it suffers from all of the difficulties associated with that problem.

A more interesting approach to the three-dimensional problem is to parallel the reasoning which led to a solution of the two-dimensional problem. In that case we found a line in the Fourier plane, along which $F(\omega_x, \omega_y)$ corresponded to a polynomial; by knowing $F(\omega_x, \omega_y)$ along this line, we then knew all of the Nyquist samples of the unknown function, which completely specified it. Such a line exists in the three-dimensional case as well. One such line is that line which is traced out by the vector $\vec{\omega}_c$ where

$$\vec{\omega}_c = \left(\frac{N^2 \omega}{\sqrt{N^4 + N^2 + 1}}, \frac{N\omega}{\sqrt{N^4 + N^2 + 1}}, \frac{\omega}{\sqrt{N^4 + N^2 + 1}} \right) \quad (5.50)$$

Along this line $F(\omega_x, \omega_y, \omega_z)$ corresponds to a polynomial of degree $N^3 - 1$ and the coefficients of this polynomial are the samples of the unknown $\{f(\frac{m\pi}{W}, \frac{n\pi}{W}, \frac{p\pi}{W}), 0 \leq m, n, p \leq N-1\}$ where W is the bandwidth, defined as in the two-dimensional case. If we sample along this line at N^3 evenly spaced points across the band of $F(\omega_x, \omega_y, \omega_z)$ then

$$G(k\Delta\omega) = \sum_{m=0}^{N-1} \sum_{n=0}^{N-1} \sum_{p=0}^{N-1} f\left(\frac{m\pi}{W}, \frac{n\pi}{W}, \frac{p\pi}{W}\right) \exp\left[-j\frac{2\pi k}{N^3}(N^2 m + Nn + p)\right]$$

$$k = -\frac{N^3}{2} + 1, \dots, 0, 1, \dots, \frac{N^3}{2} \quad (5.51)$$

Equation (5.51) can be inverted to yield $f(\frac{m\pi}{W}, \frac{n\pi}{W}, \frac{p\pi}{W})$ using an inverse CZT with $L = N^3$, $M = N^5$. Thus as might be expected, performing the inversion in the three-dimensions is even more formidable than it was in two-dimensions. This particular line is not, of course, unique; there exist other critical lines and all of the theorems which were presented in the two-dimensional case can be extended to the three-dimensional case. This shall not be done here.

There is an important difference between the two and three-dimensional one projection reconstruction problems. The projection functions and the slice functions corresponding to a three-dimensional unknown are two-dimensional functions, i.e. they are defined on a plane. To reconstruct a three-dimensional function, however, only requires knowledge of $F(\omega_x, \omega_y, \omega_z)$ along a single one-dimensional line. The frequency response along this line can be evaluated directly from the samples of the two-dimensional projection (since the projection is a bandlimited function) or equivalently since the critical line is a one dimensional critical slice of a two-dimensional critical slice, a one-dimensional projection of the two-dimensional projection can be computed, sampled and then transformed. It must be remembered, however, when working with two-dimensional projection functions that although these are bandlimited functions, the bandwidths in the two orthogonal frequency variables will depend upon the orientations of the projections. In figure 5.3 we show the relevant parameters for computing the frequency response along the critical line given in (5.50) when the original slice is evaluated on the plane $\omega_x = N\omega_y$.

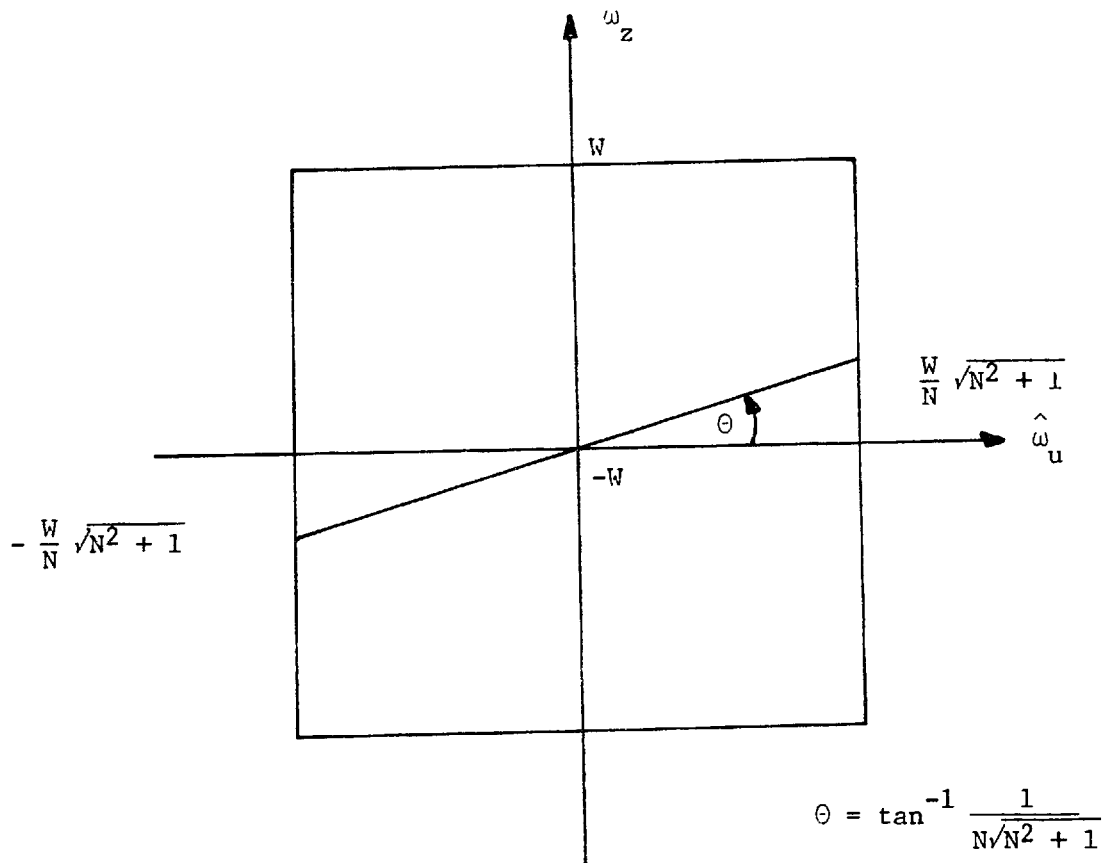


Figure 5.3

The location of one critical slice in recovering N^3 function samples of a three-dimensional bandlimited function of order N . The plane illustrated is that for which $\omega_x = N\omega_y$.

5.7 Using the Inverse CZT to Reconstruct Bandlimited Functions of Order N from More than One Projection

The problems that were discovered in reconstructing bandlimited functions of order N were computational ones and were due to the high orders of the polynomials involved. (In terms of equation 5.44 this is reflected in the parameter L). This is unavoidable, since to recover all N^2 samples from a single projection, it was necessary to work with a polynomial of degree greater than $N^2 - 1$. If, however, we are willing to use more than one projection, then perhaps we can work with lower order polynomials. Thus if we are prepared to do more than one inverse CZT, they each become easier to do. This procedure can perhaps best be explained in terms of an example.

Let us try to reconstruct a bandlimited picture of order 4 from the two projections at $\theta_1 = \tan^{-1} 1/2$ and $\theta_2 = \tan^{-1} -1/2$. Since each of these slices has a rational slope each corresponds to a polynomial of finite degree. In this case the degree is 9 and we can write

$$\begin{aligned}
 S_{\theta_1}(k\Delta\omega) &= f(0,0) + f(0,1)W + [f(0,2) + f(1,0)]W^2 + [f(0,3) + f(1,1)]W^3 \\
 &+ [f(1,2) + f(2,0)]W^4 + [f(1,3) + f(2,1)]W^5 + [f(2,2) + f(3,0)]W^6 \\
 &+ [f(2,3) + f(3,1)]W^7 + f(3,2)W^8 + f(3,3)W^9 \\
 &= \sum_{i=0}^9 A_i W^i \quad \text{where } W = \exp[-j\frac{2\pi k}{20}] \quad (5.52)
 \end{aligned}$$

Similarly we can write

$$\begin{aligned}
 S_{\Theta_2}(k\Delta\omega) &= f(0,3)W^{-3} + f(0,2)W^{-2} + [f(0,1) + f(1,3)]W^{-1} + [f(0,0) + f(1,2)] \\
 &+ [f(2,3) + f(1,1)]W + [f(2,2) + f(1,0)]W^2 + [f(2,1) + f(3,3)]W^3 \\
 &+ [f(2,0) + f(3,2)]W^4 + f(3,1)W^5 + f(3,0)W^6 \\
 &= \sum_{i=0}^9 B_i W^{i-3} \tag{5.53}
 \end{aligned}$$

If $S_{\Theta_1}(k\Delta\omega)$ and $S_{\Theta_2}(k\Delta\omega)$ are each available for 10 different evenly spaced values of k then we can perform two ($L = 10$, $M = 20$) ICZT's to obtain the two sequences A_i and B_i . From these we can compute the picture samples by:

$$\begin{array}{llll}
 f(0,0) = A_0 & f(1,0) = A_2 - B_1 & f(2,0) = B_7 - A_8 & f(3,0) = B_9 \\
 f(0,1) = A_1 & f(1,1) = A_3 - B_0 & f(2,1) = B_6 - A_9 & f(3,1) = B_8 \\
 f(0,2) = B_1 & f(1,2) = B_3 - A_0 & f(2,2) = A_6 - B_9 & f(3,2) = A_8 \\
 f(0,3) = B_0 & f(1,3) = B_2 - A_1 & f(2,3) = A_7 - B_8 & f(3,3) = A_9
 \end{array} \tag{5.54}$$

Referring to table 5.1 we see that to perform a 10/20 ICZT we get a sensitivity measure of 26 bits, whereas performing the same reconstruction from one projection we get a sensitivity measure of 76 bits. In tables 5.3 and 5.4 we see these two reconstructions

m	n	$f\left(\frac{m\pi}{W}, \frac{n\pi}{W}\right)$ actual	$f\left(\frac{m\pi}{W}, \frac{n\pi}{W}\right)$ reconstructed
0	0	0	$-1.341 \times 10^{-3} -j 7.690 \times 10^{-4}$
0	1	1.0000	$1.000 +j 3.962 \times 10^{-4}$
0	2	2.0000	$2.000 +j 7.804 \times 10^{-4}$
0	3	3.0000	$2.997 -j 1.088 \times 10^{-3}$
1	0	0	$-3.555 \times 10^{-3} -j 9.295 \times 10^{-4}$
1	1	1.0000	$1.004 +j 1.289 \times 10^{-3}$
1	2	2.0000	$2.001 +j 4.205 \times 10^{-4}$
1	3	3.0000	$2.995 +j 3.164 \times 10^{-4}$
2	0	0	$7.416 \times 10^{-3} +j 1.051 \times 10^{-3}$
2	1	1.0000	$.993 -j 4.296 \times 10^{-4}$
2	2	2.0000	$1.994 -j 1.585 \times 10^{-4}$
2	3	3.0000	$3.008 +j 1.093 \times 10^{-3}$
3	0	0	$-3.557 \times 10^{-4} +j 9.563 \times 10^{-4}$
3	1	1.0000	$.995 -j 9.980 \times 10^{-4}$
3	2	2.0000	$1.995 -j 7.756 \times 10^{-4}$
3	3	3.0000	$3.001 +j 9.189 \times 10^{-4}$

Table 5.4

The reconstruction of a bandlimited picture of order 4 from the projections at $\theta_1 = \tan^{-1} 1/2$ and $\theta_2 = \tan^{-1} (-1/2)$.

performed for a particular example. Here it can be noted that the reconstruction from 2 projections was successful in contrast to the one projection reconstruction.

The technique for performing a reconstruction from more than one projection following this approach can be summarized in the following steps.

- 1) Find a sufficient set of slice angles
- 2) Sample the slices at $d + 1$ points where d is the degree of the polynomial along each slice and compute the appropriate ICZT on each slice.
- 3) Set up a system of linear equations relating the outputs of the ICZT's to the picture samples.
- 4) Solve this set of equations to obtain the Nyquist samples of the picture.
- 5) Use the bandlimited interpolation formula (equation 5.1) to recover $f(x,y)$ from its Nyquist samples.

None of these steps is particularly simple. For example in our example we reconstructed from the slices at $\theta_1 = \tan^{-1} 1/2$ and $\theta_2 = \tan^{-1} -1/2$. Had we instead chosen to work with the slices at $\theta_1 = \tan^{-1} 1/2$ and $\theta_2 = \tan^{-1} 2$, which are of the same degrees, we would not have been able to solve the resulting linear equations. We must therefore be careful when we choose a set of slice angles. The only way to find a sufficient set of slices is to set up the necessary linear equations and see if they are solvable. This is difficult to do for large N since the number of equations and the number of variables grows as N^2 . It can be shown that the projections at $\theta_1 = \tan^{-1} 2/N$ and $\theta_2 = \tan^{-1} -2/N$ are sufficient

to reconstruct a function of order N , although from table 5.1 we see that for $N \geq 4$ it is difficult to perform the ICZT's on finite register length machines. It can also be shown that an 8×8 picture ($N = 8$) can be reconstructed from the four projections. $\theta_1 = \tan^{-1} 1/2$, $\theta_2 = \tan^{-1} 2$, $\theta_3 = \tan^{-1} -1/2$, and $\theta_4 = \tan^{-1} -2$. In all of these cases the inverse matrices for solving the resulting linear equations are straightforward to compute.

From table 5.1 we can perhaps infer that to reconstruct an $N \times N$ picture will require on the order of $N/2$ projections by these techniques, because of the sensitivity problems associated with the ICZT's. Since for large values of N this requires formidable matrix manipulations and since in Chapter 4 we discovered some techniques for performing good quality approximate reconstructions using the same numbers of projections, these techniques would not be used in practice. Nonetheless they do exhibit the tremendous amount of structure that is inherent in bandlimited functions of finite order.

These algorithms which perform a reconstruction by first setting up linear equations and then solving them, are reminiscent of the algorithms of Herman, Gordon et al. (2), (19), (20), (24), (25), (30), (31) which they call ART (Algorithm Reconstruction Techniques). With their techniques, linear equations are formulated in the space domain by comparing actual projections with the projections that would be made by an array of point masses. From the solutions to these equations, the point masses are estimated, which provide an approximation to the unknown. What is particularly interesting about their algorithm is that

it provides good reconstructions even when the number of equations is considerably less than the number of unknowns. This is accomplished by choosing the solution to the set of equations which represents the most likely unknown in some sense.

Chapter VI

SUMMARY AND SUGGESTIONS FOR FURTHER RESEARCH

6.1 Summary

In this dissertation we have suggested and compared several different algorithms for reconstructing multidimensional signals from their projections. Comparisons between the different algorithms were made by comparing the abilities of each algorithm to reconstruct a series of photographs from 64 computer generated projections. Special attention was paid to bandlimited functions since these functions can be completely specified by their samples. Thus such functions are readily suited for digital processing.

For functions which are bandlimited within a square in the Fourier domain, the idea of varying the sampling rate of each projection with the projection angle was suggested. This allowed us to specify $F(\omega_x, \omega_y)$ the Fourier transform of our unknown signal $f(x,y)$ on a concentric squares raster of points in the Fourier plane instead of on a polar raster which would result if all projections were sampled identically. On all of the examples which were tried the reconstructions from a concentric squares raster were of higher quality than those from a polar raster. One of the concentric squares algorithms was used to reconstruct a cross-section of a bone from 36 x-ray photographs.

It was also shown that bandlimited functions of finite order could be reconstructed from a finite number of projections. In fact it was shown that such functions could be reconstructed from a single projection.

6.2 Suggestions for Further Research

Perhaps the most obvious extension of this work that can be performed is the discovery of other and hopefully better reconstruction algorithms. More important than this, however, is the need for an extensive evaluation of some of the simple algorithms such as the ones presented in this dissertation. In section 4.5 the effect of such parameters as the number of projections, the number of samples per projection and the number of bits to be used in the representation of each sample was examined for a particular algorithm - the concentric squares smearing algorithm. These issues are related to such real-world effects as the effect of limited projection resolution, the effect of additive noise in the projections, and improper angular specification of the projections. It would be useful to know how sensitive the simple reconstruction algorithms are to these potential sources of error.

If reconstructions are to have any value for picture storage then in addition to considering the reconstruction problem it is necessary to consider the problem of computing projections. If the unknown function is bandlimited, this calculation is straightforward but computationally involved. It remains to be seen what effects computational approximations have on the final reconstructions.

Another area where more work can certainly be done concerns the one projection theorem. Here we have a powerful technique, which has proven to be useful, theoretically at least in the reconstruction problem. To what other problems can it be applied? Since it provides a mapping (which is invertible) between a class of two-dimensional functions and a class of one-dimensional functions, it would appear to be applicable to other problem areas, such as for example, the problem of designing multidimensional digital filters, particularly filters with finite duration unit sample responses, since these are the counterparts of bandlimited functions of finite order.

REFERENCES

1. S.H. Bellman, R. Bender, R. Gordon, and J.E. Rowe, "ART is science, being a defense of algebraic reconstruction techniques for three-dimensional electron microscopy," J. Theo. Biol., vol. 32, pp. 205-216 (1971).
2. R. Bender, S.H. Bellman, and R. Gordon, "ART and the ribosome: a preliminary report on the three-dimensional structure of individual ribosomes determined by an algebraic reconstruction technique," J. Theo. Biol., vol. 29, pp. 483-487, (1970).
3. R.N. Bracewell, "Strip integration in radio astronomy," Aust. J. of Phys., vol. 9, pp. 198-217, (1956).
4. R.N. Bracewell, and A.C. Riddle, "Inversion of fanbeam scans in radio astronomy," The Astrophysical Journal, vol. 150, pp. 427-434, (1967).
5. S.K. Chang, "The reconstruction of binary patterns from their projections," Comm. of the ACM, vol. 14, pp. 21-25, (1970).
6. S.K. Chang, and G.L. Shelton, "Two algorithms for multiple view binary pattern recognition," IEEE Trans. on Syst., Man, and Cyb., vol. SMC-1, pp. 90-94, (1971).
7. R.A. Crowther, "Three-dimensional reconstruction and the architecture of spherical viruses," Endeavor, vol. 30, p. 124.
8. R.A. Crowther, "Procedures for three dimensional reconstruction of spherical viruses by Fourier synthesis from electron micrographs," Phil. Trans. Roy. Soc. Lond. B, vol. 261, pp. 221-230, (1971).
9. R.A. Crowther, and L.A. Amos, "Three-dimensional Image Reconstruction of Some Small Spherical Viruses," Cold Spring Harbor Symposium on Quantitative Biology, vol. 36, p. 489, (1971).
10. R.A. Crowther, L.A. Amos, J.T. Finch, D.J. DeRosier, and A. Klug, "Three dimensional reconstructions of spherical viruses by Fourier synthesis from electron micrographs," Nature, vol. 226, pp. 421-425, (1970).
11. R.A. Crowther, and Linda Amos, "Harmonic analysis of electron microscope images with rotational symmetry," J. Mol. Biol., vol. 60, pp. 123-130, (1971).
12. R.A. Crowther, D.J. DeRosier, and A. Klug, "The reconstruction of a three-dimensional structure from projections and its application to electron microscopy," Proc. Roy. Soc. Lond. A., vol. 317, pp. 319-340, (1970).

13. R.A. Crowther, and A. Klug, "Art and science or conditions for three-dimensional reconstruction from electron micrograph images," J. Theo. Biol., vol. 32, pp. 199-203, (1971).
14. D.J. DeRosier, "The reconstruction of three-dimensional images from electron micrographs," Contemp. Phys., vol. 12, #5, pp. 437-452.
15. D.J. DeRosier, "Three-dimensional image reconstruction from electron micrographs by digital processing," Nerem Record, p. 118, (1969).
16. D.J. DeRosier, "Three-dimensional image reconstruction of helical structures," Berichte Der Bunsen-Gesellschaft, vol. 74, #11, pp. 1127-1128, (1970).
17. D.J. DeRosier and A. Klug, "Reconstruction of three-dimensional structures from electron micrographs," Nature, vol. 217, pp. 130-134, (1968).
18. D.J. DeRosier and P.B. Moore, "Reconstruction of three-dimensional images from electron micrographs of structures with helical symmetry," J. Mol. Biol., vol. 52, pp. 355-369, (1970).
19. G. Frieder and G.T. Herman, "Resolution in reconstructing objects from electron micrographs," J. Theo. Biol., vol. 33, pp. 189-211, (1971).
20. N.T. Gaarder and G.T. Herman, "Algorithms for reproducing objects from their x-rays," Pre-print.
21. J.B. Garrison, D.G. Grant, W.H. Guier, and R.J. Johns, "Three-dimensional roentgenography," Am. J. of Roentgenology, Rad. Therapy, and Nuc. Med., vol. 60, #4, pp. 903-908, (1969).
22. Robert M. Glaeser, "Limitations to significant information in biological electron microscopy as a result of radiation damage," J. of Ultra. Res., vol. 32, pp. 466-492, (1971).
23. B. Gold and C. Rader, Digital Processing of Signals, McGraw-Hill, New York, 1969.
24. R. Gordon, R. Bender, and G.T. Herman, "Algebraic reconstruction techniques (art) for three-dimensional electron microscopy and x-ray photography," J. Theo. Biol., vol. 29, pp. 471-481, (1970).
25. R. Gordon, and G.T. Herman, "Reconstruction of pictures from their projections," Comm. Acm., vol. 14, #12, pp. 759-768, December 1971.
26. D.G. Grant, J.B. Garrison, and R.J. Johns, "Three-dimensional radio-graphy," APL Technical Digest, pp. 10-15, January 1970.

27. D.G. Grant, "Tomosynthesis: A three-dimensional radiographic imaging technique," IEEE Transactions of Biomedical Eng., BME-19, pp. 20-28, January 1972.
28. R.G. Hart, "Electron microscopy of unstained biological material: the polytropic montage," Science, vol. 159, pp. 1464-1467.
29. R.G. Hart and J.M. Yoshiyama, "Polytropic montage: ribosomes examined in a tissue section," Proceedings of the National Acad. of Sciences, vol. 65, #2, pp. 402-408, February 1970.
30. G.T. Herman, "Two direct methods for reconstructing pictures from their projections: a comparative study," Pre-print.
31. G.T. Herman and St. Rowland, "Resolution in art: an experimental investigation of the resolving power of an algebraic picture reconstruction technique," J. Theo. Biol., vol. 33, pp. 213-223.
32. T.S. Huang, Personal Communication.
33. J.W. Klovstad, "Object reconstruction from shadow images," MIT, S.M. Thesis, (1969).
34. A. Klug, "Applications of image analysis techniques in electron microscopy," Phil. Trans. Roy. Soc. Lond. B., vol. 261, pp. 173-179.
35. R.P. Kruger, E.C. Mahen, A.J. Carlson, S.J. Dwyer, and G.S. Lodwick, "Image analysis of radiograms," 21st Annual Conference, Southwestern I.E.E.E., pp. 147-151.
36. R.M. Mersereau, "The digital reconstruction of multidimensional signals from their projections," Proceedings of the Tenth Annual Allerton Conference on Circuit and System Theory, University of Illinois, 1972.
37. R.M. Mersereau, "Recent advances in theory of reconstructing multidimensional signals from projections," QPR #105, pp. 169-183.
38. R.M. Mersereau, "Reconstruction of multidimensional signals from projections," Arden House Workshop on Digital Filtering, 1972
39. A.M. Mikhailov and B.K. Vainshtein, "Electron microscope determination of the three-dimensional structure of the extended tail of the T6 bacteriophage," Soviet Physics-Crystallography, vol. 16, pp. 428-436, (1971).
40. E.R. Miller, E.M. McCurry, and B. Hruska, "An infinite number of laminagrams from a finite number of radiographs," Radiology, vol. 98, pp. 249-255, (1971).

41. A. Oppenheim, "Realization of digital filters using block-floating point arithmetic," I.E.E.E. Transactions on Audio and Electroacoustics, vol. 18, pp. 1301-1307, (1970).
42. A. Papoulis, Systems and Transforms with Applications in Optics, McGraw-Hill, New York, 1968.
43. D.P. Peterson and D. Middleton, "Sampling and reconstruction of wave number limited functions in N-dimensional euclidean spaces," Information and Control, vol. 5, pp. 279-323, (1962).
44. L.R. Rabiner, R.W. Schafer, and C.M. Rader, "The chirp z-transform algorithm and its application," Bell System Technical Journal, pp. 1249-1292, May 1969.
45. G.N. Ramachandran, "Reconstruction of substance from shadow," Proc. Indian. Acad. Sci., pp. 14-24, July 1971.
46. G.N. Ramachandran and A.V. Lakshminaraynan, "Three-dimensional reconstruction from radiographs and electron micrographs: application of convolutions instead of Fourier transforms," Proc. Nat. Acad. Sci., vol. 68, #9, pp. 2236-2249.
47. G.N. Ramachandran and A.V. Lakshminaraynan, "Three-dimensional reconstruction from radiographs and electron michrgraphs: III--description and application of the convolution method," Indian J. of Pure and Applied Physics, vol. 9, pp. 997-1003, (1971).
48. O. Tretiak, D. Ozonoff, J. Klopping, and M. Eden, "Calculation of internal structure from multiple radiograms," Proceedings of the Two-Dimensional Digital Signal Processing Conference--Univ. of Missouri--Columbia, pp. 6-2-1 -- 6-2-3, (1971).
49. O. Tretiak, M. Eden, and W. Simon, "Internal structure from x-ray images," 8th ICMBE, (1969).
50. B.K. Vainshtein, "Synthesis of projecting functions," Soviet Physics-Doillady, vol. 16, #2, pp. 66-69.
51. B.K. Vainshtein, "Finding the structure of objects from projections," Soviet Physics-Crystallography, vol. 15, #5, pp. 781-787.

BIOGRAPHICAL NOTE

Russell M. Mersereau was born in Cambridge, Massachusetts on August 29, 1946. He received the S.B., S.M., and E.E. degrees in 1969, 1969, and 1970 respectively from the Massachusetts Institute of Technology. From 1966 to 1968 he was a cooperative student with the AVCO-Everett Research Laboratories, Everett, Massachusetts. From September 1968 to September 1969 he was supported by a National Science Foundation Fellowship. From September 1969 to June 1971 he was a Teaching Assistant and from June 1971 to February 1973 he was an Instructor in the Electrical Engineering Department at MIT. He has also been associated with the Research Laboratory of Electronics at MIT since September 1969.

Mr. Mersereau is a member of Eta Kappa Nu, Tau Beta Pi, Sigma Xi and the Institute of Electrical and Electronics Engineers.